

Search for neutral MSSM Higgs bosons in association with b quarks in the $\tau\tau$ decay channels at CDF Run II

By

Charles A. Cox

B.S. (University of California, Berkeley) 2005

DISSERTATION

Submitted in partial satisfaction of the requirements for the degree of
DOCTOR OF PHILOSOPHY

in

Physics

in the

OFFICE OF GRADUATE STUDIES

of the

UNIVERSITY OF CALIFORNIA

DAVIS

Approved:

John Conway, Chair

Robin Erbacher

John Gunion

Committee in Charge

2013

Abstract

This thesis presents the results of a search for neutral MSSM Higgs bosons decaying to $\tau\tau$ with 5.9 fb^{-1} of data. The analysis requires at least one of the taus to decay leptonically, and explores three detection modes in two channels: $\tau_e\tau_\mu$, $\tau_e\tau_{had}$, and $\tau_\mu\tau_{had}$, where the index denotes the type of tau decay. In all modes we explore the tagged and untagged channel. No signal is observed limits were set on $\sigma(pp \rightarrow \phi + X) \times BR(\phi \rightarrow \tau\tau)$ as a function of Higgs mass. The results are also interpreted as exclusions of parameter space in the $\tan\beta$ vs m_A plane for several benchmark scenarios.

Acknowledgements

I would like to thank the large number of people that have helped me reach this point. Many people played a role in shaping this research and the help of others has been critical to the success of this work.

John Conway, my thesis advisor has been an excellent mentor and a persistent help throughout the process. Discussions with Anton Anastassov have been fruitful and productive in helping to structure and develop the analysis. My initial work at CDF was on the XFT project, and my thanks go to many of the others who helped with introducing me to the CDF environment Robin Erbacher, William Johnson, Alison Lister, Andrew Ivanov, Tom Schwarz and Aron Soha.

This work builds closely on work done by Cirstobal Cuenca Almenar in collaboration with John Conway and Anton Anastassov and his help was invaluable in getting started as well as on developing the aspects of the trigger and background studies. The continuation and extension of the trigger studies was done in collaboration with Robert Forrest who was a great help.

Finally I would like to thank my family, my brothers Rick and Scup and my mother, who have my deepest gratitude for their support.

Contents

1	Introduction	1
2	Theoretical Overview	3
2.1	The Standard Model	3
2.1.1	Interactions	4
2.1.2	Quantum Electrodynamics	5
2.1.3	Electroweak Theory	6
2.1.4	Quantum Chromodynamics	9
2.1.5	The Higgs Mechanism	10
2.1.6	Problems with the Standard Model	11
2.2	The Minimal Supersymmetric Standard Model	12
3	Experimental Overview	14
3.1	Tevatron and Accelerator Complex	14
3.1.1	Proton Source	14
3.1.2	Main Injector	15
3.1.3	Antiproton Source	15
3.1.4	Tevatron	16
3.2	The Collider Detector at Fermilab	16
3.2.1	Coordinates and Units	17
3.2.2	Tracking Systems	17
3.2.2.1	The Silicon Detectors	18
3.2.2.2	Central Outer Tracker: COT	18
3.2.3	Time-of-Flight: TOF	19
3.2.4	Calorimetry	19
3.2.4.1	Central Calorimeter: CEM & CHA	20
3.2.4.2	Plug Electromagnetic Calorimeter: PEM	20
3.2.4.3	Plug and Endwall Hadronic Calorimeter: PHA & WHA	21
3.2.5	Shower Maximum Detector	21
3.2.6	Muon Detection Systems	21
3.2.7	Cherenkov Luminosity Counter: CLC	21
3.3	Triggering	22
3.3.1	Level 1 Trigger	24
3.3.2	Level 2 Trigger	25
3.3.3	Level 3 Trigger	27

4	Event Selection	28
4.1	Datasets Used	28
4.2	Monte Carlo Simulations	28
4.3	Data-Monte Carlo Hybrid	29
5	Trigger Efficiencies	31
5.1	Introduction	31
5.1.1	Trigger paths description	31
5.1.1.1	Level 2 Trigger Requirements	32
5.1.1.2	Level 3 trigger requirements	32
5.1.2	Data Samples and Event Selection	32
5.1.3	Level 2 Trigger Efficiency	33
5.1.4	Level 3 Trigger Efficiency	38
5.1.5	Electron Trigger Issue	44
6	Particle Identification	45
6.1	Introduction	45
6.1.1	Electrons	46
6.1.2	Muons	49
6.1.3	Taus	51
6.1.4	Missing Transverse Energy (\cancel{E}_T)	57
7	Event Selection and Background Estimates	60
7.1	Event Cuts	60
7.1.1	General Requirements	60
7.1.2	ζ cut	60
7.1.3	Suppression of QCD backgrounds.	62
7.1.4	$Z \rightarrow ll$ Removal	62
7.2	Backgrounds and estimation methods	63
7.2.1	$Z \rightarrow ll$	63
7.2.2	Di-boson, $W + \gamma$, and $t\bar{t}$	63
7.2.3	Backgrounds with Misidentified or Non-isolated e or μ in the $\tau_e\tau_\mu$ Detection Mode	63
7.2.4	Backgrounds from Misidentified $jet \rightarrow \tau_{had}$ in the $\tau_l\tau_{had}$ Detection Modes	64
7.2.5	Methods for Modeling the $Z \rightarrow \tau\tau$ Background in the b Tagged Channel	66
7.3	Signal Selection Efficiency	68

8 Results	70
8.1 Observed Results	70
8.2 Systematic Uncertainties	80
8.2.1 Rate: ID efficiencies	80
8.2.2 Rate: Trigger Efficiencies	81
8.2.3 Rate: Sidebands	81
8.2.4 Rate: QCD fakes	81
8.2.5 Rate: Tag efficiencies	81
8.2.6 Rate: Cross sections and branching fractions	81
8.2.7 Rate: Signal PDFs	82
8.2.8 Rate: Luminosity	82
8.2.9 Shape: Jet energy scale	82
8.2.10 Shape: EM energy scale	82
8.2.11 Shape: Mistag rate	82
8.3 Fitting Method	82
8.4 Nuisance Parameters for Systematic Uncertainties	84
8.5 Expected Sensitivity	86
8.6 Results	86
8.7 Interpretation of the Limits	94
8.7.1 Production Cross-section Calculations	94
8.7.2 Excluded region in $\tan\beta$ vs m_A	95
8.8 Conclusions	96
List of Figures	97
List of Tables	100
Bibliography	101

Chapter 1

Introduction

The standard model (SM) of Particle Physics has been an astounding success story. It accurately describes the most fundamental interactions and particles and has successfully passed a rigorous array of tests of unprecedented precision. At a base level it is a quantum field theory of the gauge group $G = SU(3)_C \times SU(2)_L \times U(1)_\gamma$. With each gauge group corresponding to the symmetry group of a different interaction, the strong interaction obeys the color symmetry modeled by the $SU(3)_C$ group, the weak interaction by the $SU(2)_L$ group and the electromagnetic interaction by the $U(1)_\gamma$ group.

Despite its great success it is widely believed that the standard model is not a complete theory and that extensions must be made to it to address its flaws. From a theoretical standpoint its issues include the requirement of artificial renormalization at high energy, the large number of free parameters, and the hierarchy problem, the problem of maintaining the mass scale between M_W and M_{GUT} or M_{pl} in the face of large quantum loop corrections and the related parameter fine-tuning that is required. From an experimental standpoint there are challenges in accounting for gravitation as well as the existence of Dark Matter or Dark Energy.

Supersymmetry (SUSY) is a proposed theoretical symmetry that connects fermions and bosons. It supposes an independent symmetry between particles whose spins differ by 1/2, but with otherwise identical quantum numbers. It therefore connects a pair of “superpartner” particles, with different spins but the same electric charge, weak isospin. Due to the natural negative sign associated with fermion loop diagrams and the otherwise identical quantum numbers, supersymmetry provides a natural solution to the hierarchy problem by the quadratic term loop cancellations of the superpartners.

One particular SUSY theory is the minimal supersymmetric standard model (MSSM). It is so called because it includes only superpartners for the SM fermions and gauge bosons and the minimal number of Higgs chiral multiplets and is a popular subject for supersymmetric searches. This research is one such study, namely a search for a neutral MSSM Higgs boson in the $\tau\tau$ decay channel at the Collider Detector at Fermilab (CDF) located at the Tevatron.

The Tevatron is a hadron collider, providing $p - \bar{p}$ collisions with a center of mass energy of $\sqrt{s} = 1.96$ TeV. There are two detectors analyzing these collisions, CDF and D0. Both experiments have produced very significant scientific results, such as discovery of the top quark, or measurement of the B_s^0 mixing. In addition recently the Tevatron experiments were able to rule out a range of SM Higgs boson masses.

CDF also mounts an active search for beyond the standard model signatures. In general these are signature based and are based on accurate modeling of standard model contributions and then assessing any deviation from the standard model of the chosen signature.

The analysis presented in this dissertation focuses on the search for neutral Higgs bosons of the minimal supersymmetric model (MSSM) decaying to tau pairs. The production of these particles could be highly enhanced at the Tevatron depending on MSSM parameter space. Due to the short lifetime of tau leptons and their relatively rich decay spectrum we have several channels available to us. Within these di-tau decays we select three separate modes, one mode whereby one tau decays to an electron and one decays to a muon, one mode where one tau decays hadronically and the other to an electron and one mode where one tau decays hadronically and the other to a muon. We then further separate each of these modes into a tagged and untagged channel to better exploit the enhanced coupling of MSSM Higgs bosons to b-quarks.

This thesis begins by sketching the theoretical background of the standard model and supersymmetry in Chapter 2. Chapter 3 gives a brief outline of the experimental machinery at the Tevatron and CDF. Chapters 4 through 7 discuss the different components of the analysis itself and Chapter 8 discusses the results.

Chapter 2

Theoretical Overview

This chapter is a brief outline of the most important theoretical underpinnings of this search, namely the standard model (SM) and the minimal supersymmetric standard model (MSSM) with particular attention to the Higgs sector the MSSM and its phenomenological consequences.

Although the SM has shown an unparalleled level of accuracy and completeness it is widely held not to be a complete theory. It has several widely recognized problems and most scientists expect that it is a low energy effective theory which would be superseded at some higher energy. Several theoretical extensions exist aiming to address these issues, the MSSM is one of them.

2.1 The Standard Model

The standard model is a quantum field theory which has proven to be consistent with experimental results with unprecedented accuracy. (2, 3) A complete description of the theory is easily available in the scientific literature, but in this section we shall do a simple overview of salient points. (5)

In the standard model the fundamental building blocks of Nature are divided in several ways. Firstly, there is the separation between fermions, which have spin $\frac{1}{2}$ and form the building blocks of all matter and gauge bosons, with spin 1 which act as force carriers.

The fermions can be further separated into the quarks (u,d,c,s,t,b) and the leptons (electrons e , muons μ and taus τ , and their corresponding neutrinos, ν_e, ν_μ, ν_τ). The quarks possess an unbroken color symmetry corresponding to the strong interactions with three degrees of freedom and a broken “flavor” symmetry dividing the six different quarks. The leptons are colorless (i.e. do not interact via the strong force) but interact via the electromagnetic (for the e , μ , and τ only) and the weak interactions. All of the fermions also have corresponding anti-particles.

All of the fermions can be grouped together into three generations, with each generation identical to the others in all quantum numbers except for mass. Most of the immediate world is composed of particles from the first generation consisting of the up (u) and down (d) quarks, the electron (e) and its corresponding neutrino (ν_e). The other generations are more massive and have correspondingly lower lifetimes and do not generally appear in ordinary matter.

The bosons act as the intermediaries in the standard model, with different bosons corresponding two different symmetries and/or interactions. The electromagnetic interaction is mediated by the photon (γ), the weak interaction by the W^\pm and Z^0 , and the strong interaction by the gluons (g). Finally there is the as yet unconfirmed Higgs boson H with spin 0 which is introduced for the Higgs mechanism of spontaneous symmetry breaking to be accomplished in which the masses of all the bosons and fermions are obtained.

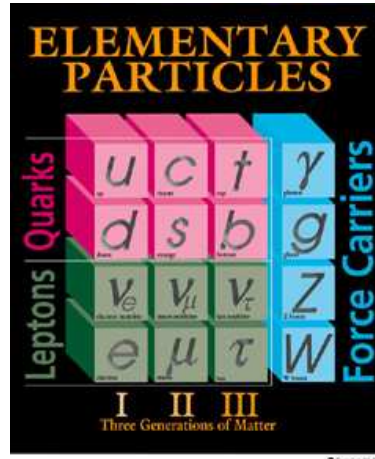


Figure 2.1: The standard model particles

2.1.1 Interactions

It is well established that there are four characteristic interactions among fundamental particles, three of which are well described in the SM, the electromagnetic interaction mediated by the massless photon in the standard model, the weak interaction mediated by the massive W^\pm and Z^0 bosons and the strong interaction mediated by massless gluons. The fourth interaction is the gravitational interaction, theoretically modeled by the graviton, but due to the weak coupling strength it does not play a role in the particle interactions generally examined in High Energy physics.

The electromagnetic interaction is probably the best known of the SM interactions and has a long history of investigation. It is described by quantum electrodynamics (QED), a gauge theory with an Abelian $U(1)$ symmetry. QED is formulated as a quantum field theory and is renormalizable and generally well behaved, with higher order loop integrals manageable via perturbation theory because of the small coupling constant $\alpha = \frac{e^2}{4\pi} \simeq \frac{1}{127}$.

The theory of the weak interaction was originally developed by Fermi to describe the current-current interaction with $V - A$ currents. The initial theory was later developed in the framework of non-Abelian gauge theory with $SU(2)_L \times U(1)_Y$ which is now called the electroweak standard model, including the weak and electromagnetic interactions.

The strong interaction describes color interactions between quarks. It has the largest coupling constant of the known interactions and is responsible for keeping the quarks inside hadrons and mesons together. The corresponding field theory in the standard model is the non-Abelian gauge theory with $SU(3)_c$ color symmetry and is called quantum chromodynamics (QCD).

The guiding symmetry of the standard model then is described by the simple direct product of the symmetry for the strong interactions $SU(3)_c$ and that describing the electroweak $SU(2)_L \times U(1)_Y$, or $G = SU(3)_c \times SU(2)_L \times U(1)_Y$. The quantum field theory that obeys that symmetry is the standard model of particle physics and is characterized by three important

principles, that it is a gauge theory, that it is renormalizable and that the symmetry breaking occurs spontaneously.

2.1.2 Quantum Electrodynamics

For QED we seek to construct a gauge invariant quantum field theory. We begin with the Lagrangian \mathcal{L} describing the field of a single free fermion with mass m . It is expressed as

$$\mathcal{L} = \bar{\psi}(i\gamma^\mu \partial_\mu - m)\psi \quad (2.1)$$

where ψ is a 4-component spinor field of the fermion and $\partial_\mu = \partial/\partial x^\mu$ ($\mu = 0,1,2,3$). γ^μ are the 4 x 4 Dirac matrices and the summation over μ is implied via the standard conventions while the m is understood to be multiplied by a 4 x 4 unit matrix I . The gauge transformation of this system is described by

$$\psi \rightarrow \psi' = e^{i\phi}\psi = U_\phi\psi \quad (2.2)$$

Since we define ϕ as constant everywhere in space-time, it follows immediately that the transformation is unitary, that is $U_\phi^\dagger U_\phi = 1$ and that it is Abelian, that is $U_{\phi_1} U_{\phi_2} = U_{\phi_2} U_{\phi_1}$. So the transformation 2.2 is global, unitary and Abelian, it is denoted by U(1).

Now if we seek to make the global symmetry a local symmetry, i.e. we introduce a x -dependent phase parameter $\phi(x)$ then the kinetic term becomes no longer invariant, that is

$$\mathcal{L} \rightarrow \mathcal{L}' = \mathcal{L} - j^\mu(x)\partial_\mu\psi(x) \quad (2.3)$$

where $j^\mu(x) = \bar{\psi}\gamma^\mu\psi$ is the vector Noether current. In order to restore the invariance we must replace ∂_μ with the covariant derivate D_μ

$$D_\mu \equiv \partial_\mu - ieA_\mu \quad (2.4)$$

Where A_μ is a vector field (spin 1) that transforms like

$$A_\mu \rightarrow A'_\mu \equiv A_\mu + \frac{1}{e}\partial_\mu\phi(x) \quad (2.5)$$

The Lagrangian therefore becomes

$$\mathcal{L} = \bar{\psi}(i\gamma^\mu \partial_\mu - m)\psi + e\bar{\psi}\gamma^\mu\psi A_\mu \quad (2.6)$$

which is invariant under the local transformation. We do need to add a kinematic term for the new field, which we add as

$$\mathcal{L} = -\frac{1}{4}F_{\mu\nu}F^{\mu\nu} \quad (2.7)$$

where F is the electromagnetic field tensor, defined as:

$$F_{\mu\nu} \equiv \partial_\mu A_\nu - \partial_\nu A_\mu \quad (2.8)$$

lepton family	Q	(T, T^3)	Y
ν_e, ν_μ, ν_τ	0	$(\frac{1}{2}, +\frac{1}{2})$	-1
e_L, μ_L, τ_L	-1	$(\frac{1}{2}, -\frac{1}{2})$	-1
e_R, μ_R, τ_R	-1	0	-2

Table 2.1: Quantum number assignment of lepton families in the GWS model

So the resultant total Lagrangian is

$$\mathcal{L}_{QED} = \bar{\psi}(i\gamma^\mu D_\mu - m)\psi - \frac{1}{4}F_{\mu\nu}F^{\mu\nu} \quad (2.9)$$

The field theory with \mathcal{L}_{QED} is called quantum electrodynamics (QED), the Lagrangian obeys the global unitary and Abelian symmetry $U(1)$ and the interactions described in 2.9 encompass the entirety of QED.

2.1.3 Electroweak Theory

The standard model electroweak theory is a non-Abelian gauge theory with $SU(2)_L \times U(1)_Y$ gauge symmetry. It represents as a unified whole the electromagnetic and weak interactions. In order to match with observed phenomena, in particular the observed fact that in weak processes we only see couplings between left-handed leptons and right-handed anti-leptons, lead to constructing a model whereby one family of leptons is represented as a left-handed doublet L and a right-handed singlet R or the $SU(2)$ group

$$L = \left(\begin{pmatrix} \nu_e \\ e \end{pmatrix} \right)_L, R = e_R \quad (2.10)$$

and more completely we represent the quantum numbers as seen in 2.1

Where the weak-hypercharge (Y) is related to the electromagnetic charge Q and the $SU(2)$ generators T

$$Q = T^3 + \frac{Y}{2} \quad (2.11)$$

Then the Lagrangian is to be constructed with L and R and should be invariant under the $SU(2)_L$ and $U(1)_Y$ groups or

$$SU(2)_L : L \rightarrow L' = e^{-i\alpha^i(x)\tau^i/2}L, R \rightarrow R' = R, \quad (2.12)$$

$$U(1)_Y : L \rightarrow L' = e^{i/2\beta(x)}L, R \rightarrow R' = e^{i\beta(x)}R \quad (2.13)$$

This is constructed as

$$\mathcal{L}_F = \bar{L}i\gamma^\mu(\partial_\mu - ig\frac{\vec{\tau}}{2} \cdot \vec{A}_\mu + \frac{i}{2}g'B_\mu)L + \bar{R}i\gamma^\mu(\partial_\mu + ig'B_\mu)R \quad (2.14)$$

where A_μ^i ($i = 1,2,3$) and B_μ are gauge boson fields associated with $SU(2)_L$ and $U(1)_Y$, respectively. g and g' are the gauge coupling constants corresponding to $SU(2)_L$ and $U(1)_Y$, respectively. The covariant derivatives are given by

$$D_\mu = \partial_\mu - ig \frac{\vec{\tau}}{2} \cdot \vec{A}_\mu - ig' \frac{Y}{2} B_\mu \quad (2.15)$$

The kinetic term of the gauge fields is given by

$$\mathcal{L}_G = -\frac{1}{4} F_{\mu\nu}^i F^{i\mu\nu} - \frac{1}{4} B_{\mu\nu} B^{\mu\nu} \quad (2.16)$$

$$F_{\mu\nu}^i = \partial_\mu A_\nu^i - \partial_\nu A_\mu^i + g \epsilon_{ijk} A_\mu^j A_\nu^k \quad (2.17)$$

$$B_{\mu\nu} = \partial_\mu B_\nu - \partial_\nu B_\mu \quad (2.18)$$

where $F_{\mu\nu}^i$ ($i=1,2,3$) is the field strength tensor the gauge field corresponding to $SU(2)_L$ and $B_{\mu\nu}$ is the field strength tensors of the gauge field corresponding to $U(1)_Y$. In both 2.14 and 2.18 the mass terms do not appear as they would violate invariance requirements. In order to add mass to the fermions and gauge bosons we need spontaneous symmetry breaking, i.e. the Higgs mechanism. Since we want a massless photon after symmetry breaking we need to have

$$SU(2)_L \times U(1)_Y \rightarrow U(1)_{em} \quad (2.19)$$

The simplest model to accomplish this is by adding a $SU(2)$ doublet of 2 complex scalar fields, ϕ with weak hypercharge $Y_\phi = +1$. The Lagrangian for the scalars is

$$\mathcal{L}_s = (D_\mu \phi)^\dagger (D^\mu \phi) - V(\phi^\dagger \phi) \quad (2.20)$$

with the potential term $V(\phi^\dagger \phi)$ given by

$$V(\phi^\dagger \phi) = m^2 \phi^\dagger \phi + \lambda (\phi^\dagger \phi)^2 \quad (2.21)$$

where m^2 and λ are real constant parameters. Finally we add the coupling term between fermions and scalars which are to provide the fermion mass, called the Yukawa interaction terms

$$\mathcal{L}_Y = -G_e (\bar{L} \phi R + \bar{R} \phi^\dagger L) + h.c. \quad (2.22)$$

and the full $SU(2)_L \times U(1)_Y$ gauge invariant Lagrangian of the GWS model is then just

$$\mathcal{L} = \mathcal{L}_F + \mathcal{L}_G + \mathcal{L}_s + \mathcal{L}_Y \quad (2.23)$$

So far we have only discussed the case for one family. To extend the model with additional generations we must extend the different components. The fermion sector is simply extended, namely

$$\mathcal{L}_F = \mathcal{L}_F^{(e)} + \mathcal{L}_F^{(\mu)} + \mathcal{L}_F^{(\tau)} \quad (2.24)$$

Where both terms are the same as 2.14 with the appropriate substitution of fermion field terms L and R by $L_{e/\mu/\tau}$ and $R_{e/\mu/\tau}$ as appropriate. However, for the Yukawa term we have additional interaction terms

$$\mathcal{L}_Y = -G_{ij}\bar{L}_i\phi R_j + h.c. \quad (2.25)$$

where $i,j = e, \mu, \tau$ and after symmetry breaking we obtain the fermion mass terms

$$\mathcal{L}_F^{(mass)} = -\vec{l}M\vec{r} + h.c. \quad (2.26)$$

where

$$\vec{l} = \begin{pmatrix} \bar{e}_L & \bar{\mu}_L & \bar{\tau}_L \end{pmatrix} \quad (2.27)$$

$$\vec{r} = \begin{pmatrix} e_R \\ \mu_R \\ \tau_R \end{pmatrix} \quad (2.28)$$

and where M is the mass matrix, a 3 x 3 complex not necessarily hermitian matrix. In general it can be diagonalized by a transformation

$$U^\dagger MV = M_d \quad (2.29)$$

where M_d is a diagonal matrix and U and V are unitary matrices. Via redefining non-observable phases of the lepton fields one can further make the elements of M_d real and positive. Then we can rewrite $\mathcal{L}_F^{(mass)}$ as

$$\mathcal{L}_F^{(mass)} = -\vec{l}'M\vec{r}' + h.c. \quad (2.30)$$

where

$$\begin{pmatrix} e'_L \\ \mu'_L \\ \tau'_L \end{pmatrix} = U^\dagger \begin{pmatrix} e_L \\ \mu_L \\ \tau_L \end{pmatrix} \quad (2.31)$$

$$\begin{pmatrix} e'_R \\ \mu'_R \\ \tau'_R \end{pmatrix} = V^\dagger \begin{pmatrix} e_R \\ \mu_R \\ \tau_R \end{pmatrix} \quad (2.32)$$

Then the prime states are the mass eigenstates and are not equal to current/weak eigenstates in general. The observed states are the mass eigenstates, so when the interactions in the generation space (mass) we allow for intergenerational mixing. It is this mixing that leads to neutrino oscillations when massive neutrinos are included in the model.

Extending this to quarks is relatively straightforward. We add three SU(2) doublets (corresponding to the left handed quarks of each of the three generations), with one up-type and one down-type quark in each doublet and 6 singlets, corresponding to the right-handed quarks of each generation. To allow for compactness we introduce the following notation

$$Q_{Li} = \begin{pmatrix} U_i \\ D_i \end{pmatrix}, U_{Ri}, D_{Ri} \quad (i = 1, 2, 3) \quad (2.33)$$

quark family	Q	(T, T^3)	Y
u_L, c_L, t_L	$+\frac{2}{3}$	$(\frac{1}{2}, +\frac{1}{2})$	$+\frac{1}{3}$
d_L, s_L, b_L	$-\frac{1}{3}$	$(\frac{1}{2}, -\frac{1}{2})$	$+\frac{1}{3}$
u_R, c_R, t_R	$+\frac{2}{3}$	0	$+\frac{4}{3}$
d_R, s_R, b_R	$-\frac{1}{3}$	0	$-\frac{2}{3}$

Table 2.2: Quantum number assignment of quark families

where i stands for the generation: $U_1 = u$, $D_1 = d$, etc. Then the Lagrangian can be written in terms of the quarks and their covariant derivatives as

$$\mathcal{L}_F = \sum_{i=1}^3 \bar{Q}_{Li} i\gamma^\mu (\partial_\mu - ig\frac{\vec{\tau}}{2} \cdot \vec{A}_\mu - \frac{i}{6} g' B_\mu) Q_{Li} \quad (2.34)$$

$$+ \sum_{i=1}^3 \bar{U}_{Ri} i\gamma^\mu (\partial_\mu - i\frac{2}{3} g' B_\mu) U_{Ri} \quad (2.35)$$

$$+ \sum_{i=1}^3 \bar{D}_{Ri} i\gamma^\mu (\partial_\mu + i\frac{1}{3} g' B_\mu) D_{Ri} \quad (2.36)$$

The gauge field terms \mathcal{L}_G and scalar field terms \mathcal{L}_s are the same as the leptons. The Yukawa terms can be written as

$$\mathcal{L}_Y = - \sum_{i,j} (\Gamma_{i,j}^{(D)} \bar{Q}_{Li} \phi D_{Rj} + \Gamma_{i,j}^{(U)} \bar{Q}_{Li} \tilde{\phi} U_{Rj} + h.c.) \quad (2.37)$$

where the $\Gamma_{i,j}^{(D/U)}$ are Yukawa couplings which in general are unconstrained complex parameters and $\tilde{\phi}$ is defined from ϕ as $\tilde{\phi} = i\tau_2 \phi^*$ where ϕ^* is the complex conjugate of ϕ . A similar treatment of the mass matrices and flavor changing behavior in the quark sector is possible and relatively straightforward.

2.1.4 Quantum Chromodynamics

In the standard model the theory of the strong interactions is quantum chromodynamics (QCD), a non-Abelian gauge theory with SU(3) color symmetry. The QCD Lagrangian for the interaction between quarks q and gluons A_μ^i for ($i=1,2,\dots,8$) is given by

$$\mathcal{L} = \bar{q}(i\not{D} - m)q - \frac{1}{4} F_{\mu\nu}^i F^{i\mu\nu} \quad (2.38)$$

and the quark field q and covariant derivative are given by

$$q = \begin{pmatrix} q^R \\ q^G \\ q^B \end{pmatrix} \quad (2.39)$$

$$D_\mu = \partial_\mu - ig_s \frac{\lambda^i}{2} A_\mu^i \quad (2.40)$$

Where the superscripts R,G,B stand for red, green and blue respectively, g_s is the strong coupling constant and λ^i are the 3 x 3 Gell-Mann matrices. $F_{\mu\nu}^i$ are the field strength tensor for gluon fields A_μ^i and are given by

$$F_{\mu\nu}^i = \partial_\mu A_\nu^i - \partial_\nu A_\mu^i + g_s f_{ijk} A_\mu^j A_\nu^k \quad (2.41)$$

where f_{ijk} are the structure constants of the color $SU(3)_c$ group. There are several important consequences of the chosen structure of QCD. Firstly the extra term, which corresponds to the non-Abelian nature of QCD, compared to QED leads to gluon self-interactions. These in turn can be shown to lead to anti-screening in the coupling constants, or "asymptotic freedom," $\alpha_s(Q^2)$ decreases with increasing Q^2 , while for small Q^2 $\alpha_s(Q^2)$ becomes large.

This essentially divides QCD into two regions, for large values of Q^2 quarks and gluons behave as free particles ("asymptotic freedom") and perturbative calculations are valid. This corresponds to behavior such as deep inelastic scattering. For small Q^2 the quark-gluon coupling becomes large, perturbative calculations are invalid and the quarks and gluons are confined in hadrons ("confinement"). This is responsible for the observed lack of free quarks/gluons in nature. QCD then is the color $SU(3)$ non-Abelian gauge theory of strong interactions

2.1.5 The Higgs Mechanism

As mentioned previously mass terms can not be directly added into the electroweak theory without violating gauge invariance. The way in which the standard model avoids this problem is via adding masses via spontaneous symmetry breaking through the Higgs mechanism.

We consider adding a complex doublet field $\phi = \begin{pmatrix} \phi_1 \\ \phi_2 \end{pmatrix}$ to the $SU(2)$ gauge invariant Lagrangian. We then have

$$\mathcal{L} = (D_\mu \phi)^\dagger (D^\mu \phi) - \frac{1}{4} F_{\mu\nu}^i F^{i\mu\nu} - V(\phi^\dagger \phi) \quad (2.42)$$

with

$$D_\mu \phi = (\partial_\mu - ig \frac{\tau^i}{2} A_\mu^i) \phi, \quad (i = 1, 2, 3) \quad (2.43)$$

$$F_{\mu\nu}^i = \partial_\mu A_\nu^i - \partial_\nu A_\mu^i + g \epsilon_{ijk} A_\mu^j A_\nu^k, \quad (2.44)$$

$$V(\phi^\dagger \phi) = -\mu^2 \phi^\dagger \phi + \lambda (\phi^\dagger \phi)^2, \quad (\mu^2 > 0) \quad (2.45)$$

We then parametrize the field $\phi(x)$ in terms of the new real field $H(x)$ and $\xi^i(x)$ ($i = 1, 2, 3$) as

$$\phi(x) = \frac{1}{\sqrt{2}} e^{i\tau^i \xi^i(x)/2\nu} \begin{pmatrix} 0 \\ \nu + H(x) \end{pmatrix} \quad (2.46)$$

We then transform the fields according to a particular gauge transformation, the unitary gauge, as follows

$$\phi(x) \rightarrow \phi'(x) = U(x) \phi(x) = \frac{1}{\sqrt{2}} \begin{pmatrix} 0 \\ \nu + H(x) \end{pmatrix} \quad (2.47)$$

$$\vec{A}_\mu \rightarrow \vec{B}_\mu = U(x) \vec{A}_\mu U^{-1} - \frac{i}{g} (\partial_\mu U) U^{-1} \quad (2.48)$$

$$U(x) = e^{-i\tau^i \xi^i(x)/2\nu} \quad (2.49)$$

Then the Lagrangian becomes

$$\mathcal{L} = (D_\mu \phi)'^\dagger (D^\mu \phi)' - \frac{1}{4} F_{\mu\nu}^i(B) F^{i\mu\nu}(B) + \mu^2 (\phi'^\dagger \phi') - \lambda (\phi'^\dagger \phi')^2 \quad (2.50)$$

If we then extrapolate the Lagrangian in terms of the component fields of ϕ' we obtain the following

$$\mathcal{L} = \frac{1}{2} \partial_\mu H \partial^\mu H - \mu^2 H^2 - \frac{1}{4} F_{\mu\nu}^i(B) F^{i\mu\nu}(B) + \frac{g^2 \nu^2}{8} B_\mu^i B^{i\mu} \quad (2.51)$$

$$+ \frac{g^2}{8} B_\mu^i B^{i\mu} H (2\nu + H) - \lambda \nu H^3 - \frac{\lambda}{4} H^4 - \frac{\nu^4}{4} \quad (2.52)$$

Looking at this we see that the three Goldstone boson $\xi^i(x)$ fields have disappeared, replaced by a triplet of massive vector fields B_μ^i and a single massive scalar. In other words the Goldstone bosons were “eaten” by the gauge bosons to make their longitudinal components. This is the same basic mechanism by which the Higgs mechanism works under other symmetries. When applied to the $SU(2)_L \times U(1)_Y$ theory that is electroweak theory it leads to the fermions obtaining mass through the Yukawa couplings and the creation of the massive gauge bosons (W^\pm, Z) and a new Higgs boson (H).

2.1.6 Problems with the Standard Model

Despite its widespread and well established success the standard model does suffer from some problems and is widely expected not to be the most fundamental theory but simply a low energy approximation, accurate up to some scale. Some of these problems are the large number of free parameters, the non-unification of the gauge couplings and the “hierarchy problem.”

The “hierarchy problem” is the problem of maintaining the separation between the mass scales of the standard model $\sim M_W$ to the higher mass scales where a more fundamental theory is expected. This problem is particularly significant with regard to scalar particles such as the Higgs particle because the Higgs mass gets a large quantum correction proportional to this higher mass scale. While it is possible to arrange the parameters such that the Higgs mass remains at the lower mass scale, doing so requires excessive fine tuning of the parameters.

One attraction of supersymmetry (SUSY) is that it offers a natural solution to the problem. SUSY is a hypothetical symmetry between fermions and bosons, that when a Lagrangian is invariant under a transformation that connects particles whose spin differ by 1/2 that theory is said to be supersymmetric. It connects a pair of particles with different spins but otherwise identical quantum numbers, such as electric charge, weak isospin, color, etc. This is relevant to the hierarchy problem because the Feynman rules provide an additional negative sign for loop diagrams with fermions, so if the supersymmetry is exact then the loop for every particle would be exactly cancelled by its superpartner particle. In practice it is expected from the absence of observed superpartners that supersymmetry would be broken, but it still reduces the scale of the hierarchy problem to the order of M_{SUSY} rather than M_{GUT} or M_{pl} . This is one of several reasons SUSY is thought of as an attractive extension of the standard model.

2.2 The Minimal Supersymmetric Standard Model

There are many possible supersymmetric extensions of the standard model, the particular one that is explored in this research is the minimal supersymmetric standard model or MSSM. It is so called because it is the simplest extension of the SM to incorporate supersymmetry. A full review of the MSSM is beyond the scope of this thesis but there are a large number of such reviews in the scientific literature but included here is an overview of some of its general features with particular attention to the Higgs sector and the phenomenological consequences of relevance to this search. (6)

The most immediately relevant feature of the MSSM for this search is the Higgs sector. In contrast to the standard model, in the MSSM the Higgs sector consists of two Higgs doublets. This is necessary because of the need for an even number of fermion doublets to avoid the Witten anomaly for $SU(2)_L$ and because of the need for Higgs doublets of opposite hypercharge to cancel the $U(1)_Y^3$ and $U(1)_Y SU(2)_L^2$ gauge anomalies that stem from the higgsinos. In terms of mass eigenstates this produces two CP even neutral Higgs bosons (h^0, H^0) one CP odd neutral Higgs boson (A^0) and two charged Higgs bosons (H^\pm). This sector is largely defined by the parameters $\tan \beta = \frac{v_2}{v_1}$ (v_1, v_2 being the vacuum expectation values of the Higgs field couplings to the *up*- and *down*- type quarks respectively) and the mass of the CP odd neutral boson m_A . In this parametrization, m_h and m_H are functions $\tan \beta$ and m_A .

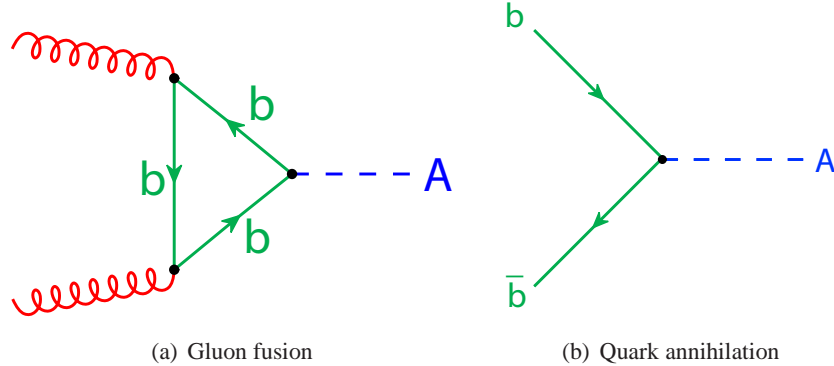
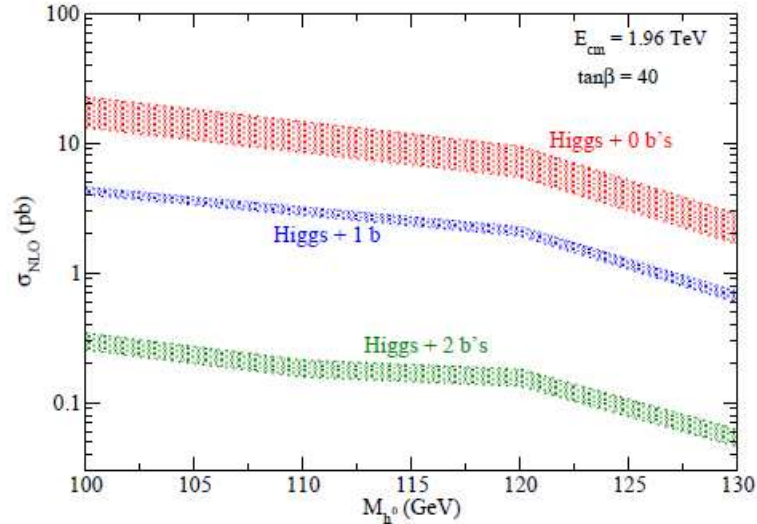


Figure 2.2: Lowest order diagram contributing to $gg \rightarrow \phi$ and $b\bar{b} \rightarrow A$.

The dominant production mechanisms for neutral MSSM Higgs bosons at hadronic colliders are gluon fusion ($gg \rightarrow \phi$) and quark annihilation ($q\bar{q} \rightarrow \phi$). The Feynman diagrams are shown in Figure 2.2. For $gg \rightarrow \phi$ the diagram is the same as the one in the SM, except for the replacement of top quarks with bottom quarks in the loop. The Higgs coupling to *down*-type quarks is proportional to $\tan \beta$ and the *b*-quark loop dominates the cross section despite the m_b/m_t suppression factor. The quark annihilation is dominated by $b\bar{b} \rightarrow \phi$. There are higher order diagrams leading to presence of one or two observable *b*-quarks in the final state. These are especially important for Higgs searches relying on detection of three or four *b*-jets and in this



(a) Higgs Production cross section

Figure 2.3: Rate of associated production with b-quarks of MSSM Higgs for a particular set of MSSM parameters.

analysis they are relevant to the tagged channels. We refer the reader to (9) for more information on MSSM Higgs production.

The decays of the neutral MSSM Higgs bosons are governed by the couplings to *up*- and *down*-type particles through the $\tan \beta$ and m_A parameters. The dominant decay modes are $\phi \rightarrow b\bar{b}$ and $\phi \rightarrow \tau^+\tau^-$ with branching fractions $\mathcal{B}(\phi \rightarrow b\bar{b}) \sim 90\%$ and $\mathcal{B}(\phi \rightarrow \tau^+\tau^-) \sim 8\%$ ¹. Consequently, these are the relevant decay modes for neutral MSSM Higgs searches. Despite the large advantage in branching fraction of the $b\bar{b}$ mode, the $\tau\tau$ channel is still *very much* relevant. Due to large di-jet backgrounds the gluon fusion mechanism can not be probed using the $b\bar{b}$ channel (given the current state of di-jet mass resolution). One is restricted to Higgs production in association with sufficiently high- p_T b quarks leading to considerable efficiency losses. On the other hand, the $\tau\tau$ mode allows the exploration of Higgs production through both gluon fusion and quark annihilation. The dominant background in this case is from $Z/\gamma^* \rightarrow \tau\tau$ events. This process is well modeled and has reliably measure cross-section from the $Z \rightarrow ee, \mu\mu$ channels, eliminating uncertainties in background normalization. That makes the $b\bar{b}$ and $\tau\tau$ channels equally useful tools for the searches.

Finally, the MSSM has an even larger number of free parameters than the standard model. Though much of the parameter space can be excluded for producing non-physical features of one kind or another it still leaves a substantial parameter space. That is why as part of this research the production cross section limits are interpreted as limits in the MSSM parameter space for some commonly used benchmark scenarios.

¹We do not consider "bosophilic" Higgs scenarios.

Chapter 3

Experimental Overview**3.1 Tevatron and Accelerator Complex**

The Tevatron (1) was a proton-antiproton collider at the Fermi National Accelerator Laboratory (FNAL or Fermilab) that for most of its lifetime was the highest-energy particle collider operational in the world. While in operation it produced $p\bar{p}$ collisions at a center of mass energy of 1.96 TeV. Data gathered in the “Run II” of the Tevatron is used in this study. The main components can be seen in Figure 3.1.

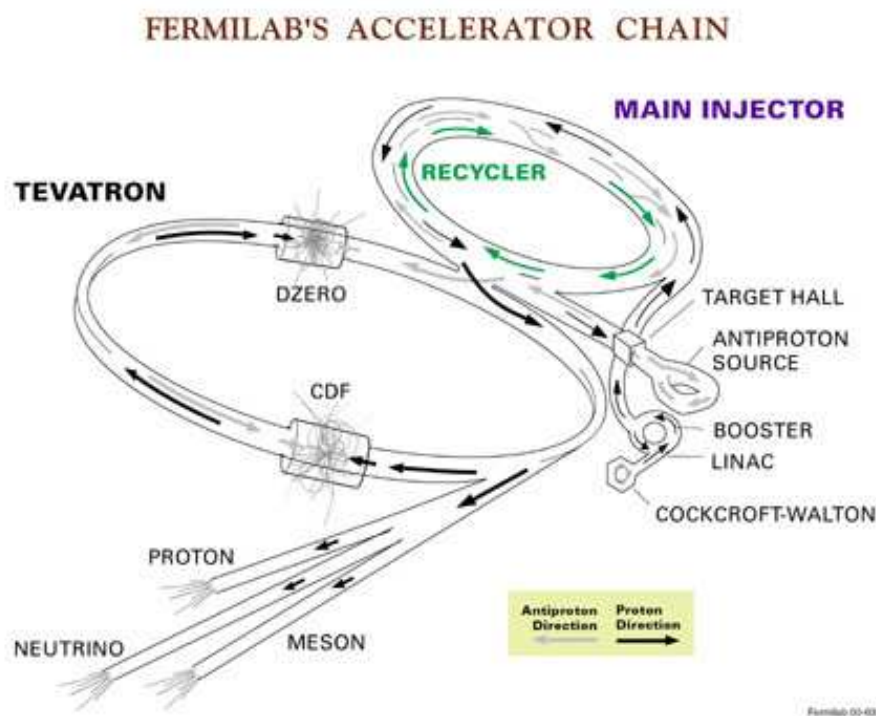


Figure 3.1: The Tevatron accelerator complex

3.1.1 Proton Source

The first step in the Tevatron accelerator chain is the the Fermilab Proton Source, which includes the Pre-accelerator, 400 MeV Linac and the 8 GeV Booster. The Pre-accelerator serves as a source of negatively charged hydrogen ions and accelerates them to an energy of 750 keV.

These ions are then passed into the Linac. The Linac is a series of radio frequency cavities (RFC) used as a linear accelerator and accelerates the hydrogen ions up to an energy of 400 MeV. The first section of the linac is the low energy drift tube Linac (DTL) and makes up the first five RFCs. Each DTL cavity uses a large power amplifier tube to amplify the 201 MHz RF

signal used in the cavities and accelerate the beam. The last 7 RFCs use Klystron amplifiers which amplify an 805 MHz RF signal that is fed into side coupled cavity Linac (SCL) modules. Every RF cycle in the DTL is used to accelerate beam but only one in four cycles in the SCL is used. The Linac and the Pre-accelerator can both accelerate beams at a 15 Hz repetition rate (once every 66 milliseconds).

The Linac's hydrogen ions then pass through a carbon foil and into the Booster. The carbon foil strips them of their electrons and the Booster RFC's accelerate the proton beam to 8 GeV with an operational rate of once every 66 milliseconds (15 Hz repetition rate). The Booster is the first circular accelerator and consists of a series of magnets arranged around a 75-meter radius circle, with 19 RFCs interspersed.

3.1.2 Main Injector

The next step is the Main Injector. The Main Injector is a circular synchrotron seven times larger than the booster divided up into 6 sections with 18 total accelerating cavities. Depending on the intended destination it accelerates the 8 GeV inputs to either 120 GeV or 150 GeV. When being used to send beam to the Antiproton Source the beam is accelerated to 120 GeV. When being used to inject protons or antiprotons into the Tevatron, called a "shot", the beam energy is 150 GeV. The Main Injector can accept as inputs either protons from the Booster or antiprotons from the Antiproton Source. Its operational rate is once every 2.2 seconds.

3.1.3 Antiproton Source

The Antiproton Source is responsible for \bar{p} production at the Tevatron. The Antiproton Source includes the target, Debuncher, and Accumulator. 120 GeV protons from the Main Injector are inserted and it then collides them with a nickel alloy target, collision producing a spray of secondary particles including antiprotons. Magnets are used to collect 8 GeV antiprotons from this spray which are then directed to the Debuncher synchrotron.

The Debuncher's primary purpose is to capture the antiprotons produced with a high momentum spread from the target. It also has beam-cooling systems that make the antiproton beam more manageable. The Debuncher does not accelerate the 8 GeV input antiprotons, only maintaining their energy and then passing them on to the Accumulator.

The Accumulator and the Recycler are used to further cool the beam while maintaining an energy of 8 GeV. The Accumulator is a synchrotron housed in the same tunnel as the Debuncher which cools the beam then passes it onto the Recycler. Though the Recycler was originally designed to 'recycle' the antiprotons from the Tevatron, this function was abandoned due to problems early in Run II of the Tevatron. Now it accepts transfers from the Accumulator and cools the beam further than the Accumulator can accomplish using a stochastic cooling system (like the Debuncher and Accumulator) and an electron cooling system. Like the Debuncher and Accumulator it does not accelerate the antiprotons but only maintains their energy at 8 GeV.

3.1.4 Tevatron

The Tevatron is the final and largest accelerator so far used to produce a $p\bar{p}$ colliding beam. It has a radius of 1 km and is a circular synchrotron with eight 53.1 MHz RFCs. It takes both protons and antiprotons from the Main Injector and accelerates them from 150 GeV to 980 GeV. Once accelerated the Tevatron then circulates these beams for an extended period of time while collisions occur, maintaining their energy until the instantaneous luminosity has fallen far enough and the antiproton source has accumulated enough \bar{p} s to warrant another shot. The time while it maintains the beam is called a “store”. The Tevatron is divided into six sectors labeled A through F. Each sector has five service buildings labeled 0 through 4. The CDF collision hall is located at the B0 section. The Tevatron typically delivers initial instantaneous luminosity of about $350 \text{ cm}^{-2} \text{ s}^{-1}$ and typically stores are dropped with an instantaneous luminosity near $50 \text{ cm}^{-2} \text{ s}^{-1}$. Though both initial and final luminosity vary between stores.

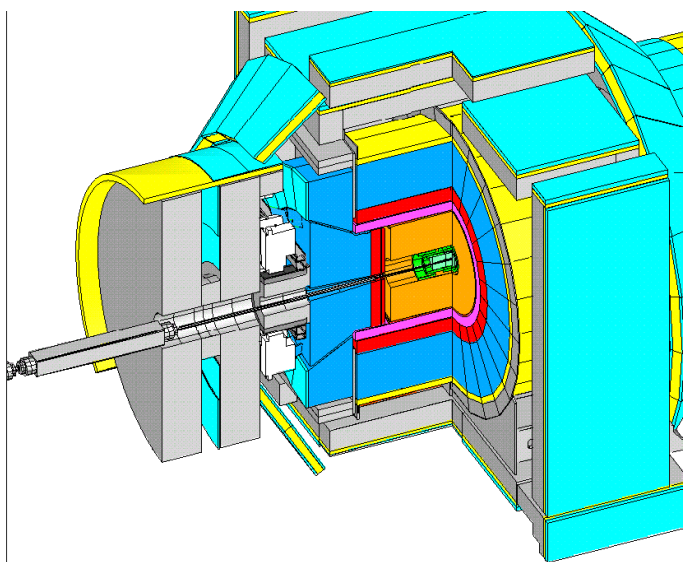


Figure 3.2: The CDF II detector

3.2 The Collider Detector at Fermilab

The Collider Detector at Fermilab Run II detector (CDF II or CDF) is an azimuthally and forward-backward symmetric apparatus weighing approximately 4,500 tons and including more than 1 million individual detector elements. It is a general purpose solenoidal detector which utilizes precision charged particle tracking with fast projective calorimetry and fine grained muon detection. A schematic of the detector is Figure 3.2. The tracking systems are contained within

a superconducting solenoid which generates a 1.4 T magnetic field parallel to the beam axis. The calorimetry and muon systems are outside of the solenoid.

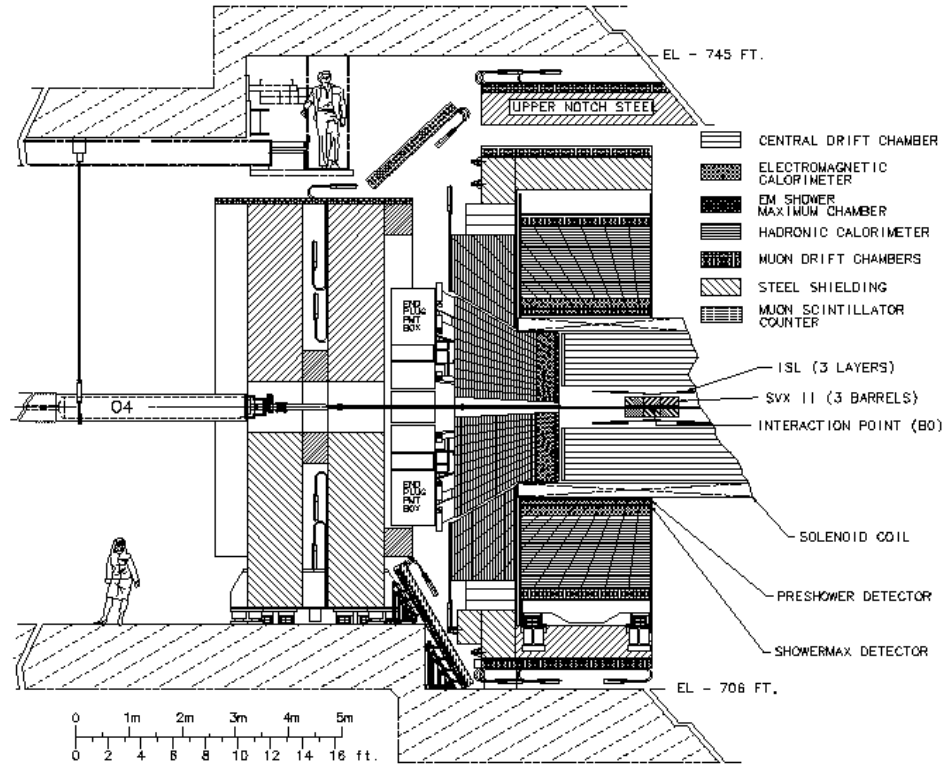


Figure 3.3: The CDF II detector

3.2.1 Coordinates and Units

The detector is shown in Figure 3.2 and Figure 3.3. CDF uses a coordinate system where the positive z -axis lies along the direction of the incident proton beam, ϕ is the azimuthal angle, θ is the polar angle (measured around the detector center in the plane of the beam axis), and p_T is the component of momentum in the transverse plane. A commonly used transformation of θ is $\eta = -\ln\left(\tan\frac{\theta}{2}\right)$. A brief description of the detector devices starting from the beam with emphasis on subsystems relevant to this analysis follows.

3.2.2 Tracking Systems

Efficient and precise charged particle tracking is at the heart of the CDF detectors purpose. A catalog of applications of this tracking important to this analysis include

- The ability to combine tracks with calorimetry and / or muon chamber information in order to provide efficient electron and muon identification with high purity both during triggering and offline reconstruction.

- Precise reconstruction of track impact parameters and efficient reconstruction of tracks in dense jets allowing the ability to identify the delayed decay of B mesons and thereby tag jet flavor.
- Efficient and precise reconstruction of track momentum at both high and low p_T .
- The ability to make time-of-flight measurements to enable particle mass identification to assist in hadronic tau reconstruction

The tracking system includes the Central Outer Tracker (COT) (10) a cylindrical open cell drift chamber, Layer 00 (11) a single-sided silicon microstrip detector, the Silicon Vertex Detector (SVX) (12) a collection of five layers of double-sided silicon microstrip detectors and the Intermediate Silicon Layer (ISL) (13) a double-sided silicon microstrip detector. All of the tracking components are contained in a superconducting solenoid, 1.5 m in radius and 4.8 m in length, which generates a 1.4 T magnetic field parallel to the beam axis. This magnetic field causes charged particle tracks to bend based upon their momentum allowing the tracking system to perform measurements of the p_T of the particles.

3.2.2.1 The Silicon Detectors

The innermost component of the silicon detectors the Layer00 detector is attached to the beampipe at a radius of 1.1 cm and covers the range of $|n| < 4.0$. Covering the radius range of $2.4\text{cm} < r < 10.7\text{ cm}$ for the range of $|n| < 2$ are the 5 layers of the SVX detector. The ISL is between the SVX detector and the COT and aids with track linking between the SVX and the COT.

Each of the silicon detectors is made of doped silicon strips, single-sided in Layer00 and double-sided for the SVX and ISL layers. Charged particles entering the strips cause ionization which creates a pulse of current read out by integrated electronics readout chips. For the double-sided strips one side of the strip is arranged to provide position information in r and ϕ while the other side of the strip the crystals are set at either 90° or 1.25° angle stereo thus providing z position information. The entire system thus allows track reconstruction in three dimensions with impact resolution of $40\ \mu\text{m}$ including a $30\ \mu\text{m}$ contribution from the beamline and z_0 resolution of $70\ \mu\text{m}$ (14). The silicon detector is an important tracking component and is crucial to the b-tagging employed in this analysis by providing secondary vertex detection.

3.2.2.2 Central Outer Tracker: COT

Outside of the silicon detector and covering the $|\eta| \leq 1.0$ region and radii between 40 and 137 cm the COT replaced the CTC of Run 0 and Run I and was designed to cope with the increased luminosity environment of Run II. The COT is a 3.1 m long cylindrical drift chamber which includes 30,240 sense wires that run the length (in z) of the chamber between the two end plates. Approximately half of the wires are in the four axial “superlayers”, running along the z direction, and half are in the four small angle (2°) stereo superlayers. Each superlayer is divided

Calorimeter Subsystem	CEM	CHA
η coverage	$ \eta < 1.1$	$ \eta < 0.9$
η segmentation	0.11	0.11
ϕ segmentation	15°	15°
Energy absorbing layer	$\frac{1}{8}$ in. lead	1 in. iron
Scintillating layer	5 mm	10 mm
Total radiation lengths	$19\chi_0$	$4.5\lambda_0$

Table 3.1: Calorimeter Summary - Central Calorimeters

in ϕ into “supercells”, with each supercell having sense wires and field wires configured for an approximately COT constant maximum drift distance of 0.88 cm.

Charged particles traveling through the mixed argon / ethane gas produce electrons which are then accelerated by the voltage maintained on the field wires towards the sense wires. Both the sense and field wires are 40 μm diameter gold plated tungsten. The sense wires span the length of the COT and register the current produced when electrons arrive at the wires as “hits”. The cells in the axial superlayers provide information on the r and ϕ of the hit and the stereo superlayers allow reconstruction of the z position. The COT achieves a hit position resolution of approximately 140 μm and momentum resolution of $\sigma(p_T)/p_T^2 = 0.0015 (\text{GeV} / c)^{-1}$ (14). The COT also provides dE/dx information for the tracks which is used in particle identification for particles with $p_T > 2 \text{ GeV}$.

3.2.3 Time-of-Flight: TOF

Located just outside the COT system is CDF’s Time of Flight (TOF) detector. (24). It is a barrel of scintillator along the COT at 140 cm from the beam line, covering $|\eta| < 1$. It is composed of 216 individual bars, each covering 1.7 in ϕ . It measures the time of arrival of a particle at the scintillators with respect to collision time, when combined with the momentum and path length measured from the tracking system it allows for the determination of the mass of the particle. The resolution in the time-of-flight measurement is $\sim 100 \text{ ps}$, and it provides on the order of two standard deviation separation between K^\pm and π^\pm for momenta $< 1.6 \text{ GeV}/c$.

3.2.4 Calorimetry

Surrounding the tracking system outside of the solenoid are segmented electromagnetic and hadronic sampling calorimeters that measure the energy flow of interacting particles for $|\eta| < 3.64$. The central calorimeters (with the endwall hadronic calorimeter) cover $|\eta| < 1.1(1.3)$. The plug calorimeters cover $1.1 < |\eta| < 3.64$. All of the CDF II calorimeters are scintillator based meaning they work by having transiting particles interact with dense metal plates generating showers of particles which excite the scintillating material. The excited scintillating material then radiates photons as it returns to its ground state, measuring these photons then provides a

Calorimeter Subsystem	PEM	PHA	WHA
η coverage	$1.1 < \eta < 3.6$	$1.3 < \eta < 3.6$	$0.7 < \eta < 1.2$
η segmentation	0.11	0.2	0.25
ϕ segmentation	15° or 7.5°	15° or 7.5°	15°
Energy absorbing layer	4.5 mm lead	2 in. iron	2 in. iron
Scintillating layer	4.5 mm	6 mm	10 mm
Total radiation lengths	$21\chi_0$	$7\lambda_0$	$4.5\lambda_0$

Table 3.2: Calorimeter Summary - Plug and Endwall Calorimeters

measure of the energy of the incident particle. The calorimetry system is crucial to accurate energy measurement of many physics objects at CDF. The properties of the calorimeters are summarized in Table 3.2.

3.2.4.1 Central Calorimeter: CEM & CHA

The Central Electromagnetic calorimeter (CEM) (15) covers the $|\eta| < 1.1$ region with full ϕ coverage. It is organized into projective towers each covering 15° in ϕ and 0.1 units in η . Each tower has 30 layers of $\frac{1}{8}$ in. thick lead and 31 layers of 5 mm SCSN-38 polystyrene scintillator for a total radiation length of $18\chi_0$. Between the eighth lead layer and the ninth scintillator layer, at the depth corresponding to maximum average transverse shower development ($5.9\chi_0$), a proportional strip chamber is inserted to determine shower position and transverse development by measurement of charge deposition on orthogonal strips and wires. The CEM achieves an energy resolution of $13.5\%/\sqrt{E_T} \oplus 2\%$ (14).

The Central Hadron calorimeter (CHA) (16) covers the $|\eta| < 0.9$ region and full ϕ coverage. It is organized into projective towers each covering 15° in ϕ and 0.1 unit in η matching the CEM calorimeter which directly precedes it. Each tower has 32 layers of 2.5 cm thick steel and 1.0 cm thick doped PMMA scintillator for a total depth of $4.7\lambda_0$. The CHA achieves an energy resolution of $75\%/\sqrt{E_T} \oplus 3\%$ (14).

3.2.4.2 Plug Electromagnetic Calorimeter: PEM

A part of the Run II upgrades for the CDF detector, the Plug Electromagnetic calorimeter (PEM) (17, 18) covers the $1.1 < |\eta| < 3.6$ region using scintillator tiles. Each tower has 23 layers of 4.5 mm lead and 4 mm scintillator for a total radiation length of $21\chi_0$. The tiles of the first layer are made out of 10 mm thick scintillator, read out separately from the rest of the PEM and used as a pre-shower detector. Behind the 4th lead plate (approximately $6\chi_0$ in) a shower-max position detector (PES) composed of plastic scintillator strips is inserted. The PEM achieves an energy resolution of $16\%/\sqrt{E_T} \oplus 1\%$.

3.2.4.3 Plug and Endwall Hadronic Calorimeter: PHA & WHA

The Plug Hadronic calorimeter (PHA) (17, 18) covers the $1.3 < |\eta| < 3.6$ region matching the PEM geometry. Each tower has 23 layers of 5.08 cm. iron and 6 mm scintillator for a total depth of $7\lambda_0$. The PHA achieves a energy resolution of $74\%/\sqrt{E_T} \oplus 4\%$.

The Endwall Hadronic calorimeter (16) covers the $0.7 < |\eta| < 1.2$ region. Each tower has layers of 5 cm thick steel and 1 cm thick doped PMMA scintillator for a total depth of $4.7 \lambda_0$. The WHA achieves an energy resolution of $75\%/\sqrt{E_T} \oplus 3\%$ (14).

3.2.5 Shower Maximum Detector

Included as part of the electromagnetic Calorimetry systems are proportional wire strip chambers, the shower maximum detector (CES). (22) These chambers are embedded in the calorimeter, at a depth equivalent to $5.9 X_0$, the point where a 15 GeV electron shower is expected to have its maximum energy deposition.

Overall the CES is composed of 128 strips, 69 in the section close to the central plane of the detector and 59 in the outer section. The CES is an important part of hadronic tau decay reconstruction as it allows for the definition of the impact of position of π^0 's. Previous studies have revealed the combination of calorimetry and CES to be capable of resolving photons from π^0 decay and even ρ mesons. (23) It also plays an role in the triggering systems, especially for electrons.

3.2.6 Muon Detection Systems

The muons detection systems form the final layer of detectors at CDF, located outside of the tracking and calorimetry systems. This is in order to exploit the fact that muons deposit very little energy in the calorimetry system and are relatively long lived, so they typically escape the detector systems. Therefore by mounting the muon systems outside of the other systems it isolates muon signals from those created by other particle interactions. The muon chambers are a combination of drift chambers and plastic scintillation counters. The drift chambers form the basis for identification of a muon and the scintillation counters are used to associate a given drift chamber signal with a particular bunch crossing, acting to identify muon signals from cosmic ray muons as opposed to muons produced in the interaction. The CMU and CMP systems both cover $|\eta| \leq 0.6$. The CMX system covers the range $0.6 \leq |\eta| \leq 1.0$ and the IMU system covers the range $1.0 \leq |\eta| \leq 1.5$ (14).

3.2.7 Cherenkov Luminosity Counter: CLC

CDF determines the beam luminosity using the Cherenkov Luminosity Counters (CLC) (19) which measure the average number of inelastic $p\bar{p}$ collisions per bunch crossing. The counters surround the beampipe in three concentric layers with 16 counters in each layer, for a total of 48 conical Cherenkov counters in each CLC detector. The entire system consists of two

modules that are located in the “3-degree holes” inside the CDF end-plug calorimeters in the forward and backward region of $3.7 < |\eta| < 4.7$. Charged particles traversing these modules coming from the $p\bar{p}$ interactions (primaries) will traverse the full length of the counter, emitting Cherenkov light and generating a large amplitude signal in the attached photomultiplier tubes (PMT). Particles from beam-halo interactions or from secondary interactions of prompt particles in detector material and the beam-pipe (secondaries) are softer, traverse at larger angles with shorter path lengths (thereby emitting less Cherenkov light) and their light will undergo a larger number of reflections before reaching the PMTs. This produces several differences between the signal produced by primaries and secondaries. Firstly, their signals are significantly smaller in amplitude and can be discriminated with suitable amplitude thresholds in the electronics. Secondly, when two primaries traverse a single counter the resultant signal is twice that of a single particle allowing distinct peaks for the different particle multiplicities to be discerned in the output.

The instantaneous luminosity (L) can be expressed as

$$L = \frac{\mu \times f_{bc}}{\sigma_{in}}, \quad (3.1)$$

where μ is the average number of $p\bar{p}$ interactions per bunch crossing, f_{bc} is the Tevatron bunch crossing frequency (1.515×10^7 Hz) and σ_{in} (approx. 60 mb (20)) is the inelastic $p\bar{p}$ interaction cross-section. Multiple separate methods for measuring μ through the CLC are possible. Two different methods are described here.

Firstly, since μ is the mean of a Poisson distribution the probability of empty crossings is $P_0(\mu) = e^{-\mu}$. By measuring the fraction of empty crossings a measurement of μ can be made and therefore the luminosity. However, the disadvantage of this method is the small probability of empty crossings at high luminosity, making a precise measure of luminosity using this technique difficult. Alternatively, μ can be interpreted as

$$\mu = \frac{\bar{N}}{\bar{N}^s}, \quad (3.2)$$

where N is the measured average number of hits per bunch crossing and N^s is the average number of hits from a single $p\bar{p}$ collision (measurable at low luminosity).

The data used in this thesis corresponds to $\simeq 6.2 \text{ fb}^{-1}$ of measured integrated luminosity, the uncertainty on this luminosity is 5.9% with 4.4% from the acceptance and operation of the CLC (20) and 4.0% from the uncertainty on the calculation of the total $p\bar{p}$ inelastic cross section (21).

3.3 Triggering

During Run II the Tevatron typically operated in a high luminosity environment, requiring the use of trigger systems to restrict data and read out of the full detector systems to a small proportion of the data. To accomplish this CDF uses a three level trigger systems with each tier

performing a more comprehensive treatment of the incoming data and accepting proportionally fewer events. Since most of the incoming data is not of physics interest, the intent of the trigger system is to select among incoming events for events of interest to various searches that are undertaken at CDF.

In the high luminosity operating environment of the Tevatron it is necessary to parse the incoming data and read out the full detector systems on only a small proportion of the data in order to maintain functionality. To accomplish this CDF uses a multitiered triggering system with each tier completing progressively more thorough reconstruction and accepting progressively fewer events, see Figure 3.4 and 3.5. CDF's triggering system has three levels, the level 1 trigger system is based on customized electronics, does relatively little reconstruction and is designed to target an accept rate below 28 kHz. The level 2 trigger system is based on a PC, does moderate reconstruction and is designed to target an event acceptance rate below 900 Hz. The final level 3 trigger system uses a farm of PCs, does a more complete reconstruction and is designed with a 200 Hz acceptance rate target.

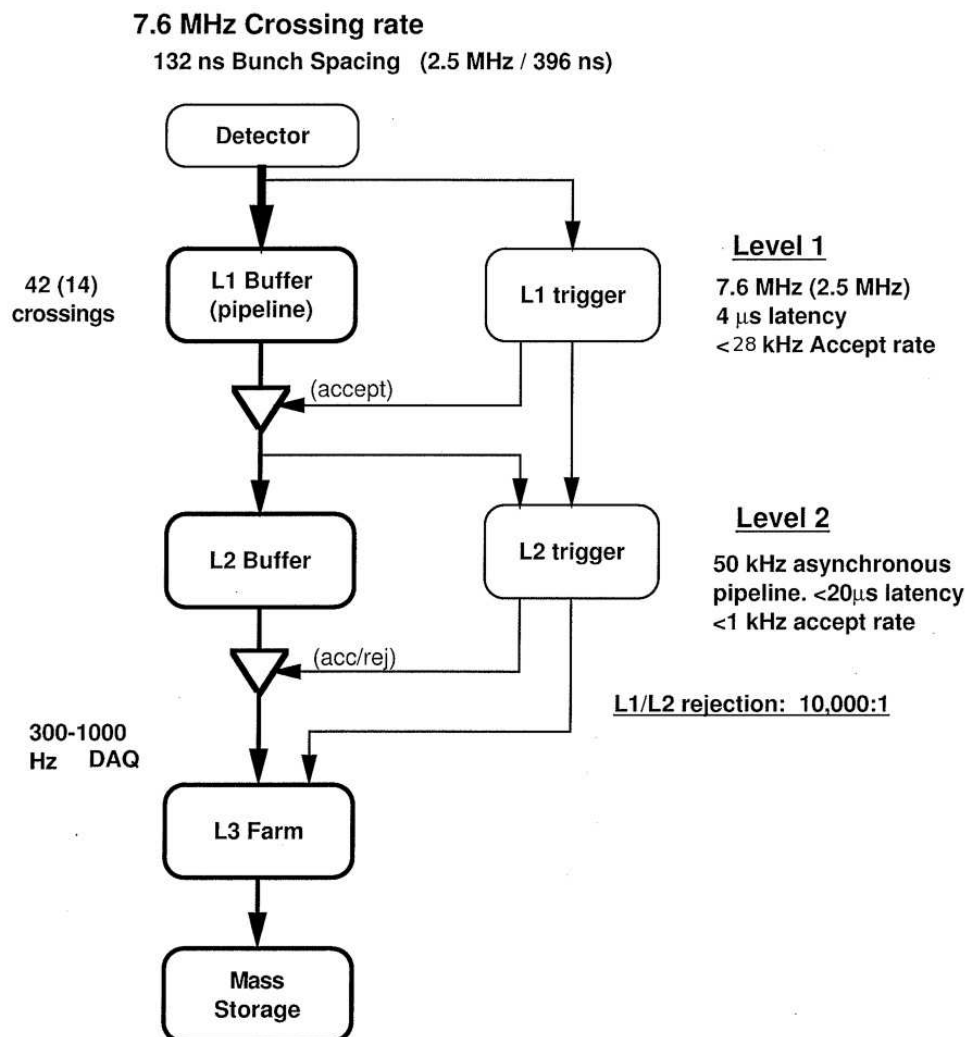


Figure 3.4: The CDF II Trigger system

3.3.1 Level 1 Trigger

The Level 1 trigger is a synchronous hardware based system that uses custom electronics to make a decision on every beam crossing, with the purpose of reducing the resultant acceptance rate below 28 kHz. The L1 decision pipeline is approximately 4 μ s, with a correspondingly deep buffer of 14 crossings. Different hardware elements partially process subsets of the full detector information in order to produce a rough picture of aspects of interest in the event. The global Level 1 decision then takes the different level 1 conditions into account to decide the global level 1 pass.

The overall L1 system is divided into three parallel tracks focusing on different elements of the detector the L1 CAL system, which focuses on the calorimetry information, the L1 TRACK system, which focuses on the COT tracking system and the L1 MUON system which searches for muon objects. Since the calorimetry and muon systems require tracks pointing to relevant elements, they receive the track information as well.

The Level 1 calorimeter trigger is intended to trigger on electrons, photons, jets, total transverse energy (E_T) and missing transverse energy (\cancel{E}_T). The triggers are divided into two types: object triggers (electrons, photons and jets) and global triggers (E_T and \cancel{E}_T). The object triggers are formed from individual calorimeter towers while the global triggers are formed by summing energies from all towers. The object triggers can then be further subdivided into single object triggers, where a single object is sufficient to generate a L1 accept, and do-object triggers, where the rate is sufficient that two or more such objects are required to generate a L1 accept. The electron and photon triggers are formed from applying thresholds to the electromagnetic (EM) energy while the jet triggers apply thresholds to the total (EM+hadronic (HAD)) energy in a tower. To further reduce rates Level 1 eXtremely Fast Tracker (XFT) tracks are available for matching to towers and towers with significant HAD energy can be rejected. The global triggers use the total (HAD + EM) energy in all the towers.

The Level 1 track trigger is intended to detect tracks on the COT. It uses hits from 4 axial layers of the COT to identify tracks with p_T greater than 2 GeV/c. The resultant track is then sent to the Extrapolation Module (XTRP) (32) which then distributes the XFT track information to the Level 1 and Level 2 trigger systems that use it. As well as providing track extrapolations to the muon and calorimeter systems the XTRP can generate a L1 accept if there are more than 6 tracks of any kind or based on P_T and ϕ information and a lookup table to generate various Level 1 triggers.

The Level 1 muon system uses muon detector primitives generated variously from the CMU, CMP, CMX, CSX, CSP and HAD systems and XFT information from the XTRP to form basic muon trigger objects. For the scintillators (CMP, CSX, CSP, HAD) primitives are derived from single or coincident groups of hits. For the wire chambers (CMU, CMX) primitives are obtained from hit patterns on the projective wires, with a requirement imposed on the difference in the

arrival times of signals. This time difference requirement imposes a minimum p_T requirement for hits from a single track.

3.3.2 Level 2 Trigger

The Level 2 trigger is an asynchronous system that processes events that have received L1 accepts in a First In - First Out (FIFO) manner. It has a buffer of four events to minimize downtime due to L2 time-outs and uses two stage design, first a dedicated hardware stage, the PULSAR (PULSer And Recorder) boards which operate on the outputs of the L1 system and secondly a PC based decision making process. In addition to the information available at and from L1, at L2 data from the shower max chambers, the Silicon Vertex Tracker (SVT) and XFT 3D stereo information are used to further refine the event selection.

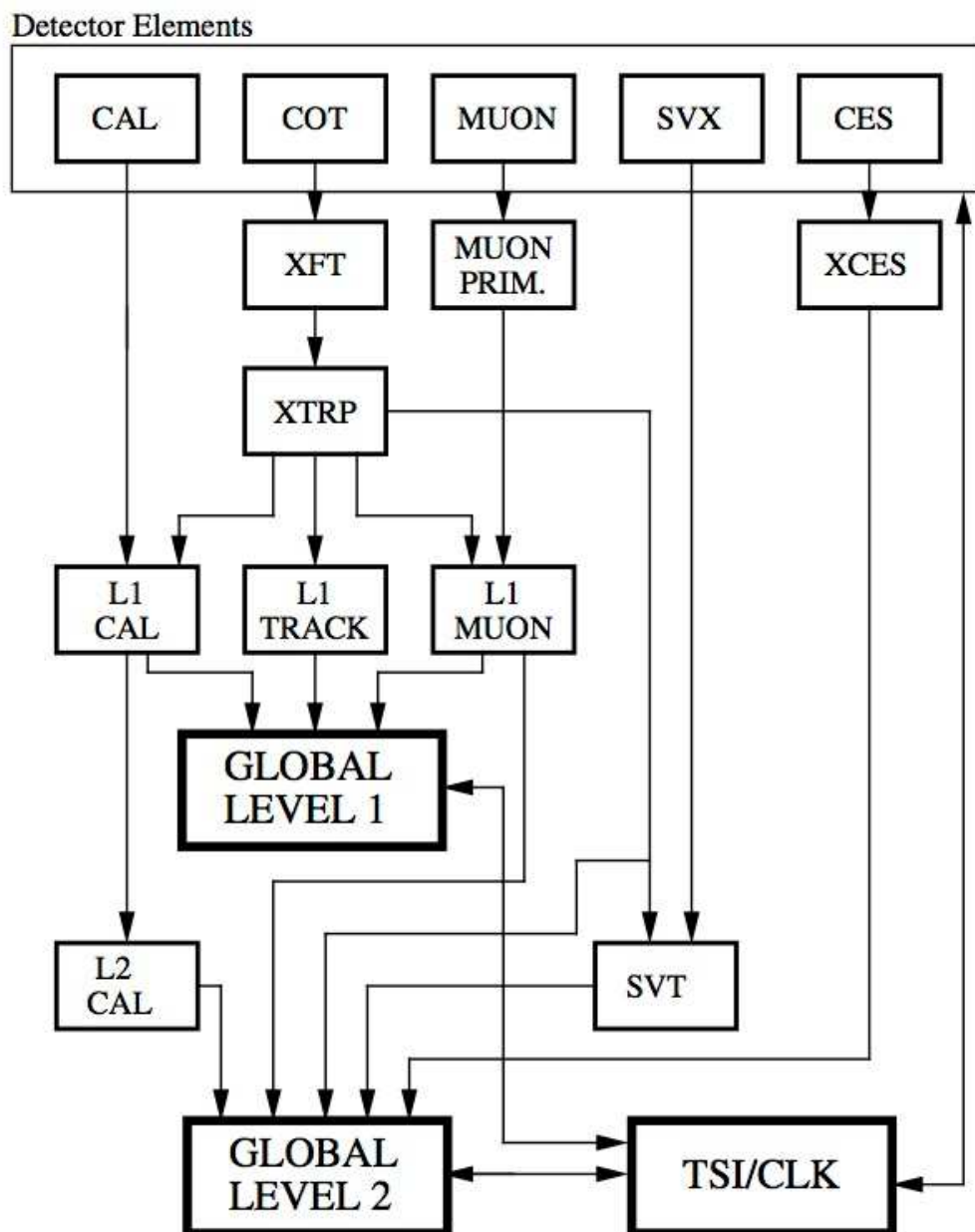
Additional primitives are generated from three systems at Level 2, the Level 2 cluster finder, L2CAL, the shower maximum strip chambers, XCES and the Silicon Vertex Tracker (SVT). The current L2CAL PULSARs receive the tower information at nearly the same time as the L1CAL, they serialize the data and upon receiving a L1 accept pass it on to the L2PC (30). This allows for near offline quality calorimetry information available at L2. The jet clustering algorithm uses a single pass clustering approach similar to that used in L3 and offline. First it selects seed towers as those towers above a certain seed threshold, then add energies from a fixed cone around the seed tower to form the jet energy. For electromagnetic (electron or photon) clusters the clustering algorithm is intended to resemble the DCAS hardware algorithm. Finally the system also calculates \cancel{E}_T .

The shower maximum detector information is used to provide better spacial resolution than available from calorimeter towers. The XCES (33) pulsar boards sum the energy on adjacent CES wires and compare them against a threshold value around 4 GeV. That information is then matched against XFT tracks to produce a Level 2 trigger. The increased spatial resolution produced allows for a significant reduction in combinatorial background for electrons and photons.

The Silicon Vertex Tracker, SVT (34), uses hit data from the silicon detector systems and compares that against each XFT track to produce a transverse impact parameter measurement with resolution $50 \mu\text{m}$, comparable to that of offline tracks of $p_T > 2 \text{ GeV}$ that do not use Layer 00.

Finally the XFT Stereo system (35) uses the stereo layers of the COT to provide additional discriminating power. This is done through confirming that the L1 XFT track, created strictly from the axial layers, goes through the stereo layers at the expected locations and through usage of the angular inclination with respect to the beam pipe to measure the angle θ of the track and use this information to point the track to other detectors, in particular to parts of the muon system. Both of these are used at L2 to provide enhanced fake rate rejection.

RUN II TRIGGER SYSTEM



PJW 9/23/96

Figure 3.5: The CDF II Level 1 and Level 2 Trigger system

3.3.3 Level 3 Trigger

After passing level 2 an event is sent to the level 3 triggers where it is read out completely. This begins with collecting data from all of the VME Readout Buffers (VRBs) which is then passed into the Event Builder (36) Scanner CPUs. The event builder is divided into 16 sub farms each consisting of one converter node and sixteen processor nodes, each converter node receives the VME data from the Scanner CPUs and then sends it forward to one of the processor nodes. There the Level 3 trigger reconstruction is applied, taking advantage of the full detector information with improved resolution, including a full 3-dimensional track reconstruction, and matching of tracks to parts of the calorimeter and muon-system information. Events that satisfy Level 3 trigger requirements are then transferred into the Consumer Server/Data Logger (CSL) system for storage. The average processing time per event in L3 is on the order of a few seconds. Some triggers which would otherwise consume more bandwidth than desired receive predefined or dynamic prescales at this level, that is effectively an additional numerical rejection factor applied on a trigger specific level. Dynamic prescales are pre scales that are adjusted on the fly based on available bandwidth.

The full set of requirements that an event has to fulfill at Level 1, Level 2 and Level 3 constitutes a trigger path. Approximately 200 such trigger paths are implemented in the CDF system and an event is accepted if it passes any of the trigger paths. It is possible for an event to pass more than one such trigger path. An event will be accepted if it passes the requirements for any one of these paths and depending on the trigger path will be stored in a trigger dataset. A complete description of the different datasets at CDF can be found in (37). The trigger paths that are relevant to this study are the SUSY_DILEPTON trigger path and the “lepton+track” trigger path which shall be described in more detail in chapter 5.

Event Selection

As outlined in the introduction this analysis involves three different final states in two different channels, namely the $\tau_e\tau_{had}$, $\tau_\mu\tau_{had}$ and $\tau_e\tau_\mu$ final states. where τ_e represents a tau that decays to an electron, τ_μ a tau that decays to a muon and τ_{had} a tau that decays hadronically. It follows the tagged and untagged channel for each state of these three final states for a total of six different channels.

Data for this analysis comes from two different trigger paths with different trigger requirements. These impose efficiency effects that must be modeled in simulated data sets, a subject that will be discussed at length in the next chapter.

The total dataset used represents 5.9 fb^{-1} of data. Over this period there were a number of changes in the triggers that took place, including some changes to the pre-scales or disabling of certain trigger paths, as a result the luminosity varies slightly based on channel.

4.1 Datasets Used

For the exploration of the $\tau_e\tau_\mu$ channel we use data collected with the ‘‘SUSY dilepton’’ triggers: datasets *edilad*, *edilbh*, *edilai*, *edilaj*, *edilak*, *edilam*. The data is taken from the officially produced Stntuple samples.

The ‘‘SUSY dilepton’’ triggers select two leptons ($l = e, \mu$) with with $p_T > 4 \text{ GeV}$ (during period *i*, the threshold for one of the leptons was increased to 8 GeV). At least one of the leptons is in the central region. In this analysis we use only the trigger paths that select one electron and one muon, both in the central detector region. Same-flavor leptons are used for consistency checks and study of lepton isolation consistency between the data and MC.

For the final states with a hadronically decaying tau we use the ‘‘lepton+track’’ triggers that require a central electron or muon, and an isolated track (used as a starting point for tau reconstruction). These are found in the *etlpad*, *etlpbh*, *etlpai*, *etlpaj*, *etlpak*, and *etlpam* datasets.

In this analysis we use Run 2 data in the full run range and apply the Top/EWK/Exotics good run list v35 (good electron, muon, good Si required, excluded COT compromised runs). This run range has both the CMX and CMU+CMP systems operational. The integrated luminosity of our sample is 5.9 fb^{-1}

4.2 Monte Carlo Simulations

Monte Carlo simulations of the $\phi \rightarrow \tau\tau$ signal were generated using PYTHIA 6.216 separately for the processes $bb, gg \rightarrow A$ (PYTHIA process numbers 156, 157), which are expected to

have the largest contribution to the MSSM Higgs production cross section. The MC simulation includes run-dependence and minimum-bias overlay. We generated samples for $\tan\beta=0$ in the mass region $90 < m_A < 300$ GeV and then apply as appropriate a stacking technique to generate larger width samples. We selected this $\tan\beta$ for the purpose of future combination with the Higgs \rightarrow bbb search. When calculating signal detection efficiencies, we weight the contributions from $gg, b\bar{b} \rightarrow A + X$ according to the predicted relative contributions. For background estimation we use the EW group MC samples that also include run-dependence and overlay of minimum bias events.

4.3 Data-Monte Carlo Hybrid

Modeling of the $Z \rightarrow \tau\tau$ background in the tagged channel poses special challenges as a result of the relatively poor way in which background jets are modeled in available MC samples. Since these jets are the source of the tags that move an event into the tagged background sample it is important to model them accurately. In order to do so we employ a method designed to combine data-based background jets with MC samples of $Z \rightarrow \tau\tau$. We do this by constructing a hybrid data-MC sample composed of baseline events from $Z \rightarrow \mu\mu$ data composed with τ 's taken from $Z \rightarrow \tau\tau$ MC samples.

The process begins by selecting for $Z \rightarrow \mu\mu$ events from data samples from the *bhmucd*, *bhmuch*, *bhmuci*, *bhmucj*, *bhmubk* and *bhmubm* datasets. The data-level muons are then matched against simulated taus at the generator level. A metric is constructed to measure the closeness of the match between muon and tau as follows.

$$metric = \sqrt{\left(\frac{\Delta Pt}{5}\right)^2 + (\Delta\phi)^2 + (\Delta\eta)^2 + \left(\frac{\Delta Z}{40}\right)^2} \quad (4.1)$$

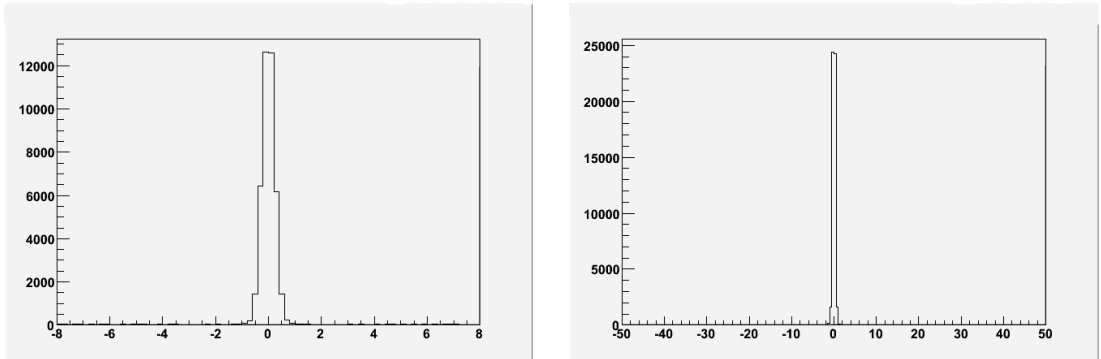


Figure 4.1: ΔZ and ΔPt between the data muons and simulated taus at the generator level

Each simulated tau is paired with whichever data muon it most closely matches. Each data muon is then paired with whichever associated tau has the smallest metric value. Then the muon is removed from the event, the simulated tau replaces it and any necessary event variables are

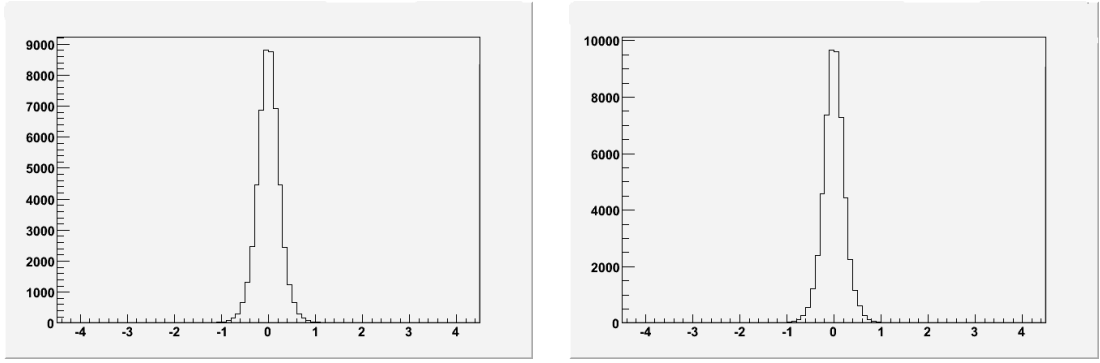


Figure 4.2: $\Delta\phi$ and $\Delta\eta$ between the data muons and simulated taus at the generator level

altered as appropriate. The differences between the final paired muons and final paired taus is shown in Figures 4.1 and 4.2

The resultant sample is then normalized at the pretag level to the pretag $Z \rightarrow \tau\tau$ MC to account for overall luminosity. This sample is then used as the $Z \rightarrow \tau\tau$ background for the tagged sample, and sets how many events are removed from the pretag $Z \rightarrow \tau\tau$ MC to make the untagged sample.

Chapter 5

Trigger Efficiencies**5.1 Introduction**

This chapter presents a measurement of the trigger efficiency of the track leg of the “lepton plus track” trigger paths. We measured the efficiency of these trigger paths with respect to fully reconstructed τ s using jets and di-lepton samples. We defined relevant variables to account for inefficiencies of the XFT track matching, L2 cluster matching and L3 isolated track finding. The overall trigger efficiency is the product of those three components.

The trigger efficiencies for the SUSY_DILEPTON paths were not remeasured for this analysis but taken from other sources. (38, 39)

5.1.1 Trigger paths description

The “lepton plus track” dataset contains events from several different trigger paths. Three families of those paths are relevant for this analysis. Two of them require a μ and an isolated track, “CMUP plus track” and “CMX plus track”. A third family triggers on a central electron and an isolated track, “Electron plus track”. The paths involving μ s were “dynamically prescaled” or “luminosity enabled” in the last periods of data taking. The whole list of trigger paths studied can be found in table 5.1.

Trigger Path Family	Trigger Paths involved
“Electron plus track”	TAU_ELECTRON8_TRACK5_ISO
“CMUP plus track”	TAU_CMUP8_TRACK5_ISO, tag 1 to 9 TAU_CMUP8_TRACK5_ISO_L2_LOOSE_DPS TAU_CMUP8_TRACK5_ISO_L2_LOOSE_LUMI_240 TAU_CMUP8_TRACK5_ISO_L2_LOOSE_LUMI_260
“CMX plus track”	TAU_CMX8_TRACK5_ISO TAU_CMX8_TRACK5_ISO_LUMI_200 TAU_CMX8_TRACK5_ISO_L2_LOOSE_DPS TAU_CMX8_TRACK5_ISO_L2_LOOSE_LUMI_200

Table 5.1: “lepton plus track” trigger paths used in this analysis

Different versions of these trigger paths have had different requirements. Only a few of them affected the track leg of the trigger. The “Electron plus track” triggers underwent a transition after run 209770, when the isolation requirements at level 3 were modified and a level 2 calorimeter cluster was required to match the XFT track. The “CMUP plus track” and “CMX plus track” trigger paths also suffered two relevant changes. First, a level 2 XFT track was included simultaneously for both μ families, in the transition from tag 7 to 8 of the TAU_CMUP8_TRACK5_ISO

L2 cluster requirements (old)	L2 cluster requirements (new)
$E_T > 4\text{GeV}$	$E_T > 5\text{GeV}$
Number of towers ≤ 5	No requirement on NTowers
pass = 2	pass = 13

Table 5.2: L2 cluster cuts.

path and from tag 6 to 7 of TAU_CMX8_TRACK5_SIO. Moreover, a second transition modified the level 3 isolation requirements after run 209770, simultaneous to the transition in the “Electron plus track”. These changes were accounted for in a previous study. (28) Subsequent to that and the focus of this study there were several changes. In the TAU_ELECTRON path in the change from v-10 to v-12 the clustering algorithm was updated to use pass 10 and pass 13 clusters for the electron and tau respectively. There were then minor changes to the trigger parameters in the change to v-13 (changed number of cluster tower requirements) and v-14 (changed ET requirement to 5 GeV from 4 GeV). The changes up through run 209770 were accounted for in previous studies. (25, 26, 27, 28)

In the TAU_CMX and TAU_CMUP paths there was the implementation of SLAM stereo confirmation after run 233108 with the 3DMatch requirement added after run 257202.

5.1.1.1 Level 2 Trigger Requirements

An XFT track with a $p_T > 5\text{ GeV}$ is required in all the different versions of the TAU_ELECTRON8_TRACK5_ISO trigger paths. It is also required from tag 8 of the path TAU_CMUP8_TRACK5_ISO and tag 7 of TAU_CMX8_TRACK5_ISO.

Moreover, this XFT track has to match a cluster for the path TAU_ELECTRON8_TRACK5_ISO, versions 8 and 10. This cluster has to fulfill the requirements summarized in table 5.2.

The TAU_ELECTRON cluster requirement was changed to pass 13 cluster with tag 12.

5.1.1.2 Level 3 trigger requirements

The level 3 trigger requirements are summarized in table 5.3. The isolation requirement is fulfilled when no shoulder tracks with meet the p_T and Z requirements are in the isolation annulus. The definition of the isolation annulus and the cuts applied to select shoulder tracks was modified after run 209770. We refer to the trigger settings before this run as the “old trigger” and to the ones after that change as “new trigger”. Table 5.4 shows the definition of isolation for both triggers.

5.1.2 Data Samples and Event Selection

For this trigger study, we chose to use jet samples because they do not include track related requirements in their trigger paths. Therefore, these events are not correlated with the “lepton plus track” sample. This dataset, however, has the inconvenience of being populated mainly by

L3 track requirements
$p_T > 5 GeV$
$ \eta < 1.5$
isolation

Table 5.3: Level 3 track cuts.

	“old trigger”	“new trigger”
L3 isolation annulus	$0.175 < \Delta R < 0.524$	$10degree < Angle < 30degree$
track cuts	$ \Delta Z < 15 cm$ $p_T > 1.5 GeV$	$ \Delta Z < 5 cm$ $p_T > 1.5 GeV$

Table 5.4: Isolation annulus definition, and cuts for shoulder tracks

fake τ s. This introduces a bias in the study of trigger level isolation, due to the differences in track multiplicity between jets and τ s. Moreover, a measurement of the efficiency of the level 2 calorimeter cluster requirement added to the “electron plus track” trigger path would be biased if measured in the jet samples.

We selected tight τ s in the runs marked as good by the “good run list, em mu” version 35. Note that tight τ ID includes offline replication of level 3 isolation. After selecting τ s, we checked whether those τ s would have passed the trigger requirements of the track leg of the different “lepton plus track” paths.

We also used high p_T samples of both μ s and electrons for obtaining the absolute normalization of the level 3 efficiencies. We selected events in the “good run list, em mu”, version 35, that had two almost-tight electrons or two almost-tight μ s with an invariant mass consistent with the Z mass peak. By almost-tight we mean that we applied all the standard ID cuts except isolation. For the tracks of each of the leptons, we calculated the isolation related variables we use for τ s. We applied the same isolation cuts we apply to τ s and then check whether these tracks would have passed the requirements in the “lepton plus track” paths.

5.1.3 Level 2 Trigger Efficiency

As previously stated, there are three kinds of requirements at level 2 that could potentially be applied in the different paths: XFT track matching, level 2 cluster matching and XFT SLAM matching.

We found the main source of XFT track finding inefficiency was related to the tracks crossing the central plane of the COT at the radius where the axial superlayers are located. After the addition of SLAM confirmation there was an additional effect when tracks crossed the central plane of the COT at the radius where the stereo superlayers are located. Therefore, when the tracks cross the $z = 0$ plane, we calculated and parametrized the efficiency in terms of the radius of crossing of the central plane of the COT, $RZ0$. When the tracks do not cross the central plane, then we found that the efficiency increases with the length of the track inside the COT.

parameter	old trigger	new trigger	SLAM
$\epsilon_{plateau}$	0.9548	0.9539	0.9445
A_1	0.2646	0.2563	0.086
C_1	58.92	58.91	58.38
S_1	2.3810	2.3504	2.5063
A_2	0.3468	0.3320	0.1643
C_2	82.17	82.23	82.08
S_2	2.6352	2.624	2.413
A_3	0.4823	0.4604	0.4060
C_3	105.8	105.8	105.5
S_3	2.796	2.812	2.527
A_4	0.4457	0.3854	0.3483
C_4	131.0	130.8	129.4
S_4	3.489	3.695	2.464
A_5	-	-	70.11
C_5	-	-	2.579
S_5	-	-	0.1882
A_6	-	-	93.64
C_6	-	-	2.771
S_6	-	-	0.2933
A_7	-	-	117.3
C_7	-	-	2.980
S_7	-	-	0.4348

Table 5.5: Fitted parameters for the L2 trigger efficiency as a function of $RZ0$.

The $RZ0$ efficiency, figure 5.1, shows a very well defined behavior: a plateau of very high efficiency with four dips. We fitted the distribution to a flat plateau and 4 Gaussians:

$$\epsilon(x) = \epsilon_{plateau} - \sum_{i=1}^4 A_i e^{-\frac{(x-C_i)^2}{S_i^2}}.$$

After the shutdown in August 2006, 3-layer XFT tracks were removed. This resulted in the dip corresponding to the 4th axial layer becoming more pronounced. Subsequently, SLAM confirmation was added, it also shows a well defined behavior: a plateau of high efficiency with seven dips. We fitted the distribution to a flat plateau and 7 Gaussians:

$$\epsilon(x) = \epsilon_{plateau} - \sum_{i=1}^7 A_i e^{-\frac{(x-C_i)^2}{S_i^2}}.$$

The fit shows the dips are precisely located at the radius where the axial and stereo super-layers of the COT are placed, table 5.5.

For the tracks that don't cross the $Z = 0$ plane, we used the path length of the track in the $r - z$ plane inside the COT, Lrz . The longer this path is, the higher the efficiency, figure 5.3.

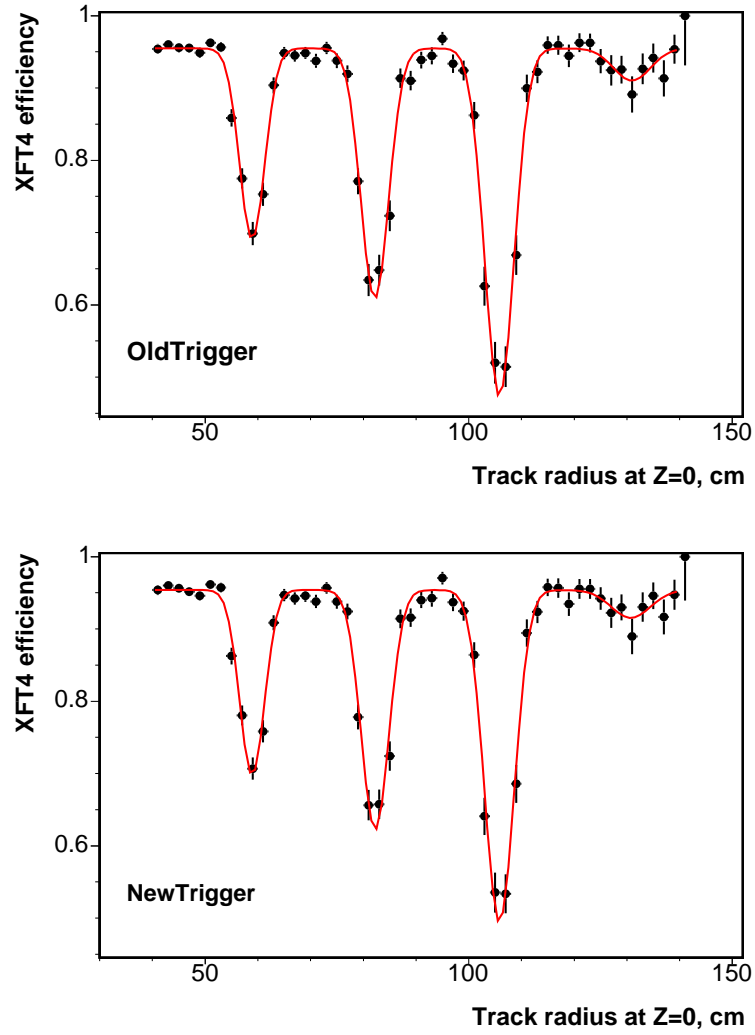


Figure 5.1: XFT track finding efficiency for tracks that cross the $Z = 0$ plane. We parameterized this efficiency as a function of the radius at which the tracks cross that plane, $RZ0$.

parameter	old trigger	new trigger
$\epsilon_{plateau}$	0.9750	0.9665
C	1.958	24.63
S	30.32	22.09

Table 5.6: Fitted parameters for the L2 trigger efficiency as a function of Lrz .

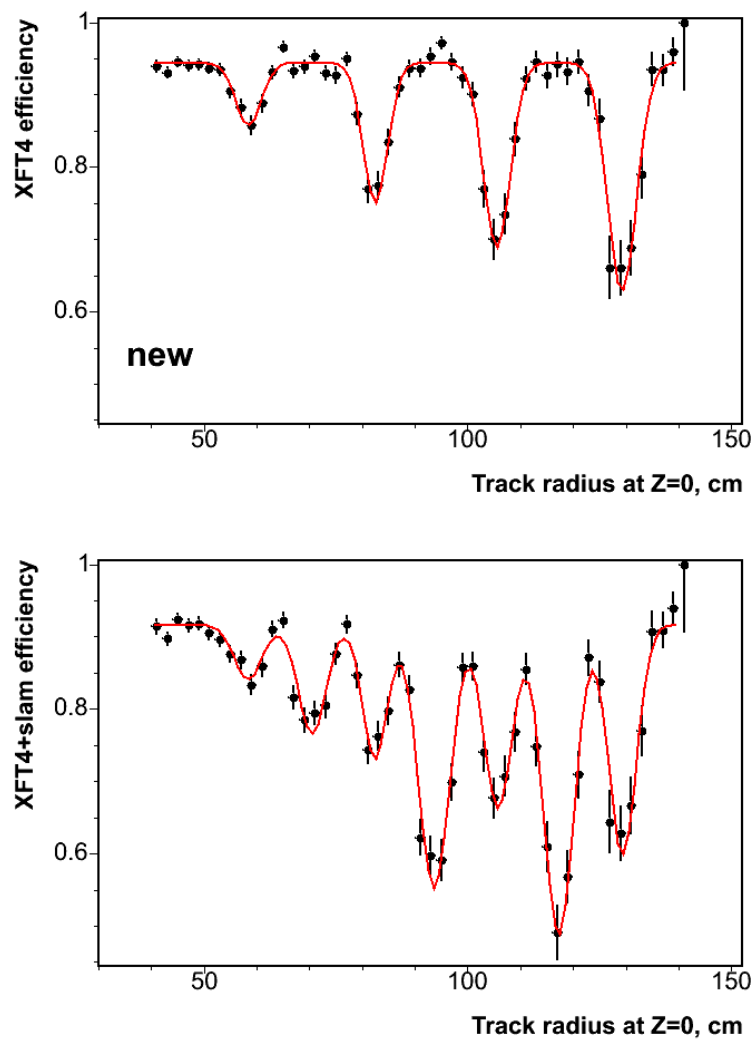


Figure 5.2: XFT track finding efficiency for tracks that cross the $Z = 0$ plane. We parameterized this efficiency as a function of the radius at which the tracks cross that plane, $RZ0$. Shown are the post-shutdown efficiency and the XFT4+SLAM efficiency.

Table 5.6 shows the result of the fit to a turn-on curve:

$$\epsilon(x) = \frac{\epsilon_{plateau}}{1 + e^{-\frac{C-x}{S}}}$$

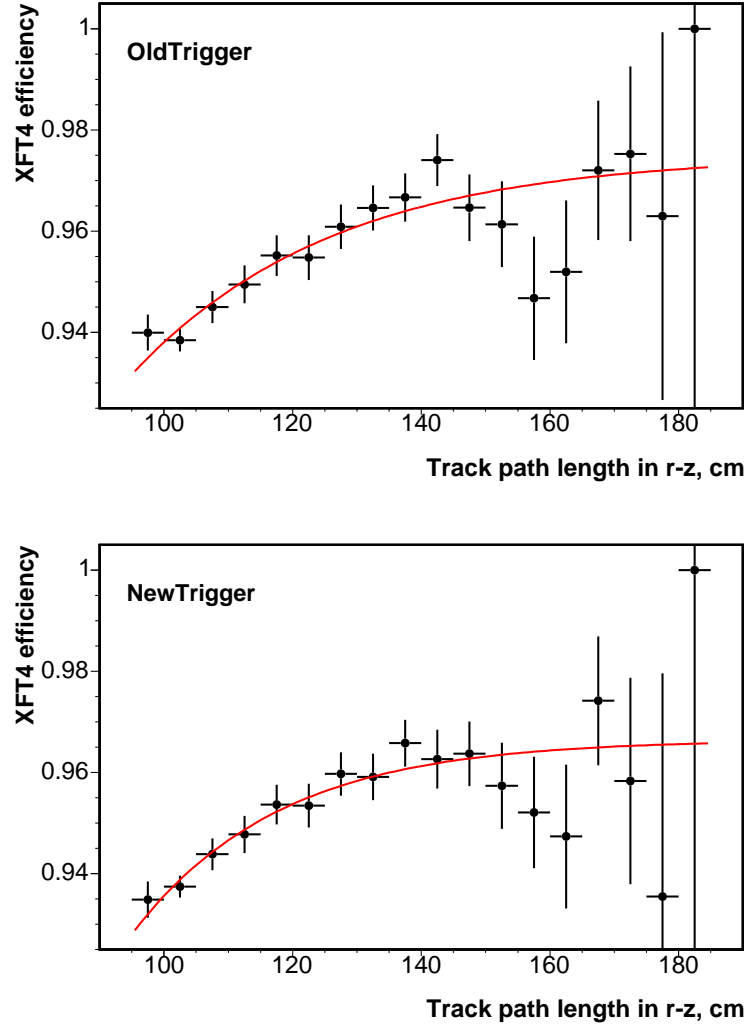


Figure 5.3: XFT track finding efficiency for tracks that do not cross the $Z = 0$ plane. We parameterized this efficiency as a function of the length of the track path in the $r - z$ plane.

After the removal of the XFT3 tracks we find that the path length turn-on is removed for tracks that don't cross the $Z = 0$ plane. We thus model the efficiency as a flat-plateau minus a gaussian. Table 5.7 shows the result of the fit

$$\epsilon(x) = \epsilon_{plateau} - Ae^{-\frac{(x-C)^2}{2S}}.$$

Regarding the cluster requirement, there is no dataset that would allow an independent measurement of the efficiency of a reconstructed τ to match a level 2 cluster with sufficient statistics. After several studies, we concluded that the only feasible way to approach this was relying on

parameter	SLAM
$\epsilon_{plateau}$	0.9448
A	0.07155
C	173.8
S	13.59

Table 5.7: Fitted parameters for the L2 trigger efficiency as a function of Lr_z .

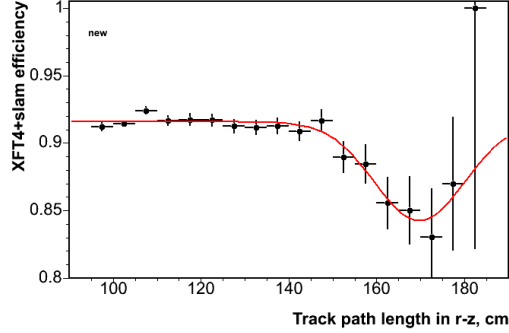


Figure 5.4: XFT track finding efficiency for tracks that don't cross the $Z = 0$ plane. We parameterized this efficiency as a function of the length of the track path in the $r - z$ plane.

Monte Carlo samples, like $Z \rightarrow \tau\tau$. Given that the simulation of the trigger, trigSim, is not fully consistent with data, we would have to scale our measurement of the trigger efficiency with a set of factors that can be obtained from QCD Monte Carlo samples and the Jet samples, figure 5.5.

The altered clustering algorithm resulted in a substantial improvement in the performance, as can be seen in figure 5.6

5.1.4 Level 3 Trigger Efficiency

The level 3 trigger requires a COT isolated track. As previously stated, there are two different implementations of isolation in our current datasets, corresponding to different time periods. We refer to them as “old trigger” and “new trigger”. The cuts applied for these two definitions of isolation are summarized in table 5.4. Some of the τ ID cuts we apply offline are tighter than the ones applied at L3, like p_T or η . In our range of acceptance, the trigger efficiency doesn't show a significant dependence on these variables.

However, L3 isolation is closely related to the goodness of the determination of the track parameters at trigger level. In the case when there are extra tracks in the signal cone, the variation of the parameters of these extra tracks could make them migrate from the signal cone at offline production level to the isolation cone at trigger level, leading to trigger inefficiency. Some parameters of the track like ϕ or the curvature, i.e. p_T , are determined much more precisely at trigger level than others, like $\cot\theta$. As it is shown in Figure 5.9 for instance, the trigger

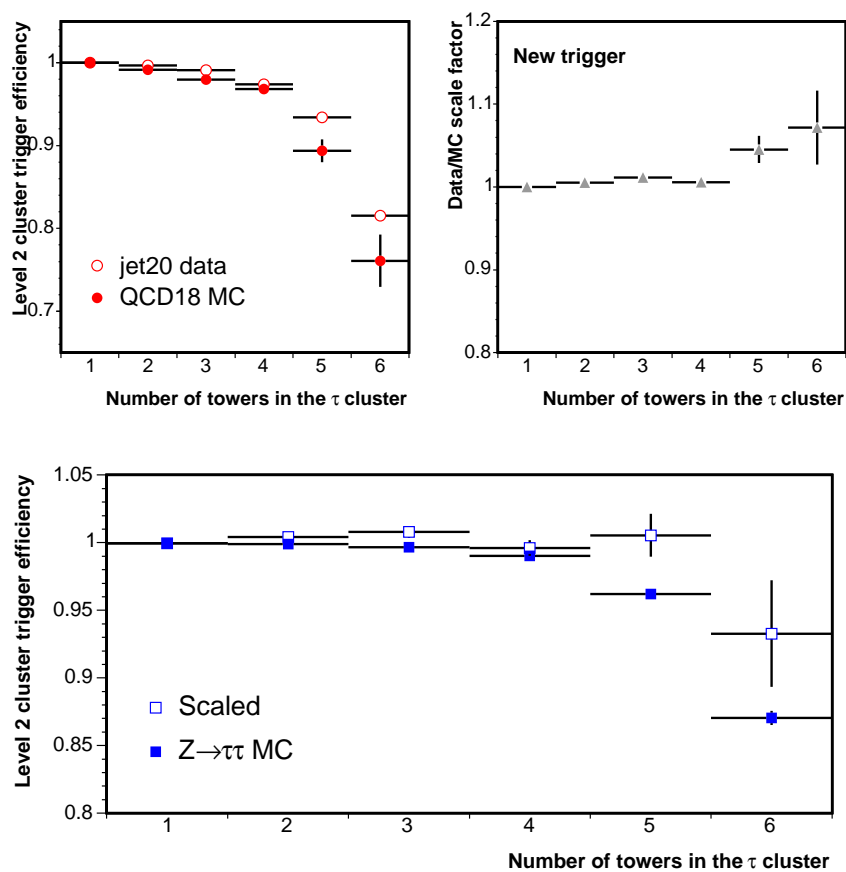


Figure 5.5: We compared the efficiency in Jet20 data and QCD 18 MC simulation (upper left). This was used to derive a scale factor as a function of the number of towers (upper right) in the τ cluster resulting in the corrected level 2 cluster trigger efficiency (lower).

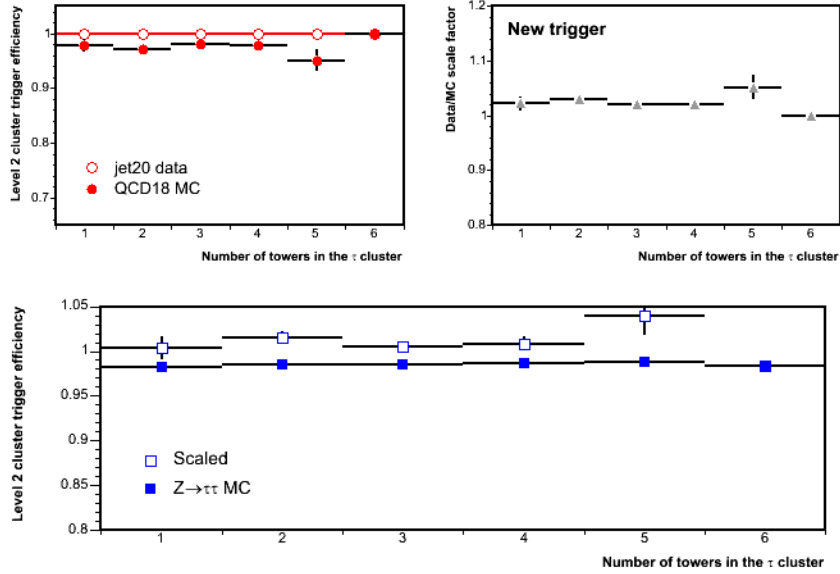


Figure 5.6: We compared the efficiency in Jet20 data and QCD 18 MC simulation (upper left) after the implementation of the pass 13 clustering algorithm. This was used to derive a scale factor as a function of the number of towers (upper right) in the τ cluster resulting in the corrected level 2 cluster trigger efficiency (lower).

efficiency is related to the closeness of the extra tracks in the signal cone to the boundary of the cone. Moreover, the presence of tracks due to multiple interactions also has a dramatic impact on the efficiency of this trigger.

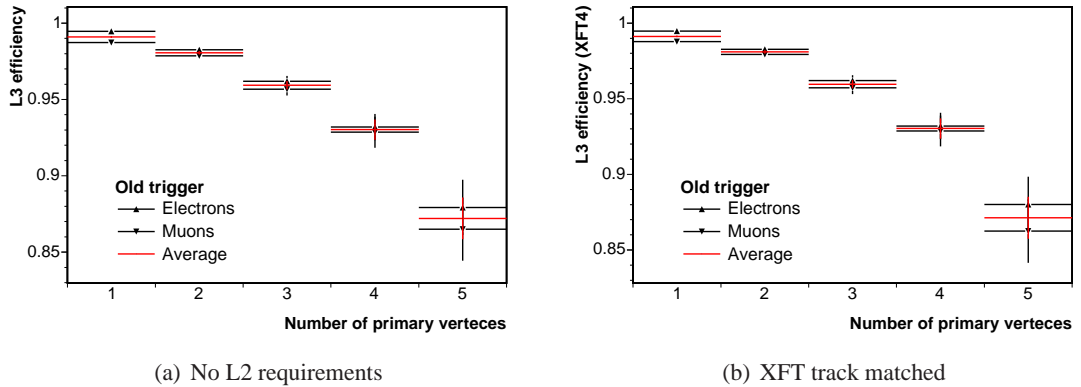


Figure 5.7: L3 efficiency parameterized in terms of the number of primary vertexes for the old trigger.

We selected events with 2 almost-tight electrons or two almost-tight μ s in the high-Pt samples. By almost-tight we mean we applied all standard cuts, except isolation. Then for each of the leptons in the event, we defined a 10° cone, and created τ -like signal and isolation variables: number of tracks in the signal cone, number of tracks in the isolation cone, sum of the p_T of the tracks in the isolation cone and sum of the E_T of π^0 in the isolation cone. We measured the

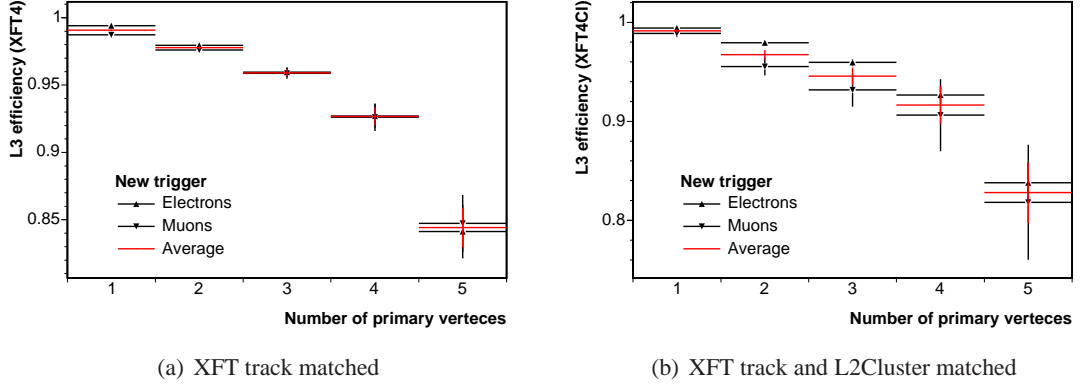


Figure 5.8: L3 efficiency parameterized in terms of the number of primary vertices for the new trigger.

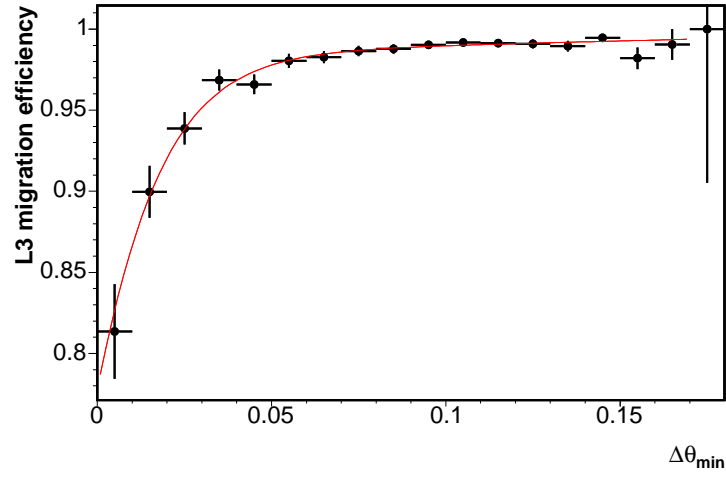
trigger efficiency for the tracks of those leptons after applying τ -like isolation cuts as a function of the number of primary vertices. This environment is closer to our signal, but it only compares to the jets samples in the 1-prong high- p_T region. This measurement of the efficiency takes into account tracks that could lay in the isolation annulus, both tracks from other interaction, from the underlying event or fake tracks.

We account for track migration as a source of inefficiency by looking at the closeness of the extra tracks in the τ signal cone to the boundary. For the “old trigger”, we calculated the $\Delta\theta$ of each extra track to the L3 signal cone boundary. We parameterized the efficiency as a function of smallest $\Delta\theta$ among those tracks, $\Delta\theta_{min}$. For the new trigger, the cone is defined in *angle*, instead of ΔR . The natural variable to parameterize the efficiency in this case is, then, the angle to the cone boundary of the closest track to the boundary in the cone, $\Delta\alpha_{min}$. For these measurements we ran over the events of the jet samples. However, calculating the efficiency in the jet samples could introduce a bias in our measurement because of the differences in track multiplicity between jets and τ s. Most of the τ s we reconstruct are fakes, which are more likely to fail trigger requirements because of the presence of low p_T tracks in the trigger isolation cone. In order to avoid this bias, and to make this “track migration” efficiency multiplicative with the overall efficiency we obtained from the jet samples, we only used τ candidates that were surrounded by a very clean environment. This condition was achieved by requiring no extra tracks in a cone of $\Delta R = 0.7$

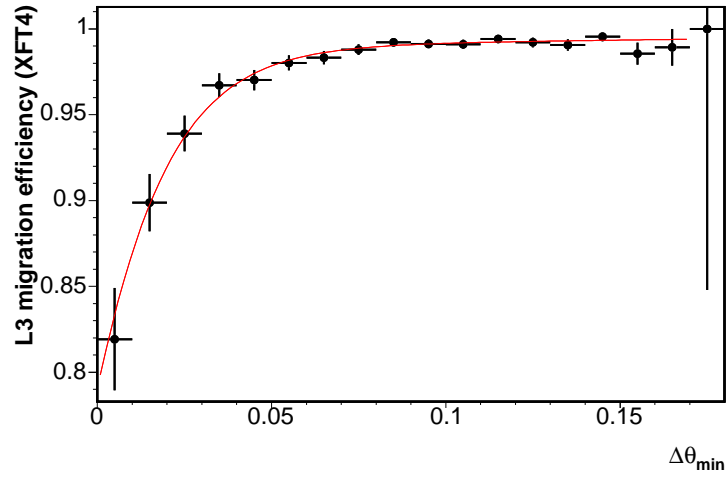
Both the overall efficiency and the track migration need to be calculated for each different set of L2 and L3 requirements. Figure 5.7 shows the L3 efficiency for the “old trigger” and Figure 5.8 for the “new trigger”, considering the different L2 requirements in each trigger path.

Figure 5.9 and Figure 5.10 show the “L3 migration” efficiency in terms of $\Delta\theta_{min}$ and $\Delta\alpha_{min}$, fitted to a turn-on function:

$$\epsilon(x) = \frac{\epsilon_{plateau} + \epsilon_{slope} \times x}{1 + e^{-\frac{C-x}{s}}}$$



(a) No L2 requirements

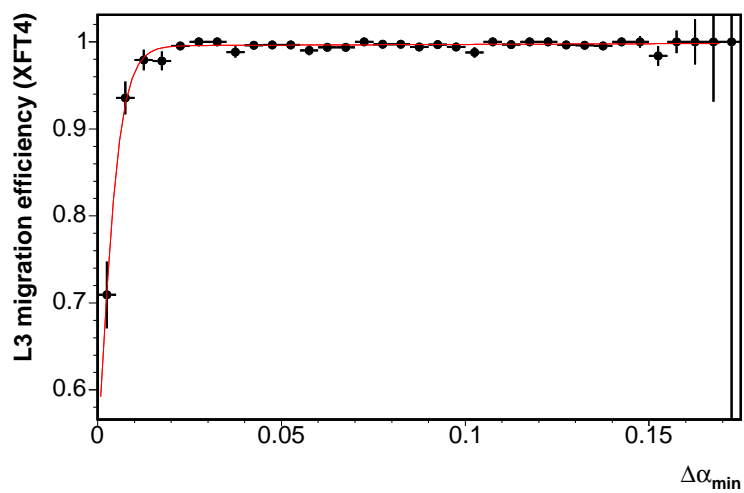


(b) XFT track matched

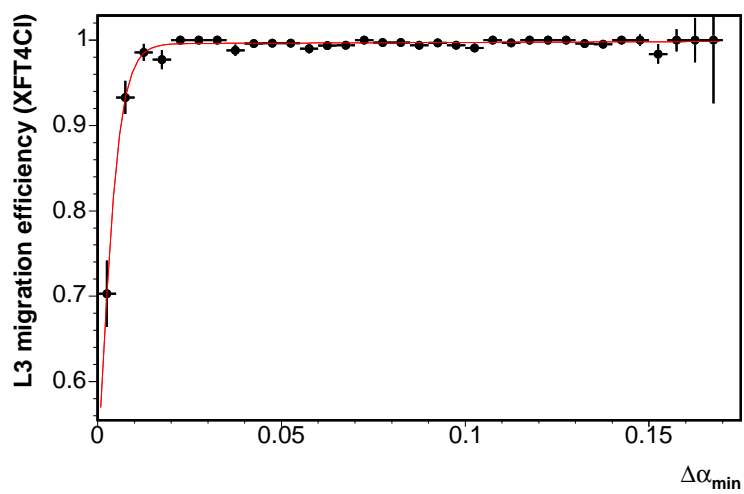
Figure 5.9: L3 “migration” efficiency for the “old trigger”, parameterized in terms of $\Delta\theta_{min}$.

parameter	“old trigger”		“new trigger”	
	no L2	XFT	XFT	XFT+L2Cluster
$\epsilon_{plateau}$	0.9848	0.9896	0.9955	0.9958
ϵ_{slope}	-2.011×10^{-2}	-2.312×10^{-2}	-2.991×10^{-4}	3.9491×10^{-5}
C	1.517×10^{-2}	1.678×10^{-2}	2.985×10^{-3}	2.7921×10^{-3}
S	5.272×10^{-2}	2.543×10^{-2}	1.598×10^{-2}	1.5801×10^{-2}

Table 5.8: Results of the fits to $\Delta\theta_{min}$ and $\Delta\alpha_{min}$.



(a) XFT track matched



(b) XFT track and L2Cluster matched

Figure 5.10: L3 “migration” efficiency for the “new trigger”, parameterized in terms of $\Delta\alpha_{\min}$

The results of the fits are shown in table 5.8.

5.1.5 Electron Trigger Issue

A small portion of the electron + track trigger encountered a software problem for a short data period. Because of this, events with $|\eta(track) - \eta(e)| \sim 0$ were rejected. The problem was found and fixed fairly quickly. To avoid this effect we make a cut $|\eta(track) - \eta(e)| < 0.3$ to cover this region in data from the affected period. The same cut is applied to MC, weighted to the appropriate amount of luminosity. We confirmed this issue is modeled in various kinematic distributions.

Chapter 6

Particle Identification**6.1 Introduction**

In contrast to other leptons, taus have a rich decay spectrum. There are two groups of decays: leptonic ($\tau \rightarrow l\nu_\tau\nu_l(\gamma)$, $l = e, \mu$) and hadronic ($\tau \rightarrow X_h\nu_\tau$, X_h =system of hadrons). Throughout this note we use τ_e , τ_μ and τ_{had} as shorthand notations for taus detected in a particular decay channel.

The combinations of tau decay modes determine the detection channels for $\phi \rightarrow \tau\tau$ - Table 6.1 .

Mode	Fraction (%)	Comment
$\tau_e\tau_e$	3	high DY $\rightarrow ee$ bg
$\tau_\mu\tau_\mu$	3	high DY $\rightarrow \mu\mu$ bg
$\tau_e\tau_\mu$	6	low QCD bg
$\tau_e\tau_{had}$	23	golden
$\tau_\mu\tau_{had}$	23	golden
$\tau_{had}\tau_{had}$	41	large multi-jet bg's

Table 6.1: Tau decay mode combinatorics and their importance for $\phi \rightarrow \tau\tau$ searches.

The largest contribution comes from $\tau_{had}\tau_{had}$, however, detection in this mode is difficult due to large QCD backgrounds. The modes $\tau_e\tau_{had}$ and $\tau_\mu\tau_{had}$ are the golden ones - they have significant contribution and contain an electron/muon that helps suppress multi-jet events. Despite its relatively small contribution, $\tau_e\tau_\mu$ is very interesting because it provides very efficient QCD suppression.

The modes $\tau_e\tau_e$ and $\tau_\mu\tau_\mu$ are not very useful at CDF due to their small contributions and high ee and $\mu\mu$ DY backgrounds (in addition to $\tau\tau$ DY).

The particles of interest in this analysis are electrons (from τ_e), muons (from τ_μ), and the products of hadronically decaying taus. The selection criteria for electrons and muons closely follows the JP recommendations. Our minimum p_T (E_T) requirements for muons and electrons are set to 6 GeV for the $\tau_e\tau_\mu$ channel, and to 10 GeV for the $\tau_{had}\tau_{e/\mu}$ channels.

We apply the standard cuts for tight medium- and high- p_T leptons (excluding isolation), and use the common CDF reconstruction and identification data/MC scale factors. The results for electrons and muons can be found in Ref. (40) and Ref. (41). Muon reconstruction efficiencies are consistent in the high- and medium- p_T samples, and we use the data/MC scale factors as quoted in Ref. (42)

For the electron and muon selection in the $\tau_e\tau_\mu$ channel we do not apply calorimeter isolation and use fixed track isolation cuts instead: $I_{trk}^{0.4} = \sum p_T^{iso} < 2 \text{ GeV}$, where the sum is over all tracks within $\Delta R < 0.4$ and $\Delta z_0 < 5 \text{ cm}$ of the muon or electron track. For the $\tau_l\tau_{had}$ channels, we additionally apply the calorimeter isolation as defined for low/medium- p_T leptons (40, 41).

6.1.1 Electrons

The following is a list of the electron ID cuts used in the analysis.

Electron cuts

- $E_T > 10.0 \text{ GeV}$ for $\tau_l\tau_{had}$, $E_T > 6.0 \text{ GeV}$ for $\tau_e\tau_\mu$
- $p_T > 8.0 \text{ GeV}$ for $\tau_l\tau_{had}$, $p_T > 5.0 \text{ GeV}$ for $\tau_e\tau_\mu$
- $E_{had}/E_{EM} < 0.055 + 0.00045 * E$
- $L_{shr} < 0.2$
- $E/P < 2.0$ (no cut if $E_T > 50 \text{ GeV}$)
- $-3 < q\Delta X < 1.5 \text{ cm}$
- $|\Delta Z| < 3 \text{ cm}$
- $\chi_{CESstrip}^2 < 10$
- $|z_0| < 60 \text{ cm}$
- $|d_0^{corr}| < 0.2 \text{ cm}$
- $|z_{COT}| < 140.0 \text{ cm}$
- $\geq 3 \text{ stereo}$, 2 axial layers (≥ 5 hits)
- $E_{rel}^{iso} < 0.1$ or $E_T^{iso} < 2.0 \text{ GeV}$, not applied for $\tau_e\tau_\mu$
- $\sum p_T^{iso} < 2 \text{ GeV}$ (cone 0.4)
- satisfy fiduciality requirements
- not from conversion

Conversion removal is applied to electron candidates by forming all possible oppositely charged track pairs and rejecting the candidate if at least one satisfies $|S_{XY}| < 0.2 \text{ cm}$, $|\Delta\lambda| < 0.04$.

The data/MC scale factor of the fixed track isolation cut is determined from ee in the Z mass peak. We use data from the SUSY dilepton ee sample and the EW group $Z/\gamma \rightarrow ee$ MC

Cut	Efficiency
Conversion	0.971 ± 0.001
Fiducial	0.987 ± 0.001
TrkAxSeg	0.9989 ± 0.0004
TrkStSeg	1 ± 0
E_{had}/E_{EM}	0.993 ± 0.001
Isolation	0.973 ± 0.002
L_{shr}	0.991 ± 0.001
E/P	0.934 ± 0.003
ΔZ	0.9979 ± 0.0005
$q\Delta X$	0.9986 ± 0.0004
$\chi_{CESstrip}^2$	0.967 ± 0.002
Total	0.799 ± 0.002

Table 6.2: Measured ID and isolation efficiencies for electrons

samples. The electrons are required to pass the full electron ID except for isolation. We find that the MC describes the data quite well and obtain a data/MC scale factor of 0.997 ± 0.001 for the track isolation cut.

For this type of isolation there should be no dependence on electron E_T as illustrated in Figure 6.2 (shown later in the text), where we plot the scale factor as a function of electron E_T . To reduce backgrounds in the low- and intermediate- E_T region, we select only back-to-back electron pairs ($\Delta\phi > 3.0$). We would like to note that this distribution is for demonstration purposes to show that there is no general E_T -trend. The $E_T < 15$ GeV region is probably more sensitive to the background subtraction rather than the efficiency ratio itself. The other issue regarding electrons is the data/MC energy scale. The plots on Figure 6.1 show the invariant mass of lepton pairs and the data/MC agreement in the position of the Z -peak (after applying the corrections recommended on the JP page).

For the combined ID and isolation cuts we obtain an overall data efficiency of 0.799 ± 0.002 a MC efficiency of 0.814 ± 0.001 and an overall scale factor of $0.981 \pm 0.003(stat.) \pm 0.004(syst.)$, further details are in table 6.2 (43). In actual implementation we apply the standard Joint Physics scale factor implementation to apply a luminosity weighted average based on luminosity profiles as appropriate for some of our MC, period specific scale factors range from 0.96 to 1.011.

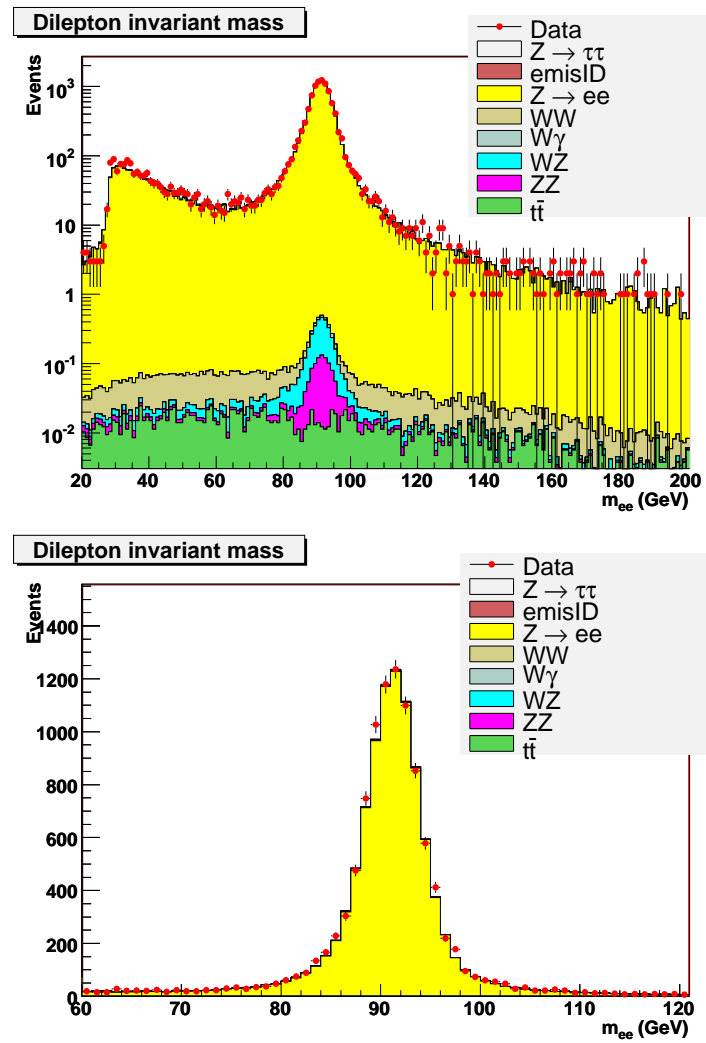


Figure 6.1: Invariant mass of the selected electron pairs (1 fb⁻¹ sample).

6.1.2 Muons

The analysis uses central muons reconstructed in the CMU+CMP and CMX detectors.

Muon cuts

- $p_T > 10.0$ GeV for $\tau_l\tau_{had}$, $p_T > 6.0$ GeV for $\tau_e\tau_\mu$
- $|z_0| < 60$ cm
- $|d_0^{corr}| < 0.2$ cm
- $\sum p_T^{iso} < 2$ GeV (cone 0.4)
- $E_{rel}^{iso} < 0.1$ or $E_T^{iso} < 2.0$ GeV, not applied for $\tau_e\tau_\mu$
- ≥ 3 stereo, 2 axial layers (≥ 5 hits)
- $\rho_{COT} > 140$ cm

$p_T > 20$ GeV

- $E_{EM} < 2 + \max(0, 0.0115 * (p - 100))$ GeV
- $E_{had} < 6 + \max(0, 0.028 * (p - 100))$ GeV
- $|\Delta X_{CMU}| < 3$ cm and $|\Delta X_{CMP}| < 7$ cm (CMUP)
- $|\Delta X_{CMX}| < 6$ cm (CMX)

$p_T < 20$ GeV

- $E_{EM} < 2$ GeV
- $E_{had} < 3.5 + (p_T/8.0)$ GeV
- $|\Delta X_{CMU}| < 3$ cm **or** $\chi_{CMU}^2 < 9.0$
- $|\Delta X_{CMP}| < 7$ cm **or** $\chi_{CMP}^2 < 9.0$
- $|\Delta X_{CMX}| < 6$ cm **or** $\chi_{CMX}^2 < 9.0$

Just as in the electron case we measure the additional data/MC scale factor for the track isolation requirement from events in the Z -peak and get a data/MC scale factor of 1.00 ± 0.001 .

As expected the scale factor has no p_T dependence. The distribution, together with the results for electrons is shown in Figure 6.2. The di-muon mass distributions in the data and MC are in good agreement - Figure 6.3.

The ID and isolation efficiencies are obtained in two regions, the high pt region corresponding to $p_T > 20$ and the intermediate region, $p_T \leq 20$ and are summarized in table 6.3 (41, 42). From these we obtain an average scale factor of 0.986 ± 0.01 for high pt muons and 0.914 ± 0.034 for low pt muons, though again as with the electrons we apply a luminosity weighted scale factor for some period specific MC.

	$p_T \leq 20$		$p_T > 20$	
	CMUP	CMX	CMUP	CMX
EM energy	0.9923 ± 0.0021	0.9962 ± 0.0027	0.9749 ± 0.0018	0.9682 ± 0.0026
Had energy	0.9930 ± 0.0021	0.9859 ± 0.0035	0.9837 ± 0.0015	0.9825 ± 0.0019
COT hits	0.9950 ± 0.0019	0.9822 ± 0.0035	0.9959 ± 0.0008	0.9998 ± 0.0002
d0	0.9897 ± 0.0041	0.9856 ± 0.0070	0.9971 ± 0.0006	0.9962 ± 0.0011
Stub matching	0.9805 ± 0.0032	0.9986 ± 0.0045	0.9758 ± 0.0023	0.9947 ± 0.0011
Isolation	0.8672 ± 0.0080	0.8999 ± 0.0134	0.9739 ± 0.0018	0.9714 ± 0.0024
Reconstruction	0.9101 ± 0.0075	0.9691 ± 0.0064	0.9336 ± 0.0029	0.9446 ± 0.0033
Total ID	0.8290 ± 0.0095	0.8171 ± 0.0137	0.9097 ± 0.0033	0.9188 ± 0.0040

Table 6.3: Measured ID and isolation efficiencies for medium and high p_T muons

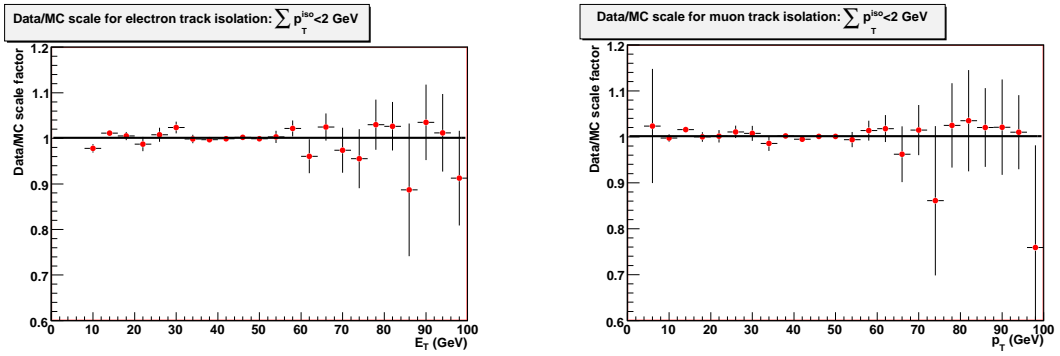


Figure 6.2: Data/MC scale factor for track isolation of electrons (left), and muons (right). The scales are plotted as a function muon p_T (electron E_T).

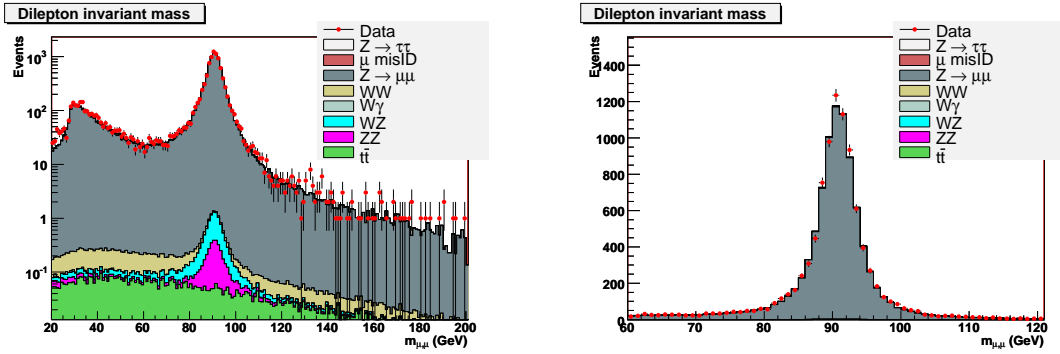


Figure 6.3: Invariant mass of selected muon pairs (1 fb⁻¹ sample).

6.1.3 Taus

Here and below “tau reconstruction” refers to the reconstruction of the visible decay products X_h of taus experiencing semi-hadronic decays: $\tau \rightarrow X_h \nu_\tau$. X_h can be a π^\pm/K^\pm , or some short-lived intermediate resonance that decays directly (or through some intermediate states) to final states containing $\pi^{\pm,0}, K^{\pm,0}$.

Details on the tau reconstruction procedure can be found in (26) and the references therein. The selection criteria used in this analysis are similar, with the exception of the mass cut in the 3-prong taus, and the track isolation requirement. Here we only list the selection cuts as used in this analysis and the derived data/MC scale factors.

Tracks and π^0 's in the signal cone are used to construct the four-momentum of the hadronic system. The four-momentum is used in subsequent event cuts and for the determination of the mass of the system $M(\text{trks} + \pi^0\text{s})$. In some cases there is a non-negligible energy loss due to π^0 reconstruction inefficiency (mostly when they hit near the edges of the CES detectors). Therefore, in some cases one has to apply corrections to the measured tau energy from tracks and π^0 's, as discussed in (45). Here we apply similar (but simplified) corrections.

Corrections are mostly needed for the 1-prong tau decays, and we correct the energies only in this case using information on the energy deposited in the tau calorimeter cluster. We use two corrections that are applied only in cases when the energy in the calorimeter cluster is larger than the estimate from tracks+ π^0 's. First, we want to account for the case with possible π^0 losses. This correction is applied when we have substantial EM energy in the cluster ($E_{EM}/E_{tot} > 0.2$). In this case we assign as tau p_T the sum of the energy of the charged track and the EM energy contained in the cluster (minus MIP energy). To avoid overestimation due to large EM energy deposition from the track, we require that $E_{had} > 0.3p^{trk}$. In cases where the conditions for this correction are not met we look for cases of potentially large hadronic energy contribution (possibly due to K_L): $p^{trk} < E_{had} - \sigma_{had}$, where $\sigma_{had} = 0.5\sqrt{E_{had}}$. In this case we assign E_T^{cl} as tau p_T instead of $p_T(\text{trks} + \pi^0\text{s})$.

We define the variable ξ' to suppress electrons and muons depositing large amount of EM energy.

$$\xi' = \frac{E_{tot}}{\sum |\vec{p}|} \left(0.95 - \frac{E_{EM}}{E_{tot}} \right), \quad (6.1)$$

where E_{tot}, E_{EM}, E_{had} are the total, electromagnetic and hadronic tau cluster energies, and \vec{p} are the momenta of charged tracks associated with the tau.

To suppress electrons accompanied by bremsstrahlung, we reject 1-prong tau candidates if a π^0 candidate with $|\Delta z_{CES}| < 2.0$ cm of the projection of the track **and** in ϕ lies between the CES intersect of the track helix and its tangential. To account for CES position, and track extrapolation resolution, the veto region is extended by 0.01 rad beyond the points of the tangential intersect track hit in CES. This procedure is similar to the one used in (46) (p.14). The

track in one-prong taus in the $\tau_e\tau_{had}$ channels are restricted to the fiducial part of the CES detector $|x_{CES}| < 21$ cm. This restriction is imposed to avoid the effect of deficiencies in the simulation of detector response to electrons near the ϕ cracks.

The following is a summary of the tau reconstruction and ID cuts.

Tau cuts

- $E_T^{seed\ twr} > 6.0$ GeV
- $E_T^{sh\ twr} > 1.0$ GeV
- $N^{twr} \leq 6$
- $\theta_{sig} = \min(0.17, \frac{5.0 \text{ rad/GeV}}{E^{\tau\ cl}})$ rad ¹
- $\theta_{iso} = 0.52$ rad
- $p_T^{seed\ trk} > 6.0$ GeV ²
- $p_T^{sh\ trk} > 1.0$ GeV
- $E_T^{\tau\ cl} > 9.0$ GeV
- $p_T > 15.0$ GeV for 1-prongs, $p_T > 20$ GeV for 3-prongs
- $\Delta z^{sh\ trk} < 5.0$ cm
- $9.0 < |z_{CES}^{seed\ trk}| < 230.0$ cm
- traverse all 4 axial SL's in COT
- $\sum p_{T,trk}^{iso} < 2$ GeV, no tracks with $p_T > 1.5$ GeV
- $\sum E_{T,\pi^0}^{iso} < 1$ GeV
- $N_{sig}^{trk} = 1, 3$
- $|\sum Q^{trk}| = 1$
- $M(\text{trks} + \pi^0s) < 1.8$ GeV
- $\xi' > 0.1$

¹To prevent the signal cone from becoming too small and sensitive to track/ π^0 direction resolution we set limits $0.05 < \theta_{sig}$ rad for tracks, and $0.1 < \theta_{sig}$ rad for π^0 's

²Seed track quality: ≥ 3 stereo, ≥ 2 axial layers with at least 5 hits

Tau detection efficiency is affected by the requirements imposed on tracks and π^0 's in the isolation annulus. Possible difference between data and MC can appear due to deficiency in the simulation of the underlying event and multiple interactions. To compare data and MC we select muons and electrons from $Z \rightarrow \mu\mu$ and $Z \rightarrow ee$ events and compare the tau-style isolation efficiencies. In this case the isolation annulus is fixed to be between $10^\circ - 30^\circ$ degrees with respect to the selected lepton. In principle this comparison can be done by randomly selecting regions of the detector, but the use of Z events ensures environment that is similar to our event selection.

The electrons (or muons) are required to have opposite charge, pass the standard tight ID cuts for high- p_T leptons (up to isolation), and have an invariant mass $66 < M_{ll} < 116$ GeV.

For the selected leptons we replicate the L3 isolation offline (just like for tau selection) and determine the data/MC scale factors and uncertainties for the isolation requirements $\sum p_{T, trk}^{iso} < 2$ GeV, $\sum E_{T, \pi^0}^{iso} < 1$ GeV. The isolation efficiencies obtained from electrons and muons as a function of number of primary vertices are shown in Figure 6.4 and 6.5. One can clearly see the deterioration with increased number of interactions in the event. For practical purposes we derive one single scale factor and uncertainty by integrating over all vertex multiplicities. The average scale factor from electrons and muons is $\epsilon_{data}^{iso}/\epsilon_{MC}^{iso} = 0.989 \pm 0.001$ (runs < 209769), and $\epsilon_{data}^{iso}/\epsilon_{MC}^{iso} = 0.984 \pm 0.001$ for (runs > 209769).

The same procedure is used to determine the scale factor for the offline replication of the L3 isolation requirements, given that the tau isolation requirements are satisfied. These give results of $\epsilon_{data}^{L3 iso}/\epsilon_{MC}^{L3 iso} = 0.997 \pm 0.001$ for the period of the ‘‘old trigger’’ (runs < 209769), and $\epsilon_{data}^{L3 iso}/\epsilon_{MC}^{L3 iso} = 0.999 \pm 0.001$ (runs > 209769).

Tracks with $p_T > 1.0$ GeV from the underlying event and multiple interactions can contribute to track ‘‘multiplicity migration’’ if they are contained in the signal cone. The number of additional tracks in a 10° cone is compared with respect to the muon direction and an average of 0.025 ± 0.013 additional tracks are found in the data, and 0.027 ± 0.003 in the MC. This corresponds to an uncertainty in tau selection efficiency due to ‘‘multiplicity migration’’ of 0.3%.

Hadronic scale uncertainty in the MC affects tau acceptance through the requirement on minimum tau cluster energy, tau seed tower E_T threshold, and the ξ' cut. In the previous iteration we found an uncertainty of 2%, consistent with the result obtained in (48).

The effect of the cut on the mass of the hadronic tau decay products $m(trks + \pi^0$'s) on data and MC is examined using a sample of taus from W decays. The data is selected with the ‘‘tau+MET’’ trigger. For this test the 0h+0i samples are used. Tau ID is the same as for the Higgs search, except for a higher threshold on the seed track: $p_T > 10$ GeV due to the trigger requirements. To suppress multi-jet backgrounds we impose tight event cuts: $\cancel{E}_T > 30$ GeV, no extra jets with $E_T > 5$ GeV in the detector. The latter requirement introduces a large dependence on the modeling of jet multiplicities (including very soft jets), that complicates the exact determination of tau yields in data and MC. Since we are not attempting to measure

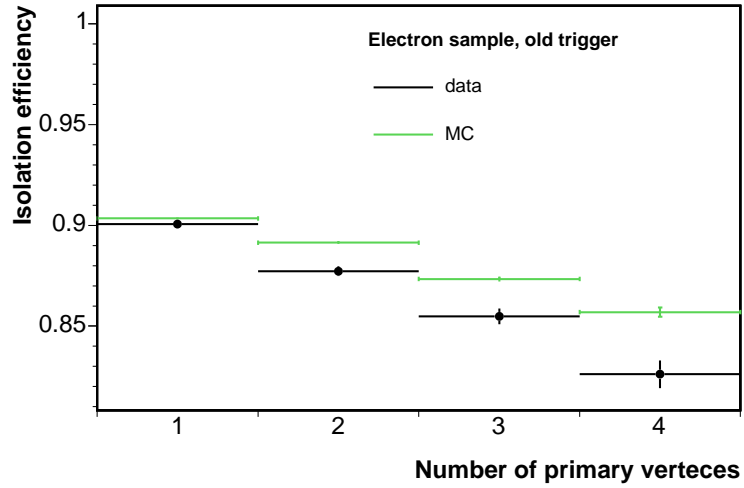
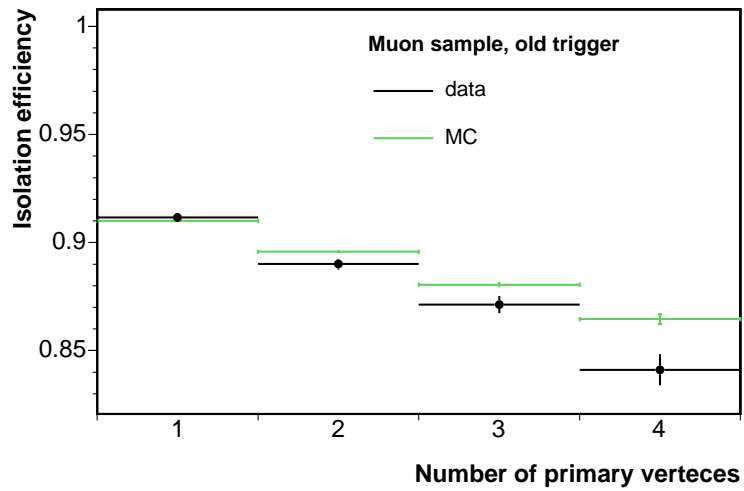
(a) Efficiency measured with $Z \rightarrow ee$ events, run < 209769(b) Efficiency measured with $Z \rightarrow \mu\mu$ events, run < 209769

Figure 6.4: Comparison of the efficiency of the $\sum p_{T, trk}^{iso} < 2 \text{ GeV}$, $\sum E_{T, \pi^0}^{iso} < 1 \text{ GeV}$ cuts in data and MC using $Z \rightarrow ee, \mu\mu$ events (1.8 fb^{-1} sample).

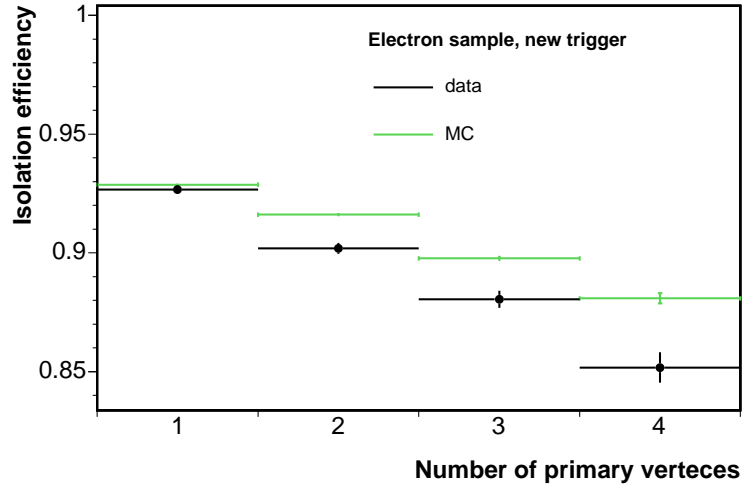
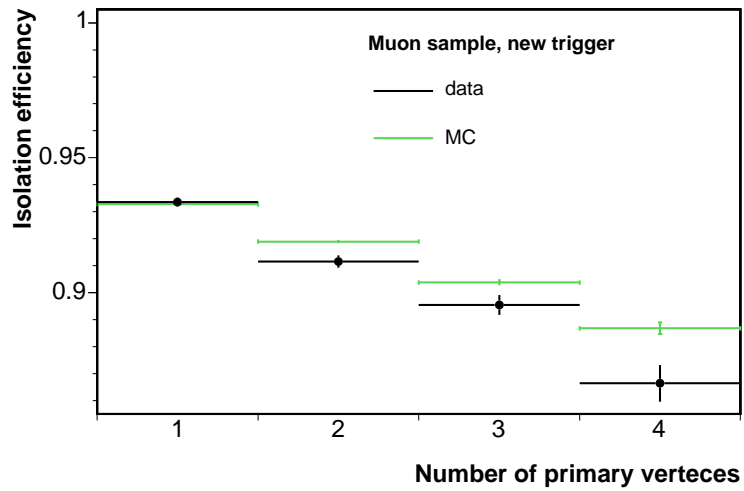
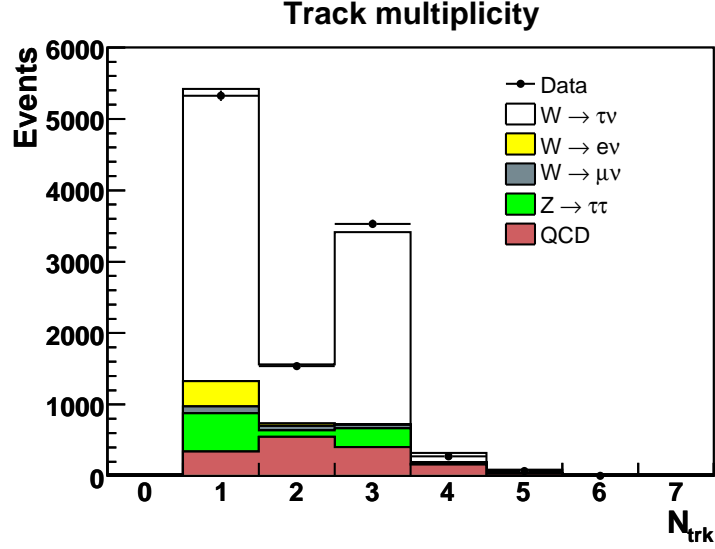
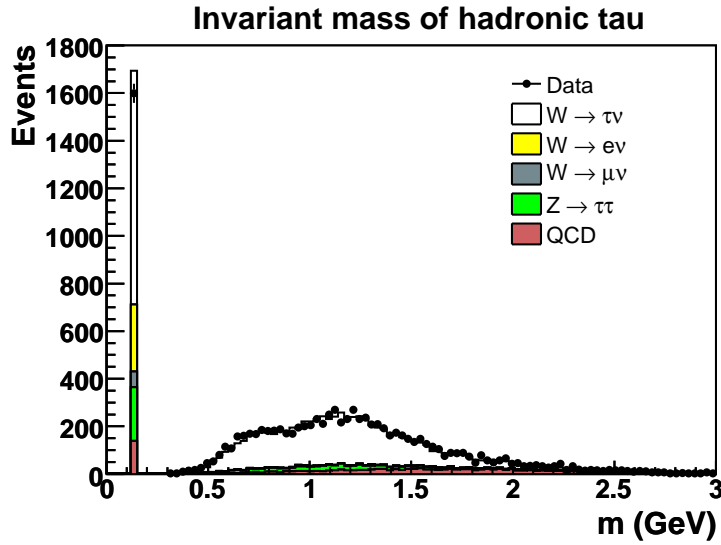
(a) Efficiency measured with $Z \rightarrow ee$ events, run > 209769(b) Efficiency measured with $Z \rightarrow \mu\mu$ events, run > 209769

Figure 6.5: Comparison of the efficiency of the $\sum p_{T, trk}^{iso} < 2 \text{ GeV}$, $\sum E_{T, \pi^0}^{iso} < 1 \text{ GeV}$ cuts in data and MC using $Z \rightarrow ee, \mu\mu$ events (1.8 fb^{-1} sample).

the $W \rightarrow \tau\mu$ production, we only need to determine the relative contributions from the major processes that contribute to the selected events. The relative contributions of the MC events from EW processes are fixed to the ratios of their cross sections. The number of residual $jet \rightarrow \tau$ fakes is obtained by performing a fraction fit of the track multiplicity distribution with templates from MC and a JET20 sample. The fitted distribution is shown in Figure 6.6.



(a) Fitted track multiplicity distribution for tau candidates from the $\tau + \cancel{E}_T$ sample



(b) Mass of the hadronic decay products (1,3-prong)

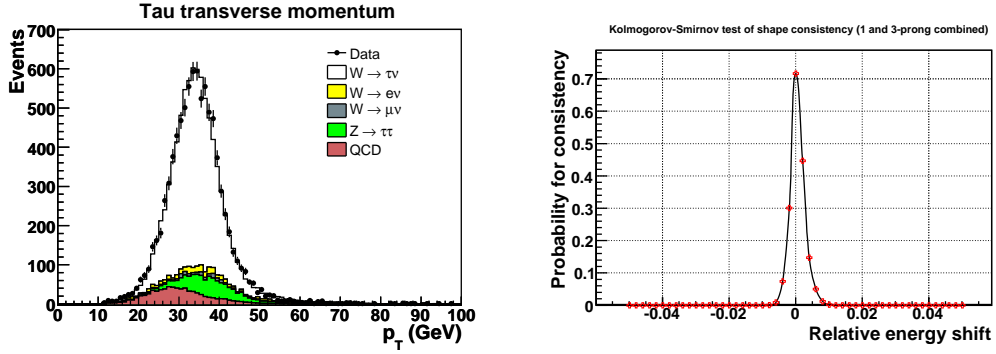
Figure 6.6: Track multiplicity and $m(trks + \pi^0$'s) for tau candidates. Contributions from $W \rightarrow \tau\nu$ and various backgrounds are included as shown in the Legend.

Figure 6.6 shows the tau mass distributions for 1- and 3-prong taus with normalization. The mass cut ($m < 1.8 \text{ GeV}$) efficiency for 1-prongs is 0.952 ± 0.003 for data and 0.969 ± 0.003 in the MC. From here we determine $\epsilon_{data}^{m \text{ cut}} / \epsilon_{MC}^{m \text{ cut}} = 0.982 \pm 0.05$. To account for deficiencies in the reconstructed mass in the data we decided to relax the mass in the 3-prong samples to

2.2 GeV, and find efficiency of 0.944 ± 0.004 for data and 0.978 ± 0.003 in the MC, resulting in a data/MC scale factor of $\epsilon_{data}^{m cut} / \epsilon_{MC}^{m cut} = 0.965 \pm 0.005$. Due to the discrepancy in the mass distributions in the high-mass region for 3-prongs we increase the uncertainty on the mass cut efficiency to 2%.

Based on the data/MC comparisons we assign a 3% systematic uncertainty on the selection of hadronically decaying taus. When applicable, the MC events are scaled using the derived scale factors.

The determination of the tau energy scale is not straightforward. The presence of neutrinos in tau decays prevent us from making reconstructing narrow resonances like it is done for electrons and muons. Here we use a comparison of the data and MC p_T distributions of reconstructed taus in $W \rightarrow \tau\nu$ decays and look for indication of relative data/MC energy shifts. In previous work (27) corrections of the order of 1% were derived to be applied to the data. The same procedure is used and confirms, that these corrections are still valid for the new sample as shown in Figure 6.7.



(a) p_T spectrum of the decay products in hadronic tau decays.

(b) p_T spectrum of the decay products in hadronic tau decays.

Figure 6.7: Distributions of tau p_T in data and MC after correcting data for the observed shifts (left), and the resulting KS test (right).

The p_T distributions and the corresponding KS test results after applying the previously derived corrections are shown in 6.7.

6.1.4 Missing Transverse Energy (\cancel{E}_T)

The presence of \cancel{E}_T in an event (apart from the instrumental part) is an indication of the presence of “invisible” particle(s). In the studies topological states we have three or four neutrinos. Therefore, \cancel{E}_T represents the transverse component of the sum of the neutrinos momenta (and it is more appropriate to call it missing transverse momentum). Most of the events have taus that are almost back-to-back in the transverse plane and the neutrino momenta are balanced to a large degree. As a result the signal signature is not always characterized by a large \cancel{E}_T .

In order to improve efficiency and purity \cancel{E}_T is used both in the event selection cuts and signal extraction. The “raw” \cancel{E}_T in the event is calculated for the z -position of the primary vertex (if no vertex is present, the z -position of the leptons is used). We apply three different corrections to the “raw” \cancel{E}_T , the standard joint physics recommended corrections for muons and jets and an additional correction based off taus. We apply muon corrections when a track passes the muon ID requirements, by replacing the transverse energy in the hit tower(s) by the track p_T for purposes of \cancel{E}_T calculation. Calorimeter response to jets is taken into account by applying the jet energy corrections up to (and including) Level 5 to all jets with $E_T^{raw} > 10$ GeV in the region $|\eta| < 2.4$ (if they are not identified as e , μ , or τ).

For the $\mu\tau$ channel we apply an additional correction to \cancel{E}_T , the tau calorimeter cluster E_T is replaced by the calculated tau p_T . Studies have shown this improves the agreement obtained as indicated by figure 6.8.

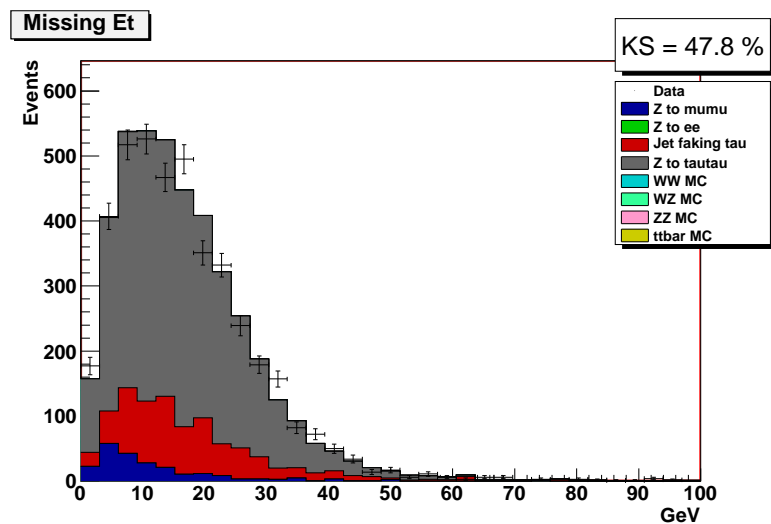
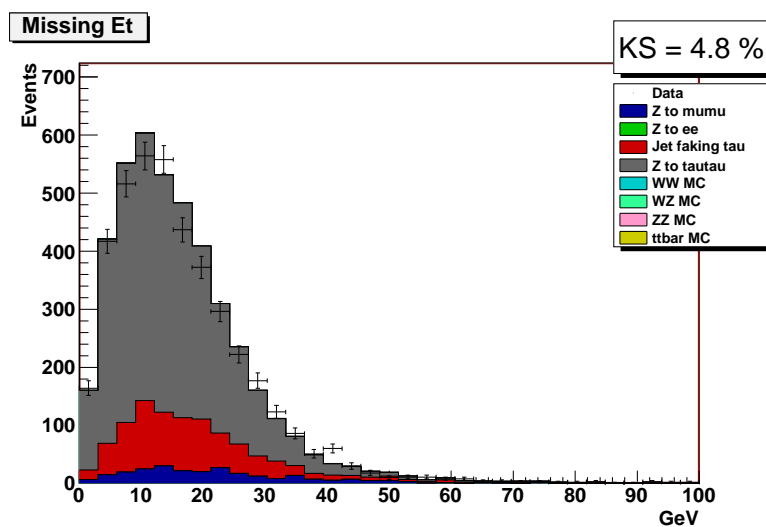
(a) \cancel{E}_T spectrum in $\mu\tau$ channel with correction(b) \cancel{E}_T spectrum in $\mu\tau$ channel without correction

Figure 6.8: Distributions of \cancel{E}_T in $\mu\tau$ channel with tau correction (left) and without tau correction (right)

Chapter 7

Event Selection and Background Estimates

7.1 Event Cuts

Apart from the irreducible background from $Z/\gamma^* \rightarrow \tau\tau$ the major other backgrounds in this analysis are $Z/\gamma^* \rightarrow ll$, $W \rightarrow l\nu + jet(s)$ ($l = e, \mu$), and ‘‘QCD’’ ($p\bar{p} \rightarrow jets$). The event cuts are designed as a compromise between effective suppression of the major reducible backgrounds and maintaining sufficient signal efficiency. Other backgrounds, such as $t\bar{t}$ and di-boson events are taken into account in the analysis (and are also suppressed by some of the cuts), but due to their small contribution played limited role in designing the cuts.

7.1.1 General Requirements

The two leptons must come from the same interaction: $|z_0^{(1)} - z_0^{(2)}| < 5 \text{ cm}$. To increase signal detection efficiency we do not require a reconstructed primary vertex in the event. The $p\bar{p}$ interaction point $|z_0^{int}|$ is taken as the average z_0 's of the two leptons: $z_0^{int} = 0.5 \times (z_0^{(1)} + z_0^{(2)})$, and must be in the luminous region: $|z_0^{int}| < 60 \text{ cm}$. The electron and muon are required to have opposite charge: $Q^{(1)}Q^{(2)} = -1$.

7.1.2 ζ cut

The ‘‘ ζ cut’’ is an attempt to discriminate events with \cancel{E}_T that are not consistent with a particle decaying to two taus. It is targeted at di-boson, $W \rightarrow l\nu + jet(s)$, but also helps to suppress QCD, and $t\bar{t}$ events.

We define a bisection axis $\vec{\zeta}$ in the transverse plane for the directions of the visible tau decay products (in this case the electron and muon) -see Figure 7.1. The transverse momentum of ϕ (or any other particle decaying to two taus) is

$$\vec{P}_T^\phi = \vec{P}_T^{vis}(\tau_1) + \vec{P}_T^{vis}(\tau_2) + \vec{\cancel{E}}_T,$$

where we assume that $\vec{\cancel{E}}_T$ is the sum of the transverse momenta of the neutrinos from tau decays. The transverse momentum of the tau visible products is

$$\vec{P}_T^{vis \tau} = \vec{P}_T^{vis}(\tau_1) + \vec{P}_T^{vis}(\tau_2).$$

The projections of \vec{P}_T^ϕ and $\vec{P}_T^{vis \tau}$ onto the defined $\vec{\zeta}$ axis are

$$P_\zeta^\phi = \vec{P}_T^\phi \cdot \vec{\zeta}$$

and

$$P_\zeta^{vis \tau} = \vec{P}_T^{vis \tau} \cdot \vec{\zeta},$$

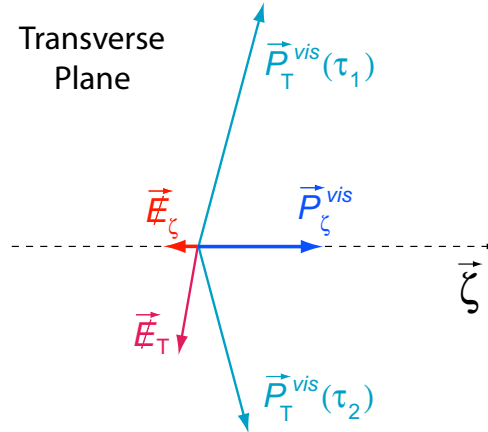


Figure 7.1: Illustration of the definition of parameters used in the ζ cut.

respectively.

Figure 7.2 shows the P_ζ vs P_ζ^{vis} distribution for $\phi \rightarrow \tau\tau$, and $W \rightarrow l\nu + jet(s)$ MC events. The distributions are plotted after applying the other event cuts. The graphical cut shown on these plots results in small efficiency loss and substantial background suppression.

The rationale behind this cut is simple: both the neutrinos and the visible decay products from tau decays go at small angles from the initial tau direction. Therefore, the sum of the neutrino's momenta should not go opposite to the direction of the sum of visible products. The defined acceptance region implicitly takes into account MET resolution. The cut placement is determined by inspecting the predicted distributions and minimizing the signal losses. Figure 7.2 shows the effect of the cut on signal (Higgs) and several of the backgrounds.

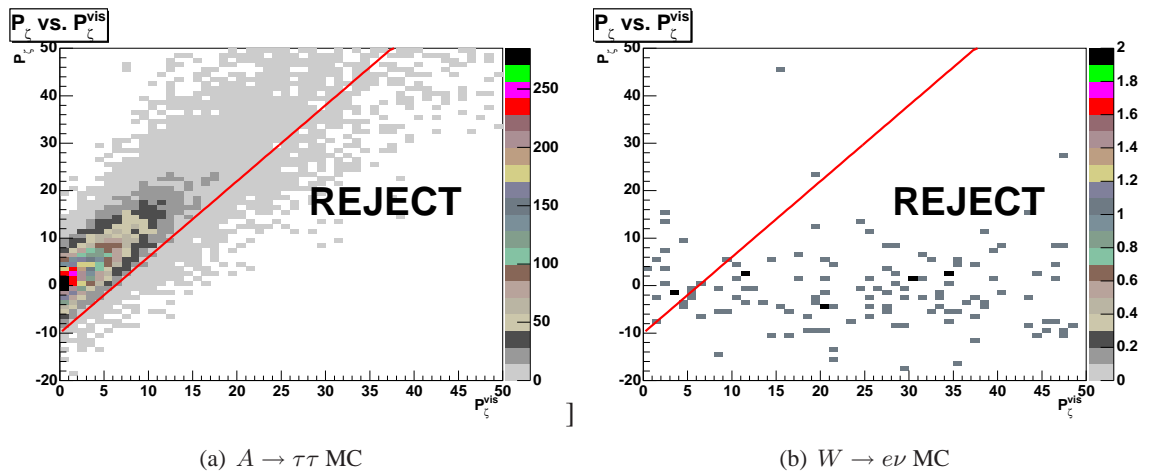


Figure 7.2: Effect of the ζ cut.

7.1.3 Suppression of QCD backgrounds.

Jets are suppressed to a significant degree by the lepton ID cuts and the isolation requirements. However, at low E_T their number is so large that event cuts are needed to clean up the sample.

For the $\tau_l\tau_{had}$ we define $H_T = |p_T^l| + |p_T^\tau| + \cancel{E}_T$. Previously we placed a uniform cut of $H_T > 50$ GeV. In this analysis we apply different cuts, based on track multiplicity of the tau candidates. 3-prong tau decays have larger contamination from misidentified jets and we raise the threshold to $H_T > 55$ GeV. For 1-prong tau decays in the $\tau_e\tau_{had}$ channel we keep the cut at 50 GeV. The jet contamination in 1-prong decays in the $\tau_\mu\tau_{had}$ is the smallest, and we use a cut of $H_T > 45$ GeV to recover some efficiency in the low-mass Higgs region. The cuts are placed based on the inspection of the distributions of same-sign events in the data.

For the $\tau_e\tau_\mu$ the jet backgrounds can be reduced significantly with sufficiently high lepton p_T . However, this leads to a loss in signal efficiency. As compromise require $|E_T^e| + |p_T^\mu| > 30$ GeV, that allows us to keep the jet backgrounds under control. Figure 7.3 shows the distributions for like-sign events in the data, and the lowest-mass Higgs boson ($m_A = 90$ GeV) considered in this search, and Higgs with mass $m_A = 200$ GeV. In addition for approximating the shape, like-sign events also give us an *approximate* estimate of the number of background events that will enter the sample. The cut value is chosen to cut out the bulk of the exponentially increasing background events.

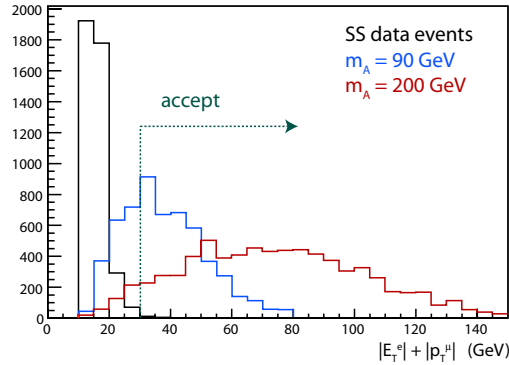


Figure 7.3: Effect of the $|E_T^e| + |p_T^\mu|$ cut on like-sign data events and Higgs signal ($m_A = 90, 200$ GeV). The normalization of the Higgs signal is arbitrary.

7.1.4 $Z \rightarrow ll$ Removal

In the $\tau_\mu\tau_{had}$ and $\tau_e\tau_{had}$ channel we apply a cut to reduce the background from $Z \rightarrow ll$ events. We veto events with 1-prong tau decays if the invariant mass of the tau track and the lepton is within 10 GeV of m_Z .

7.2 Backgrounds and estimation methods

7.2.1 $Z \rightarrow ll$

This group includes $Z \rightarrow \tau\tau$ decays to the same final states as the signal. Apart from di-tau mass (and related parameters) these events are practically indistinguishable from the signal. This is the largest expected background for this analysis. We do not make any attempt to suppress the Z background. Any differences in di-tau mass related parameters are used at the time of signal extraction/limit setting procedure. $Z \rightarrow ee$ and $Z \rightarrow \mu\mu$ also contribute some background events due to particle misidentification. These backgrounds are also estimated using MC samples from the Electroweak group. For the $Z \rightarrow ee$ and untagged $Z \rightarrow \tau\tau$ samples we merge run dependent MC corresponding to P0-13 with run independent MC, with each sample weighted according to the fraction of total luminosity represented by the appropriate run period. The $Z \rightarrow ee$ samples used are the zewk*d, zewkee, zewkeh, zewkej and zewkei datasets. The $Z \rightarrow \tau\tau$ samples used are the zewk*t datasets and for $Z \rightarrow \mu\mu$ we use the zewkdm dataset. The samples are normalized to the CDF measurement of the Z production cross section in $Z \rightarrow ee$ (lepton universality is assumed). The $Z \rightarrow \tau\tau$ decays in the tagged channel are handled separately as discussed later.

7.2.2 Di-boson, $W + \gamma$, and $t\bar{t}$

These are small backgrounds (due to small production cross sections). The final states contains the particles expected in our signal final state (in the $W + \gamma$ case there must be an unremoved photon conversion). These backgrounds are substantially suppressed by the “ ζ cut”. All these backgrounds are estimated using MC samples.

7.2.3 Backgrounds with Misidentified or Non-isolated e or μ in the $\tau_e\tau_\mu$ Detection Mode

The leptons in this group come either from a misidentified particle in a jet, or a real lepton contained in a jet. We do not separate these two sources and use a procedure based on the selecting events with non-isolated leptons to estimate the contamination in our final sample and predict the shapes in the distributions of interest.

We use the same p_T thresholds and isolation requirements for electrons and the muons that allows us to treat them in a symmetric way. For each lepton we define a sideband regions in terms of track isolation that is separated from the signal region ($I_{iso}^{trk} < 2$ GeV): $4 < I_{iso}^{trk} < 10$ GeV. The other lepton is required to be isolated. The area of each sideband is larger than the size of the signal region to increase the statistics of the selected events. The sum of the events in the two lepton sidebands are used to approximate the background shapes for events that are contained in the signal region. The sample is normalized to account for the different area in the sidebands. The distribution of track isolation is not guaranteed to be flat in signal

and sideband regions. This effect is handled using information from the like-sign events: we estimate the expected number of like-sign events using the sidebands and compare with the observed number of isolated like-sign $e\mu$ pairs (after subtracting contributions from the other background sources). The ratio is used as an additional scale factor f_{sb} for the background in the opposite-sign sample. The distributions in the sidebands of like-sign electrons and muons is shown in Figure 7.4. From these distributions we obtain $f_{sb} = 1.15 \pm 0.20$.

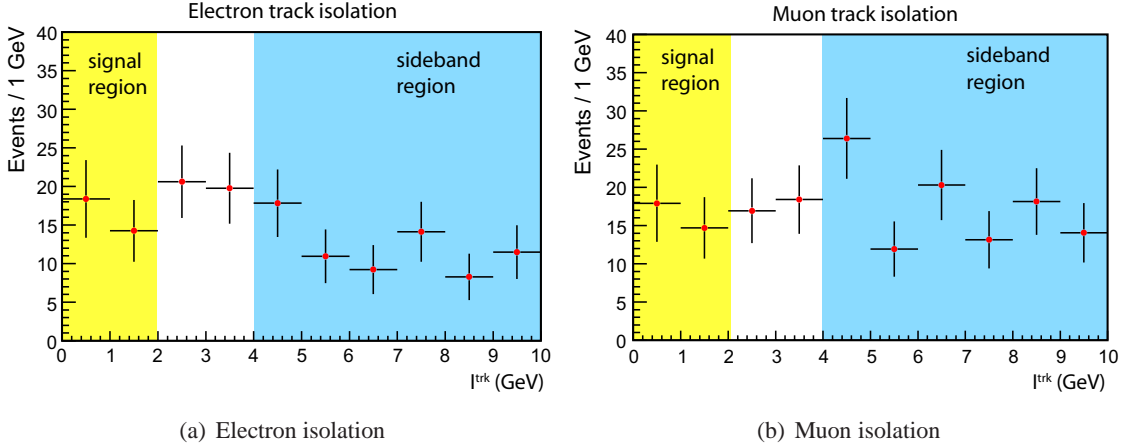


Figure 7.4: Track isolation for electrons and muons in same-sign events passing all other selection criteria.

This procedure fully accounts for multi-jet backgrounds. In this case both leptons originate from jets. Another source we have to consider is W +jets, where only one of the leptons is misidentified, and the other one is from $W \rightarrow l\nu$. For this case the above procedure will account only for half of the events from this source (each sideband should contain the respective events with one misidentified lepton, however when taking the average of the two we allow half of these W + jets events). W +jets events are effectively suppressed by the ζ -cut and their contribution to the final sample is negligible. To confirm this hypothesis we use inclusive W MC samples. We do not expect the MC to reliably predict the absolute number of background events and instead of scaling the MC samples to the data luminosity we normalize to the excess of events in the data in a control region.

7.2.4 Backgrounds from Misidentified $jet \rightarrow \tau_{had}$ in the $\tau_l \tau_{had}$ Detection Modes

There are three quite different processes that contribute to this group:

- $W \rightarrow l\nu + jet(s)$: one of the jets fakes a hadronic tau
- $\gamma + jet$: the photon undergoes conversion with onesoft/undetected leg, resulting in reconstruction of an isolated electron; the jet fakes a hadronic tau
- $p\bar{p} \rightarrow n jets$: one jet fakes a tau, another one fakes an e/μ

In this analysis we use an updated data based fake rate method for $jet \rightarrow \tau_{had}$ misidentification. (54)

The fake rate method assumes that the jets from the above sources have similar properties and that differences are covered by assigning systematic uncertainties ($\sim 15\%$). The challenge of applying this method to events selected with the “lepton+track” triggers is that the tau candidates are already quite isolated (in terms of tracks). Consequently, when applying fake rates the substantial “contamination” with real taus has to be accounted for which a method has been developed. The following is an outline of the method.

Let us start with a simplified case, and consider an initial sample passing loose tau cuts, and a final sample produced after applying the tight cuts. The number of real taus and $jet \rightarrow \tau$ fakes that survive this transition depend on the efficiency and fake rate (calculated with respect to the loose objects).

Let \hat{N} be the number of tau candidates passing the loose tau cuts, and denote the number of candidates passing the tight tau cuts by N . There are three sources that contribute to the observed events: real taus, leptons ($l = e, \mu$), and “jets”. This is reflected in the following set of equations

$$\begin{aligned}\hat{N} &= \hat{N}^\tau + \hat{N}^{jet} + \hat{N}^l \\ N &= N^\tau + N^{jet} + N^l \\ N^\tau &= \epsilon \hat{N}^\tau \\ N^{jet} &= f \hat{N}^{jet},\end{aligned}$$

where the last two expressions are the definitions of relative efficiency and fake rate.

Then it is easy to show that the jet background can be written as

$$N^{jet} = \frac{f}{\epsilon - f} [\epsilon \hat{N} - N] - C_l,$$

where C_l is a correction for e, μ contributions (which is small for the considered processes). It has the form

$$C_l = \frac{f}{\epsilon - f} [\epsilon \hat{N}^l - N^l],$$

where the leptons passing as loose and tight taus can be obtained from MC simulation.

If we take into account that efficiency and fake rate are actually functions of the parametrization variables (whatever they might be) and write the equations for infinitesimally small regions in parameter space, we get the same expressions for the fake tau density in terms of the event densities \hat{n} and n (instead of number of events)

$$n^{jet}(\Omega) = \frac{f(\Omega)}{\epsilon(\Omega) - f(\Omega)} [\epsilon(\Omega) \hat{n}(\Omega) - n(\Omega)] - c_l,$$

where Ω denotes a point in the efficiency/fake rate parametrization space. The densities $\hat{n}(\Omega)$ and $n(\Omega)$ are given by

$$\hat{n}(\Omega) = \sum_i^{\hat{N}} \delta(\Omega - \Omega_i)$$

$$n(\Omega) = \sum_i^N \delta(\Omega - \Omega_i).$$

To obtain the number of $jet \rightarrow \tau$ fakes in the final sample we substitute the above densities in the expression for $n^{jet}(\Omega)$ and integrate over the parameter space. The QCD estimation reduces to a sum over all loose taus which enter with weight

$$w_i^{\overline{ID}} = \frac{f(\Omega_i)\epsilon(\Omega_i)}{\epsilon(\Omega_i) - f(\Omega_i)}$$

if the candidate did not pass tight tau ID cuts, and

$$w_i^{ID} = \frac{f(\Omega_i)(\epsilon(\Omega_i) - 1)}{\epsilon(\Omega_i) - f(\Omega_i)}$$

if it did. It is straight forward to apply the ‘‘lepton correction’’.

Using these weights we can obtain the distributions for various event variables.

We choose to parameterize the the fake rates and efficiencies in terms of track multiplicity, sum of the tau cluster E_T and calorimeter isolation E_T , and η_{det} of the tau candidate. The fake rates are obtained from jet samples.

As can be seen, the agreement between the predicted and observed tau fakes is quite good. One can argue that the observed fakes in the W +jets control region are closer to the upper limit of our prediction. This is not surprising, since the fake rates reflect the quark/gluon jet composition in multi-jet events. We can account for this small deviation by using W +jets MC events, normalized to account for the observed difference in the control region. Using this normalization we can obtain the contributions to the signal region. This procedure allows us to bring the tau fakes estimated to the level of the central value of the expectation. These additional contributions are included in the table with the summary of the observed backgrounds.

In order to further improve the background modeling by limiting statistical affects we apply a simple histogram smoothing algorithm to this background.

7.2.5 Methods for Modeling the $Z \rightarrow \tau\tau$ Background in the b Tagged Channel

In order to avoid issues regarding inaccuracies of b tag modeling in MC we employ a data-MC hybrid method to estimate $Z \rightarrow \tau\tau$ backgrounds in the tagged channels

We aim to select data events similar to our targeted background by selecting for $Z \rightarrow \mu\mu$ events in data, we then proceed to replace the muons in the event with τ 's from $Z \rightarrow \tau\tau$ MC events with the aim of producing a $Z \rightarrow \tau\tau$ event with the jets derived from data rather than MC.

To do so we begin by locating $Z \rightarrow \mu\mu$ candidates and then matching the candidate muons against τ 's from MC. To determine the candidate distance we use the following metric

$$metric = \sqrt{(\Delta P_t/5)^2 + (\Delta\phi)^2 + (\Delta\eta)^2 + (\Delta Z/40)^2}$$

source	untagged	tagged
$Z \rightarrow \tau\tau$	MC	data-MC hybrid
$Z \rightarrow ee$	MC	MC
$Z \rightarrow \mu\mu$	MC	MC
$t\bar{t}$	MC	MC
$jet \rightarrow \tau$ fakes	data (jet fakes)	data (jet fakes)
lepton fakes	data (sideband)	data (sideband)
$WW \rightarrow ll$	MC	MC
$WZ \rightarrow ll$	MC	MC
$ZZ \rightarrow ll$	MC	MC

Table 7.1: Summary of backgrounds and modeling methods

where all of the values are calculated between the generator level τ and the detector information from the μ . We then select the “closest” match for each candidate and use that τ to replace the μ from the data event, recalculating all the necessary event quantities such as \cancel{E}_T, H_t etc..

We then scale the resultant background based on the assumption that the pretag background is accurately modeled by the MC. So we normalize the pretag data-MC hybrid to the level of the pretag MC.

Table 7.1 summarizes all of the backgrounds and how we model them.

7.3 Signal Selection Efficiency

The Higgs signal selection efficiency for the defined cuts is shown in Figure 7.5 for the three detection modes. The efficiency is defined with respect to Higgs $\rightarrow \tau\tau$ production, where both taus can decay in any mode.

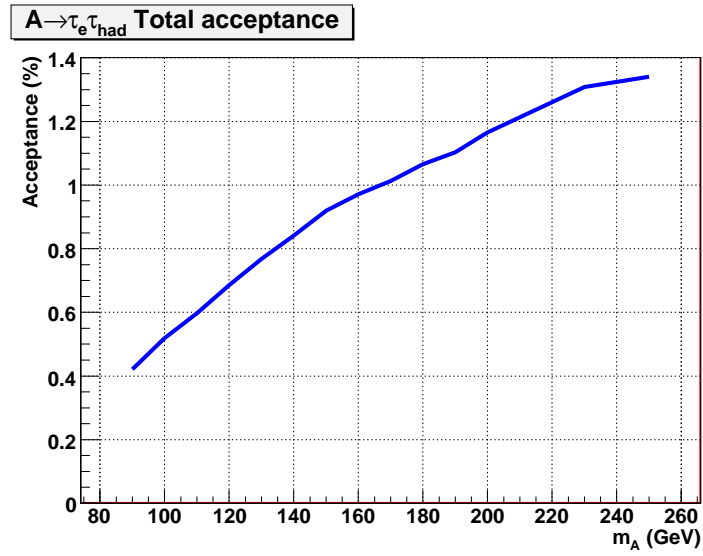
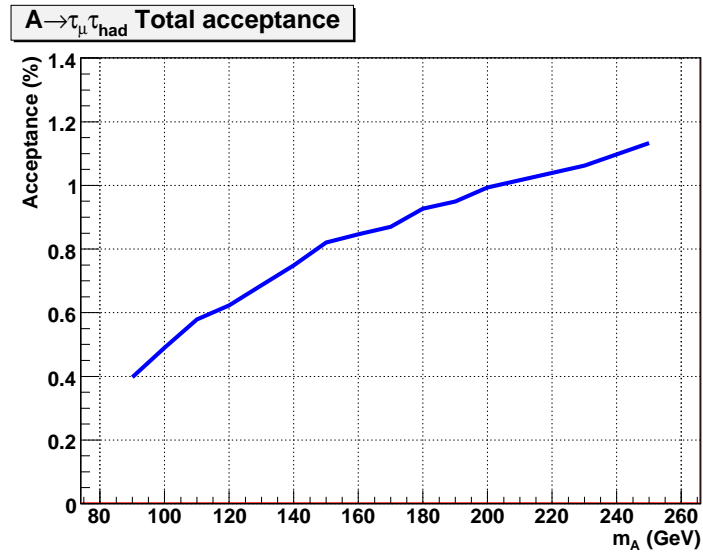
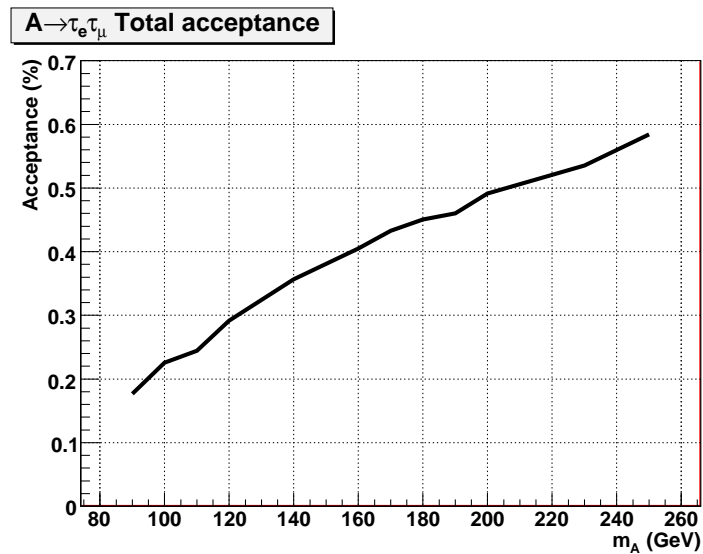
(a) $\tau_e \tau_{had}$ (b) $\tau_\mu \tau_{had}$ (c) $\tau_e \tau_\mu$

Figure 7.5: Signal selection efficiencies for the three detection modes as a function of Higgs mass (m_A).

Chapter 8

Results**8.1 Observed Results**

The number of observed events and the expected contributions from the considered background sources for the untagged channel are summarized in Table 8.1 and 8.2. Similarly, the tagged channel is summarized in Table 8.1 and 8.3. The errors quoted in the tables above are statistical only. The systematic errors are applied in the fits per source of the uncertainty and takes into account the correlation between the backgrounds.

source	untagged events	tagged events
$Z \rightarrow \tau\tau$	1746.96 ± 16.9	21.26 ± 4.1
$Z \rightarrow ee$	3.28 ± 1.2	0 ± 0
$Z \rightarrow \mu\mu$	92.7 ± 2.7	1.86 ± 1.1
$W/Z\gamma$, di-bosons	24.2 ± 0.21	0.236 ± 0.052
$t\bar{t}$	12.1 ± 0.3	11.74 ± 0.18
fake/non-ISO	126.5 ± 6.6	1.92 ± 0
Sum BG	2005.8 ± 19.5	37.0 ± 4.25
DATA	1903	22

Table 8.1: Predicted backgrounds and observed events in the $\tau_e\tau_\mu$ untagged and tagged channel after applying all selection cuts. The quoted errors are statistical only.

CDF Run II Preliminary $5.9 fb^{-1}$

source	$\tau_e\tau_{had}$ no-b	$\tau_\mu\tau_{had}$ no-b
$Z \rightarrow \tau\tau$	2851.58 ± 24.9	3238.94 ± 24.3
$Z \rightarrow ll$	96.49 ± 6.0	225.9 ± 6.9
di-boson events	5.06 ± 0.3	5.12 ± 0.15
$t\bar{t}$	2.97 ± 0.3	3.03 ± 0.21
total $jet \rightarrow \tau$ fakes	$1134.4 (\pm 15\% \text{ sys})$	$760.2 (\pm 15\% \text{ sys})$
Sum BG	4090.5 ± 172.1	4233.3 ± 116.8
DATA	4036	4175

Table 8.2: Predicted backgrounds and observed events in the $\tau_e\tau_{had}$ and $\tau_\mu\tau_{had}$ untagged channels after applying all selection cuts. The quoted errors are statistical only.

CDF Run II Preliminary 5.9 fb^{-1}

source	$\tau_e\tau_{had}$ btag	$\tau_\mu\tau_{had}$ btag
$Z \rightarrow \tau\tau$	13.75 ± 1.81	14.12 ± 2.97
$Z \rightarrow ll$	0.08 ± 1.71	0 ± 0
di-boson events	0.079 ± 0.071	0.082 ± 0.067
$t\bar{t}$	2.75 ± 0.075	2.86 ± 0.078
total $jet \rightarrow \tau$ fakes	5.78 ± 0.60	7.37 ± 0.96
Sum BG	22.4 ± 2.56	24.4 ± 3.12
DATA	23	8

Table 8.3: Predicted backgrounds and observed events in the $\tau_e\tau_{had}$ and $\tau_\mu\tau_{had}$ tagged channels after applying all selection cuts. The quoted errors are statistical only.

The following plots show comparisons of various distributions of the predicted standard model processes and the observed events in the untagged and tagged channel. In the plots the gray background corresponds to the $Z \rightarrow \tau\tau$, blue to $Z \rightarrow \mu\mu$ green to $Z \rightarrow ee$, red to either $jet \rightarrow \tau$ or sidebands depending on channel, teal and light blue to diboson and yellow to the $t\bar{t}$ background. Figures 8.1 and 8.2 refer to the untagged $\tau_e\tau_{had}$ channel, Figures 8.3 and 8.4 refer to the untagged $\tau_\mu\tau_{had}$ channel and Figures 8.5 and 8.6 refer to the $\tau_e\tau_\mu$ untagged channel, finally Figure 8.7 refers to all the untagged channels. Figure 8.8 refers to some basic kinematic properties of the tagged channels.

All of the following plots are made prior to the fitting process used in the extraction of the final limits and reflect a generally reasonable level of agreement between data and backgrounds.

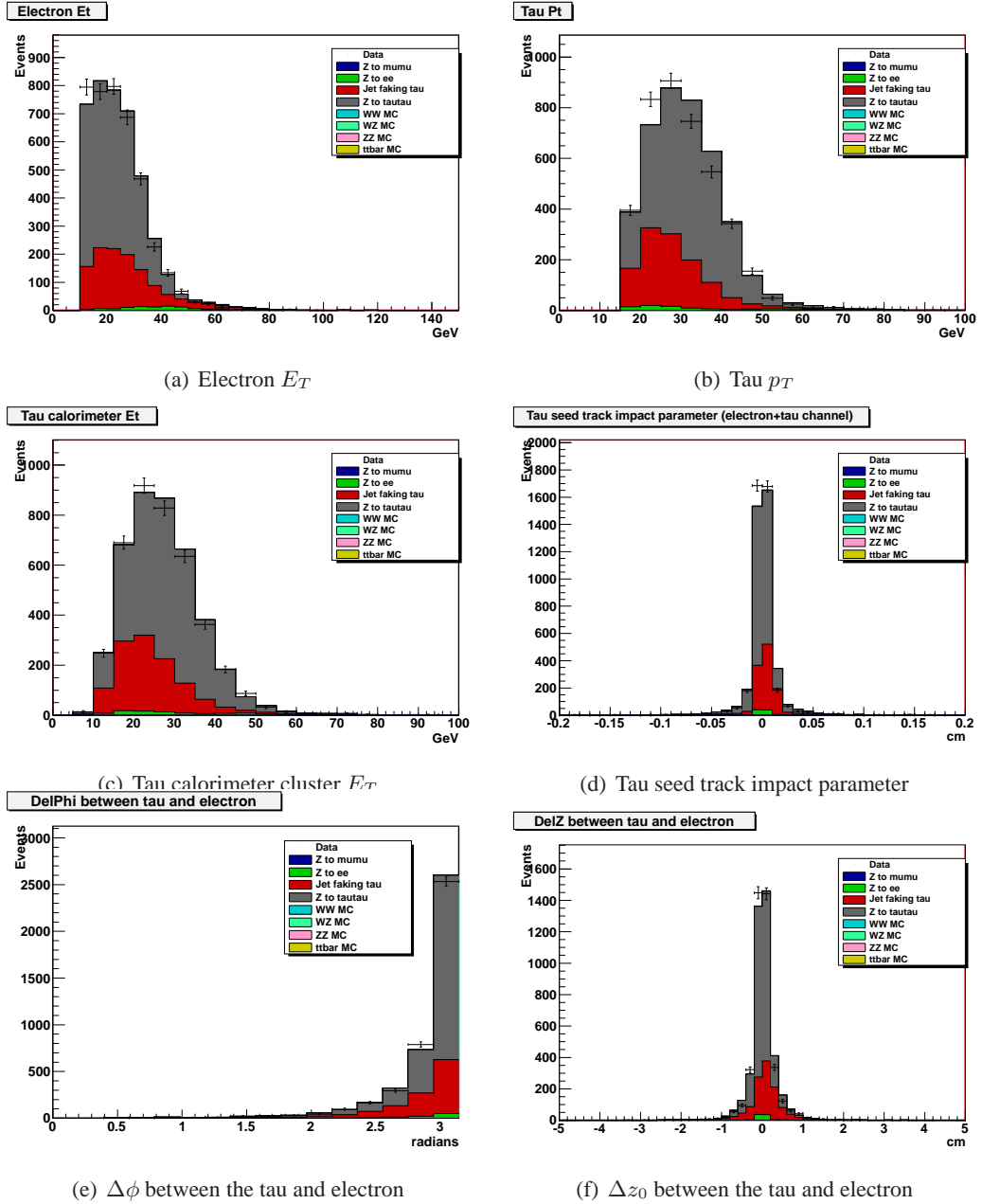


Figure 8.1: Distributions for $\tau_e Thad$ candidate events.

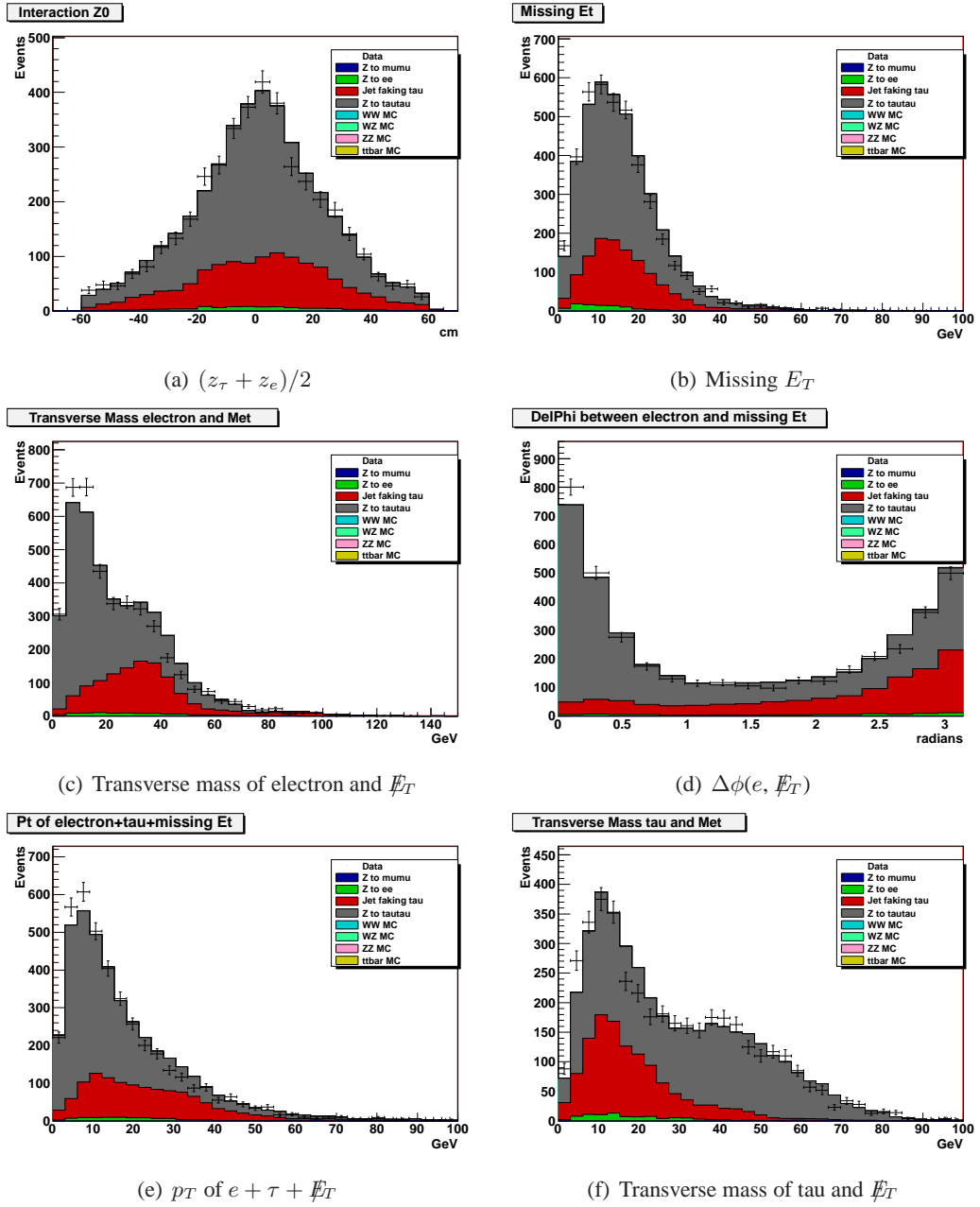


Figure 8.2: Distributions for $\tau_e Thad$ candidate events.

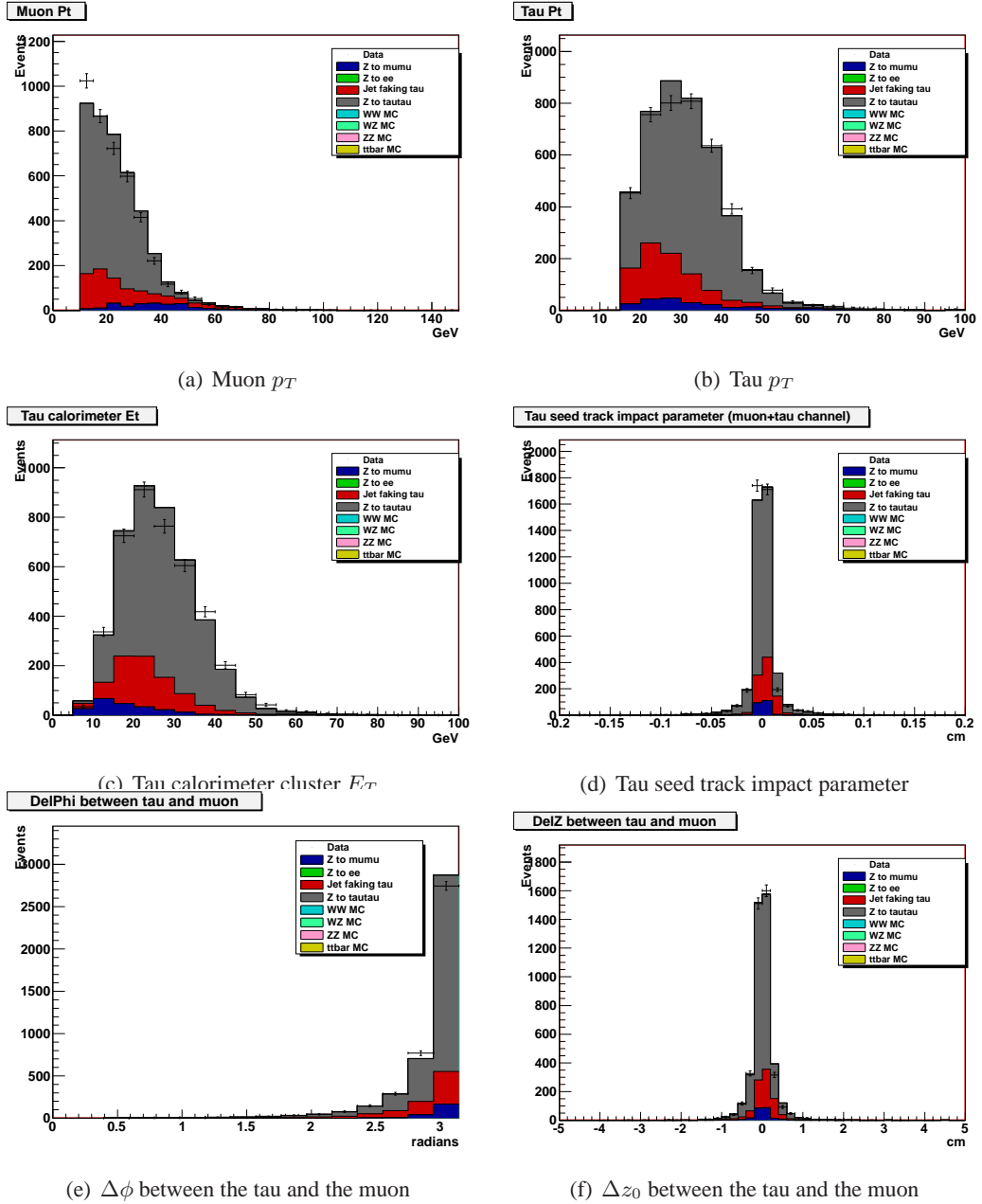


Figure 8.3: Distributions for $\tau_\mu Thad$ candidate events.

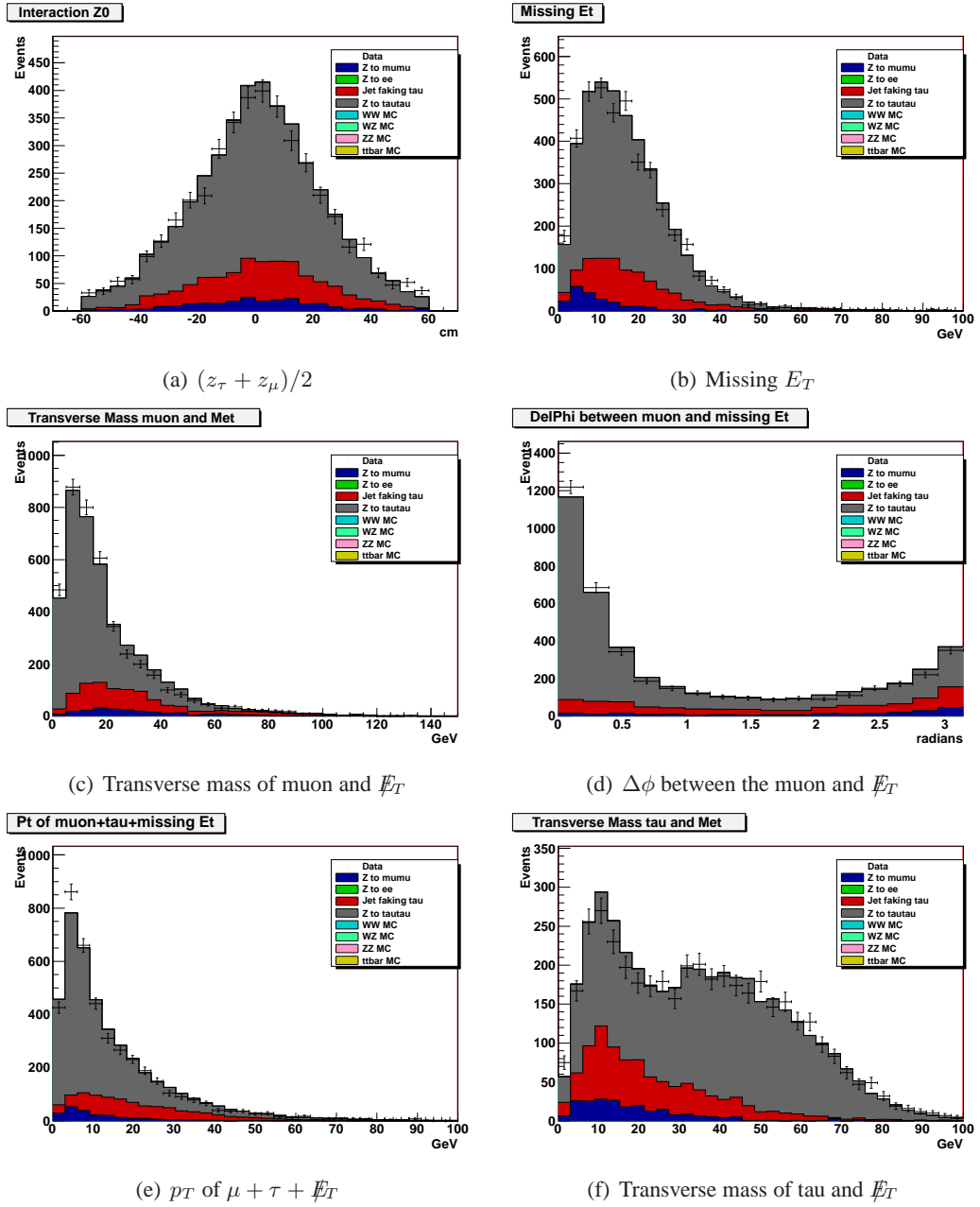


Figure 8.4: Distributions for $\tau_\mu\tau_{had}$ candidate events.

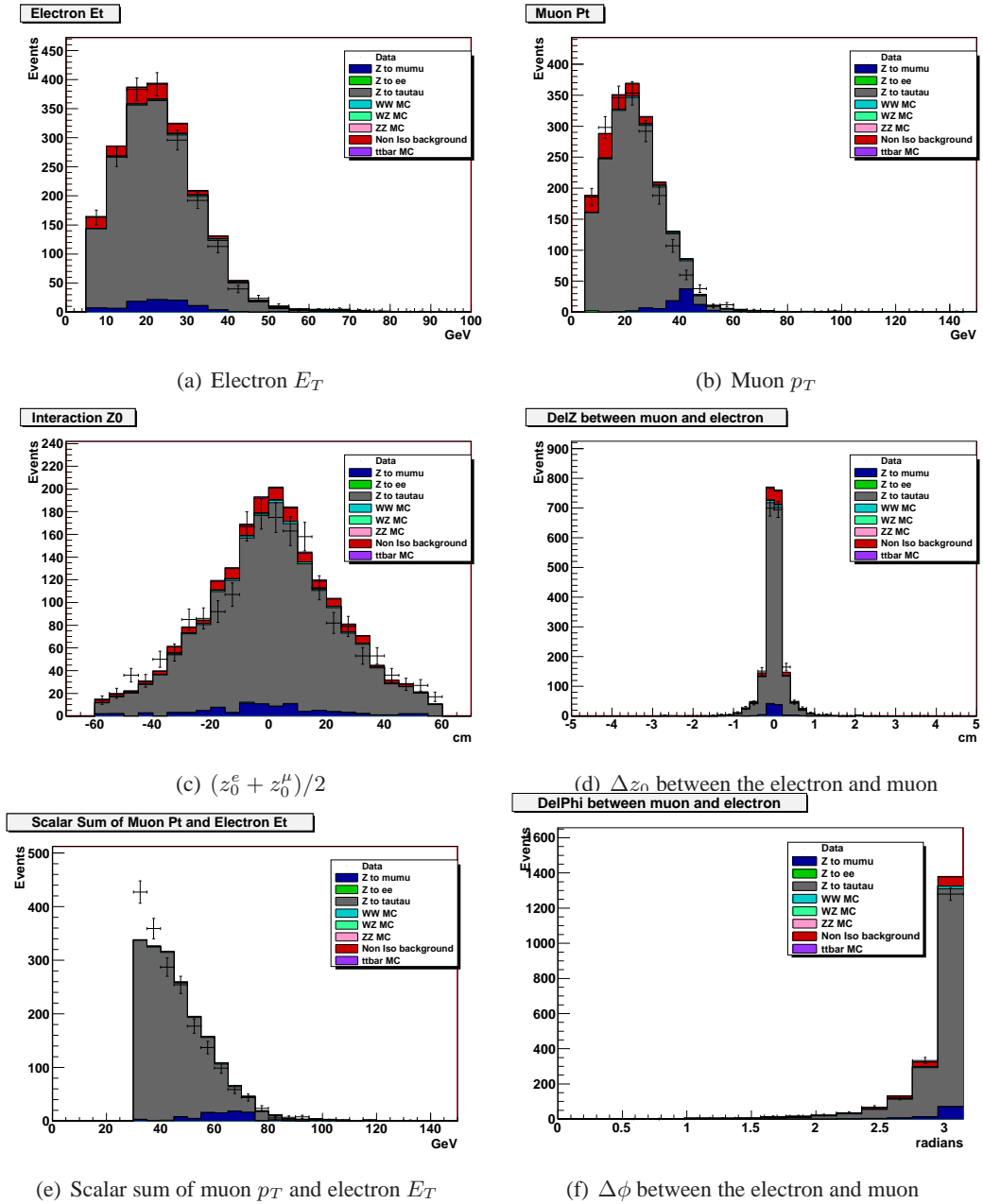


Figure 8.5: Distributions for $\tau_e \tau_\mu$ candidate events.

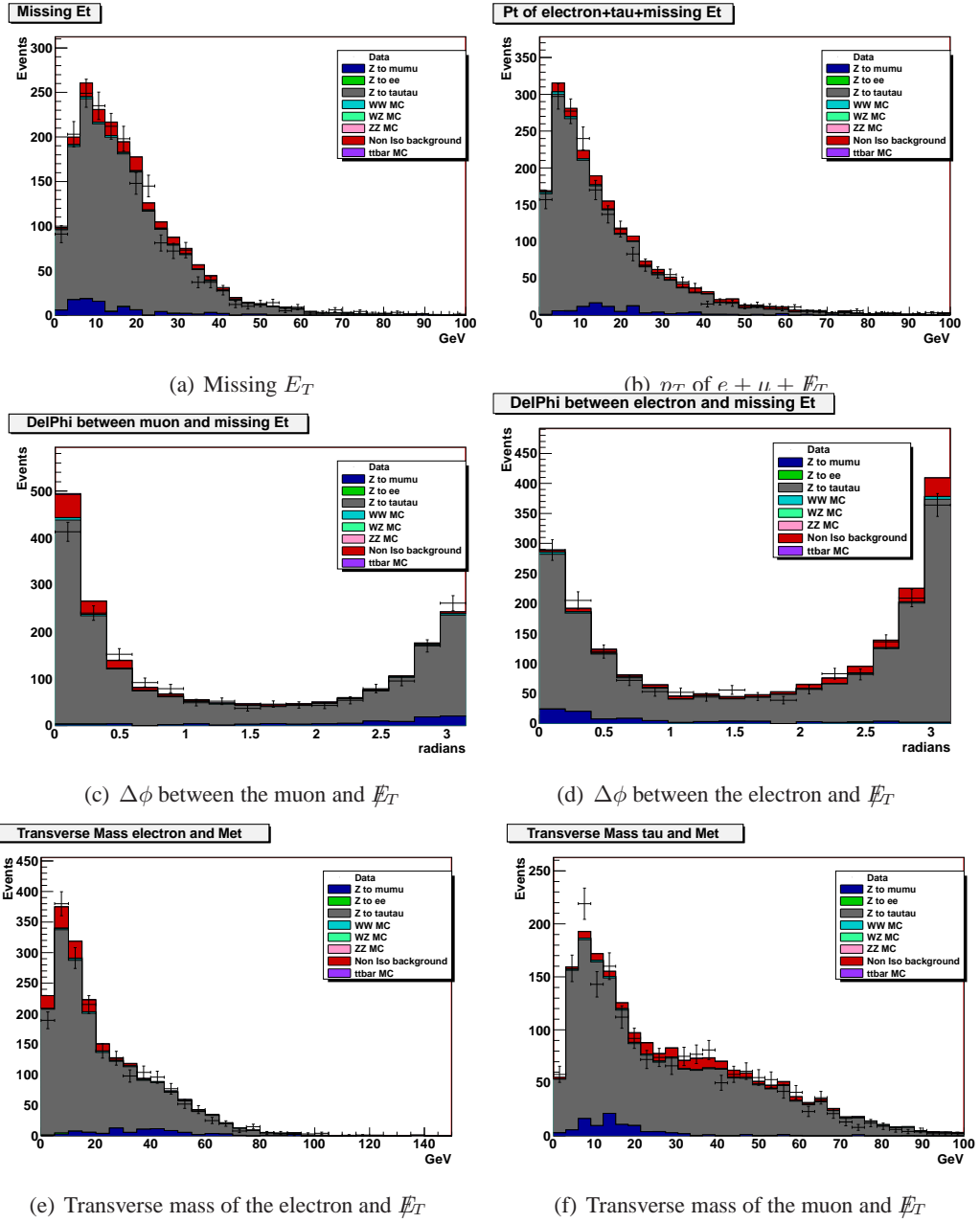


Figure 8.6: Distributions for $\tau_e \tau_\mu$ candidate events.

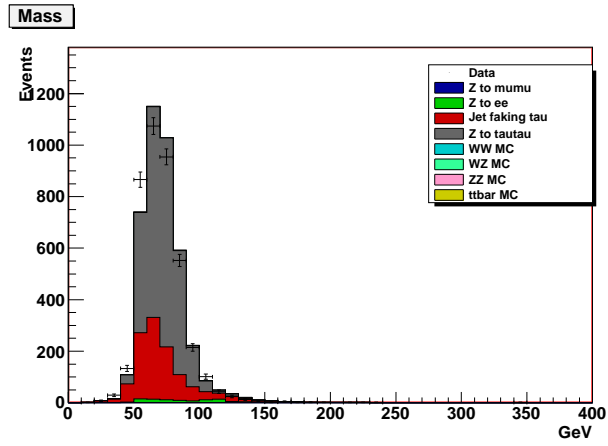
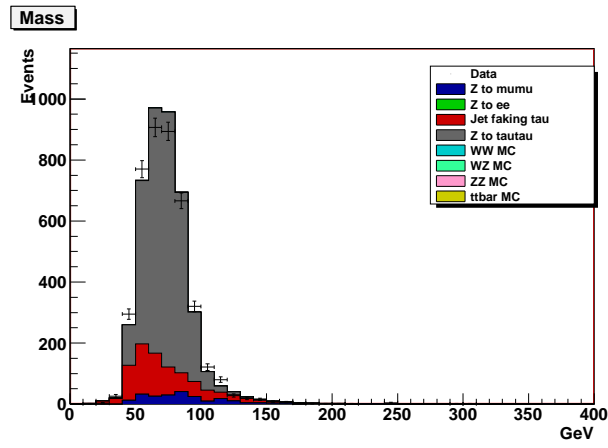
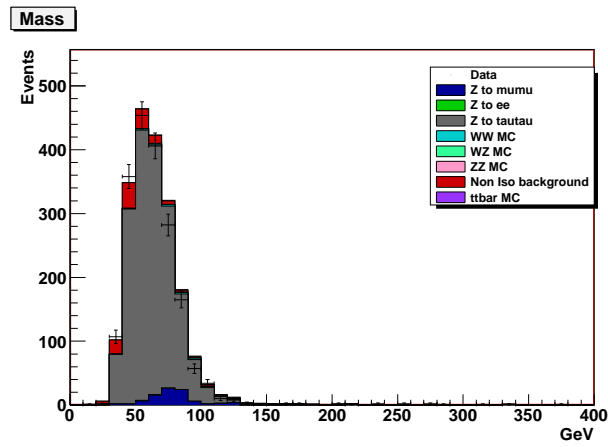
(a) $\tau_e \tau_{had}$ (b) $\tau_\mu \tau_{had}$ (c) $\tau_e \tau_\mu$

Figure 8.7: Distributions in the three channels used for signal extraction. All background normalizations are absolute.

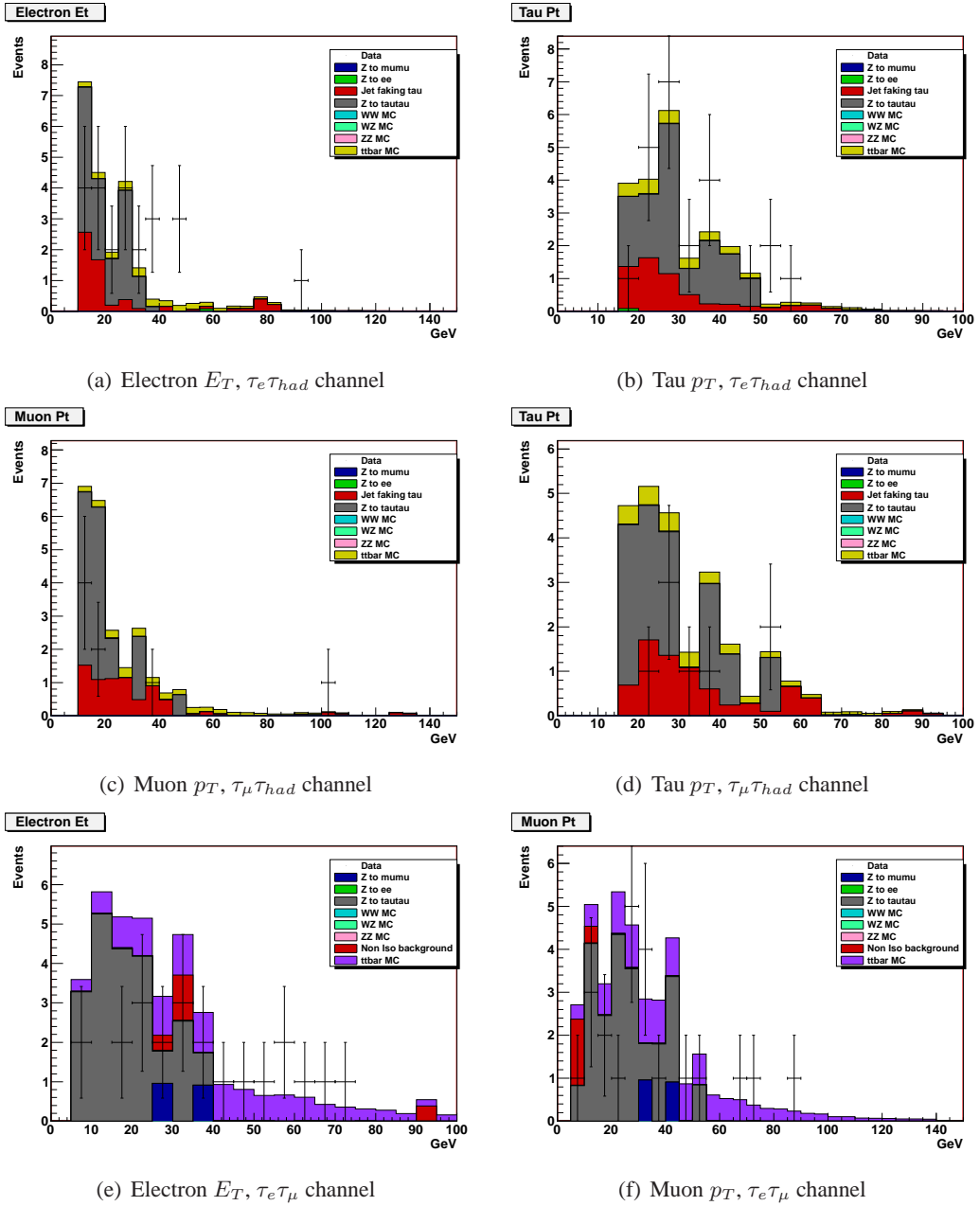


Figure 8.8: Distributions for b-tagged channels, first line is $\tau_e \tau_{had}$, second line is $\tau_\mu \tau_{had}$ and third line is $\tau_e \tau_\mu$.

8.2 Systematic Uncertainties

There are several sources of systematic uncertainties affecting the analysis:

- Trigger efficiency
- Particle ID
- Event cuts
- Background estimation
- PDF's used in MC simulation
- Luminosity

We define two types of systematic uncertainties. The first group includes rate uncertainties, that affect the expected number of signal or/and background events in the final sample, but do not lead to changes in the shape of the distributions of interest. The second group are shape uncertainties that affect the shape of the distribution used for signal extraction. Shape uncertainties can also be accompanied by changes in the number of selected events because of event-level cuts. Shape uncertainties are accounted for by producing sets of shifted templates that may contain different number of events compared to the nominal ones.

This separation is needed for the proper treatment of the systematic uncertainties in the signal extraction or setting of limits. For example, “event-cuts” uncertainties are not explicitly defined, but are accounted for in a natural way by the uncertainties affecting the parameters used to construct these cuts. In the following we present a short discussion of the considered uncertainty sources, and summarize the grouping and type of the uncertainties in Table 8.4.

8.2.1 Rate: ID efficiencies

We rely on MC simulation to predict the particle interaction in the detector and to estimate signal efficiency and most of the backgrounds. We account for possible differences between data and MC particle ID efficiencies through the introduction of scaling factors applied to MC. The uncertainties in determining these factors are assigned as systematic errors of particle reconstruction and ID efficiency. For muons and electrons we use the standard ID's (up to isolation) and assign the corresponding official uncertainties for intermediate- and high- p_T (E_T) muons (electrons). In addition we add in quadrature the uncertainty due to the track isolation cuts that are not part of the results in these references, which was found to be very small and independent of the lepton p_T . These are treated as rate uncertainties that do not affect the shapes. For the case of electrons and muons the uncertainty in the data/MC scale factor are different below and above 20 GeV. We use common systematic uncertainties obtained by weighting the fraction of electrons (or muons) in the low- and high- p_T regions. For a conservative estimate we use the fractions found in the $\tau_e\tau_\mu$ channel, which contain the larger portion of soft leptons. The

fraction of muons below (above) 20 GeV is 42% (58%). For electrons, the fractions below (above) 20 GeV are 43% (57%), similar to the electrons. We take 1% uncertainty for muons with $p_T > 20$ GeV, and 4% uncertainty for muons with $p_T < 20$ GeV, and assign overall 2.7% uncertainty to muon reconstruction and identification. For electrons, we use uncertainties of 0.6% (3.2%) for the case when electron E_T is above (below) 20 GeV. and assign uncertainty for electron identification of 2.4%.

8.2.2 Rate: Trigger Efficiencies

We assign 1% error for the muon triggers (covering all muon systems), and 0.3% for the electron trigger. The assigned uncertainty in the tau trigger rate is somewhat higher at 3% as determined in the efficiency study in Chapter 5. These uncertainties are applied to physics objects of the corresponding types in MC.

8.2.3 Rate: Sidebands

For the backgrounds from fake/non-isolated leptons in the $\tau_e\tau_\mu$ we add in quadrature the statistical error and the uncertainty in the sidebands scale factor. This results in a total relative uncertainty of 18% and is applied to the sideband backgrounds.

8.2.4 Rate: QCD fakes

For the uncertainties in the backgrounds in the $\tau_{e/\mu}\tau_{had}$ channels due to $jet \rightarrow \tau$ misidentification we assign a 30% systematic uncertainty based on the comparisons of the predicted and observed fake taus in the defined control regions. This is the half-difference between the estimates with the FR's obtained exclusively from the leading, and sub-leading jet in the event.

8.2.5 Rate: Tag efficiencies

For btags we rely on data for the $Z \rightarrow \tau\tau$ but otherwise use MC. Differences in MC/data response are included in a scale factor, we use the standard secVtx tag prescription assigning an uncertainty of ± 0.05 to the SF of 0.96.

8.2.6 Rate: Cross sections and branching fractions

The systematics related to background estimation from the MC samples are determined by the uncertainties in the cross-sections and branching fractions. We apply a 2.2% uncertainty to the $Z \rightarrow ll$ cross section and branching ratio. We assign a 13.4% uncertainty to the $t\bar{t}$ cross section. We assign a 10% uncertainty to the di-boson cross sections.

8.2.7 Rate: Signal PDFs

The systematic uncertainty in Higgs signal acceptance due to the lack of precise knowledge of the parton distribution functions (PDFs) is 5.7%, as estimated in a previous analysis (26). This is applied to the signal MC.

8.2.8 Rate: Luminosity

We use the standard luminosity uncertainty of 6% which is applied to all MC backgrounds.

8.2.9 Shape: Jet energy scale

Deficiencies in the simulation of calorimeter response to jets lead to MC/data differences in measured \cancel{E}_T . These are accounted for by the MC-specific jet energy corrections. To estimate the systematic uncertainties, we vary the jet corrections applied to the MC by one sigma to produce “shifted” templates for the signal extraction/limit setting. This is an example of a shape uncertainty accompanied by some change in the event rate coming through the application of the event cuts.

8.2.10 Shape: EM energy scale

Another source of shape uncertainty is the EM energy scale. We take 1% uncertainty in electron E_T and produce corresponding shifted templates. The same procedure is applied to the events in the channels with hadronically decaying taus. We ignore data/MC differences in the measurement of track p_T and do not assign a corresponding shape uncertainty resulting from muon p_T . These are applied to the appropriate physics objects in our background models.

8.2.11 Shape: Mistag rate

For the tag backgrounds another source of uncertainty comes from the mistag rate. We take a $\pm 1\sigma$ uncertainty in mistag rate and produce corresponding shifted templates.

8.3 Fitting Method

In this analysis we are looking for a Higgs signal on top of a very large background from $Z/\gamma^* \rightarrow \tau\tau$, plus other smaller backgrounds including fakes and diboson production. To distinguish the Higgs signal from this background we use the “visible mass” variable, m_{vis} , defined as a pseudo-four-vector formed from adding together the lepton and reconstructed tau four vectors to the transverse and total energy components of the \cancel{E}_T vector (setting its z component to zero). This variable is found to have slightly better signal-background discrimination than the transverse mass, for example. Example distributions for m_{vis} in the $\tau_l\tau_{had}$ channel is shown in Figure 8.9

Parameter	type	Error(%)	applies to:
e ID	rate	2.4	e in MC
muon reco+ID	rate	2.7	μ in MC
tau ID	rate	4.2	τ in MC
e trig	rate	0.3	e in MC
muon trig	rate	1.0	μ in MC
tau trig	rate	3.0	τ in MC
z-vertex cut	rate	0.5	all MC
fake/non-iso lepton bg in $\tau_e\tau_\mu$	rate	20.0	fake/non-iso bg
fake τ_{had} in $\tau_e\tau_{had}$	rate	30.0	fake tau bg
fake τ_{had} in $\tau_\mu\tau_{had}$	rate	30.0	fake tau bg
tight secVtx	rate	5.2	tags
$\sigma \times \mathcal{B}(Z \rightarrow ll)$	rate	2.2	Z MC
$Z \rightarrow ll$ backgrounds	rate	6	$\tau_e/\mu\tau_{had}$
$\sigma(t\bar{t})$	rate	13.4	$t\bar{t}$ MC
di-boson cross sections	rate	10	di-boson MC
PDFs (<i>Higgs</i>)	rate	5.7	signal
Luminosity	rate	6.0	all MC
JES	shape	$\pm 1\sigma$ (per jet)	all MC
EM scale	shape	± 1.0	e in MC
Tau p_T scale	shape	± 1.0	τ_{had} in MC
Mistag scale	shape	$\pm 1\sigma$ (per jet)	all MC

Table 8.4: Systematic uncertainties by source.

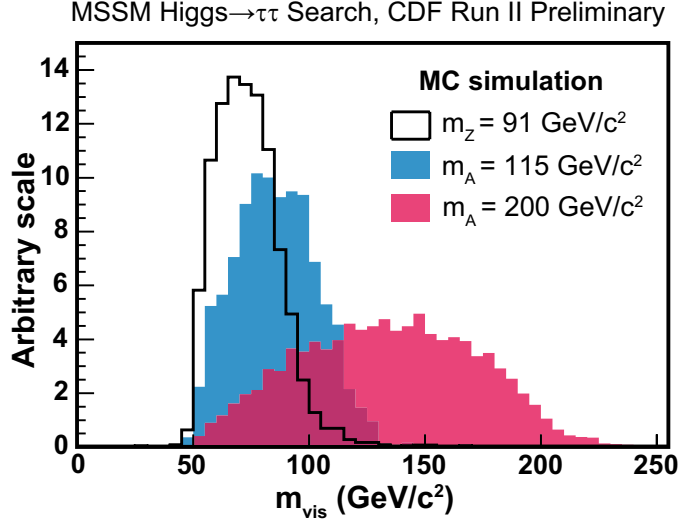


Figure 8.9: Visible mass distributions for Z and Higgs bosons (normalized to the same area).

We form a binned likelihood using the observed m_{vis} spectrum. If n_{ij} is the observed number of events in m_{vis} bin i , for channel j (where $j = 1$ corresponds to the $e\tau$ channel, $j = 2$ to $\mu\tau$, and $j = 3$ to $e\mu$, for the untagged channel and $j+3$ for the tagged channel), and μ_{ij} is the expected number of events in that bin, then the likelihood can be written

$$\mathcal{L} = \prod_{ij} \frac{\mu_{ij}^{n_{ij}} e^{-\mu_{ij}}}{n_{ij}!} \quad (8.1)$$

The expected number of events in a bin is the sum over all possible sources (indexed by k here), resulting from the product of the integrated luminosity L , the cross section times branching ratio σ_k for the source, and the efficiency ϵ_{ijk} in the bin:

$$\mu_{ij} = \sum_k L \sigma_k \epsilon_{ijk} \quad . \quad (8.2)$$

In principle if all the parameters except the signal cross section σ_h were known exactly, we could apply Bayes' Theorem to arrive at a posterior density $\mathcal{P}(\sigma_h)$ in the unknown variable:

$$\mathcal{P}(\sigma_h) = \frac{\mathcal{L}(\sigma_h)}{\int_0^{\sigma_{max}} \mathcal{L}(\sigma'_h) d\sigma'_h} \quad (8.3)$$

Here we assume a uniform prior density in the unknown signal cross section up to some maximum cutoff. This posterior density $\mathcal{P}(\sigma_h)$ can then be used to determine confidence intervals and estimate the true value of the signal rate.

8.4 Nuisance Parameters for Systematic Uncertainties

In practice not all of the parameters in the likelihood are known precisely, due to systematic uncertainties. For example the overall integrated luminosity L is uncertain at a level of 6%,

the $Z/\gamma^* \rightarrow \tau\tau$ cross section assumed is taken from the CDF measured value of 254.9 ± 5.7 pb (excluding the luminosity uncertainty), etc. We incorporate *all* systematic uncertainties as nuisance parameters in the likelihood. These include uncertainties listed in Table 8.4

- integrated luminosity,
- background cross sections,
- QCD (τ fake) rates,
- lepton and tau trigger/ID data/MC ratios,
- PDFs, and
- electron, tau and jet (\cancel{E}_T) energy scale.

All the parameters in the likelihood except the signal cross section are thus nuisance parameters, free to float within gaussian constraints corresponding to the uncertainty in that parameter. The overall likelihood can then be written

$$\mathcal{L} = \prod_{ij} \frac{\mu_{ij}^{n_{ij}} e^{-\mu_{ij}}}{n_{ij}!} \times G(L, L_0, \sigma_L) \times \dots \quad (8.4)$$

where the G functions are gaussians constraining the values of the imprecisely known parameters.

Template Morphing

The energy scale uncertainties are treated using a ‘‘template morphing’’ technique. Each background source bin efficiency ϵ_{ijk} is calculated for the nominal case, and for $\pm 1\text{-}\sigma$ shifts due to the uncertainty in the electron, tau, jet (\cancel{E}_T) scale, and mistag uncertainty. Then, in calculating the expected number of events in a bin, we allow a morphing parameter to control the admixture of the nominal and shifted bin efficiency. For example, if we let f^e represent the electron energy scale morphing parameter, the expected number of events in a given bin ijk can be written in terms of an efficiency

$$\epsilon_{ijk} = \epsilon_{ijk}^{nom} + f^e \left(\frac{\epsilon_{ijk}^+ - \epsilon_{ijk}^-}{2} \right) . \quad (8.5)$$

Thus the nominal value of the number of expected events corresponds to $f^e = 0$, and we include a unit gaussian constraint term on the value of f^e . The tau, jet energy scale and mistag uncertainties are handled in similar fashion simultaneously. The predicted number of events from a given source in a bin is never allowed to be negative as a result of the morphing.

Profile Likelihood

To obtain the posterior density in the signal rate $\mathcal{P}(\sigma_h)$ we need to eliminate the nuisance parameters. The pure Bayesian method would be to marginalize them by integrating the likelihood over them. We choose a different method, referred to as profiling, in which we maximize the likelihood with respect to all the nuisance parameters (using MINUIT) at each point in σ_h . This choice is guided by the practical facts that a) the profile calculation is more than an order of magnitude faster to compute and b) gives results nearly identical to the marginalization calculation. The resulting profile likelihood $\mathcal{L}^{max}(\sigma_h)$ is used exactly as described above in deriving the posterior density $\mathcal{P}(\sigma_h)$.

To obtain a 95% CL limit on the value of σ_h we integrate the posterior density to that value of σ_h below which 95% of the probability density lies. We note that this can be done for *any* experimental outcome, regardless of whether a signal excess is observed.

8.5 Expected Sensitivity

We evaluate our expected sensitivity by performing many pseudoexperiments in which we generate an outcome based on the expected number of events in each bin from a random Poisson distribution about the mean number expected. Since at this stage we are interested in the upper limit we can set, we assume a zero signal cross section. For each pseudoexperiment we calculate the 95% CL upper limit as discussed in the previous section. For each Higgs mass, then, we have a distribution of expected upper limits. The median of the distributions are taken as the “expected limits”.

Table 8.5 shows the median expected upper limit, and also the $\pm 1\sigma$ and $\pm 2\sigma$ ranges and the observed limits.

8.6 Results

The observed and expected limits as a function of m_A are shown in Figure 8.10. Figure 8.11 and 8.12 show the observed distributions with background in a signal and no signal case for the $\tau_e\tau_\mu$ channels. Figure 8.13 and 8.14 show the observed distributions with background in a signal and no signal case for the $\tau_e\tau_{had}$ channels. Finally figure 8.15 and 8.16 show the observed distributions with background in a signal and no signal case for the $\tau_\mu\tau_{had}$ channels.

mass (GeV)	-2σ	-1σ	median (pb)	$+1\sigma$	$+2\sigma$	observed (pb)
90.	8.801	12.062	17.310	23.888	33.375	20.396
100.	5.319	6.969	9.886	14.046	19.032	19.417
110.	2.643	3.537	4.830	6.940	9.022	11.224
120.	1.561	2.185	2.998	4.328	5.894	6.734
130.	1.055	1.460	1.981	2.857	3.809	3.439
140.	0.763	1.120	1.539	2.161	2.956	1.698
150.	0.606	0.829	1.137	1.600	2.161	0.884
160.	0.440	0.637	0.876	1.272	1.654	0.547
170.	0.376	0.528	0.725	1.022	1.345	0.366
180.	0.310	0.431	0.589	0.794	1.079	0.276
190.	0.255	0.349	0.481	0.667	0.898	0.219
200.	0.215	0.296	0.415	0.584	0.783	0.188
210.	0.198	0.256	0.359	0.483	0.632	0.183
220.	0.167	0.227	0.322	0.439	0.595	0.173
230.	0.151	0.192	0.278	0.386	0.515	0.130
240.	0.136	0.180	0.246	0.360	0.475	0.124
250.	0.119	0.159	0.227	0.318	0.453	0.119
260.	0.112	0.142	0.204	0.289	0.395	0.118
270.	0.097	0.134	0.183	0.264	0.371	0.110
280.	0.093	0.124	0.166	0.228	0.307	0.107
290.	0.083	0.115	0.162	0.222	0.307	0.106
300.	0.080	0.103	0.143	0.199	0.281	0.103

Table 8.5: Expected and observed 95% CL limits on the Higgs signal cross section. For the expected limits, the columns illustrate the range of the expectation around the median.

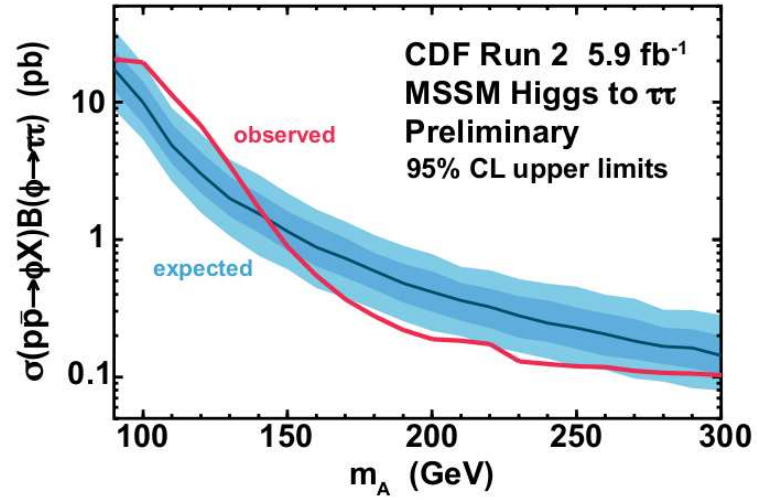


Figure 8.10: Observed and expected 95% CL upper limits on $\sigma(p\bar{p} \rightarrow \phi + X) \times BR(\phi \rightarrow \tau\tau)$ as a function of Higgs mass. The shaded areas show the $\pm 1, 2\sigma$ bands on the expected limits.

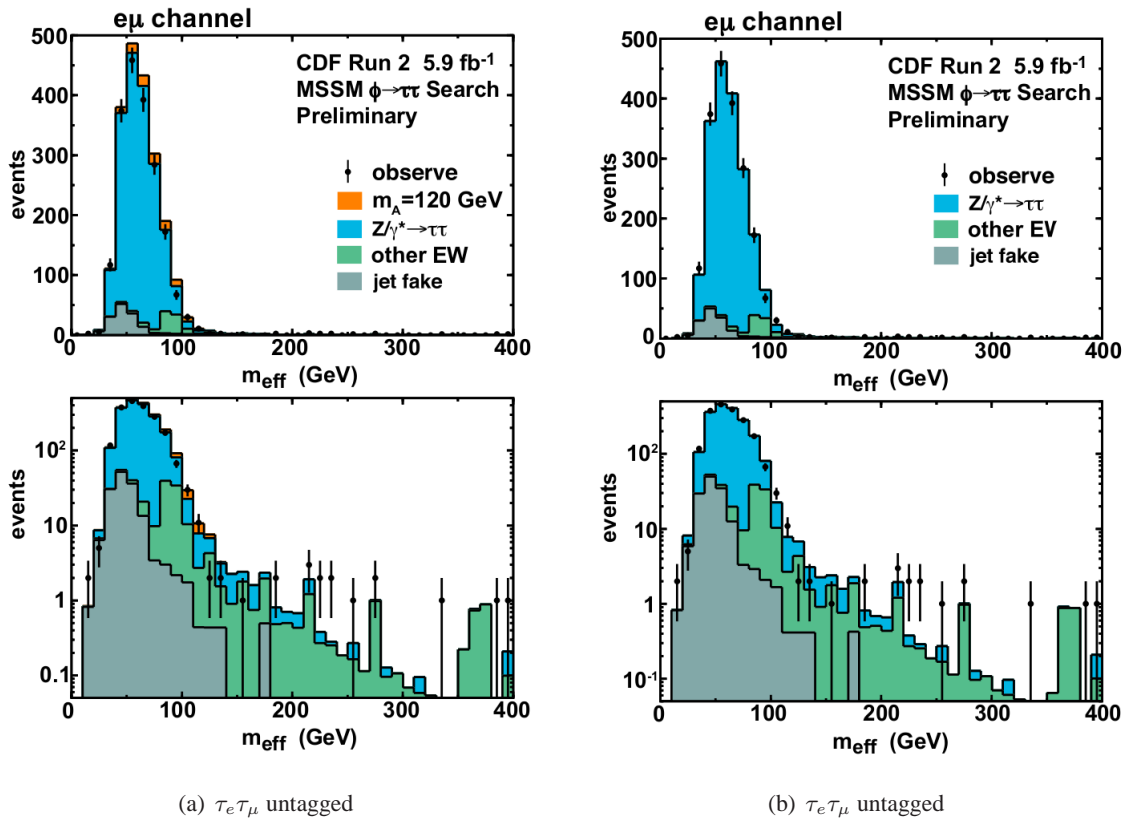


Figure 8.11: Observed distribution of m_{vis} along with and without a signal corresponding to $m_A = 120$ GeV. The signal distribution is normalized to the excluded signal at 95% CL. The backgrounds are normalized to the expectations after performing the fits.

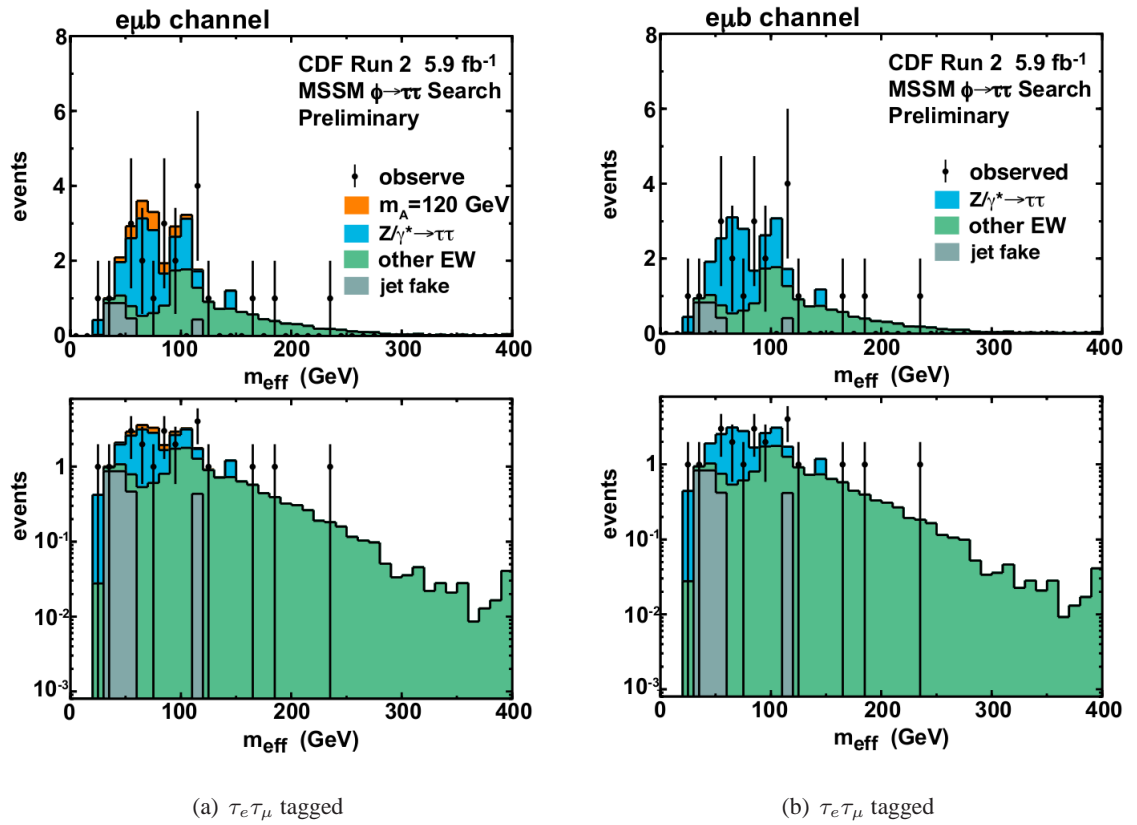


Figure 8.12: Observed distribution of m_{vis} along with and without a signal corresponding to $m_A = 120$ GeV. The signal distribution is normalized to the excluded signal at 95% CL. The backgrounds are normalized to the expectations after performing the fits.

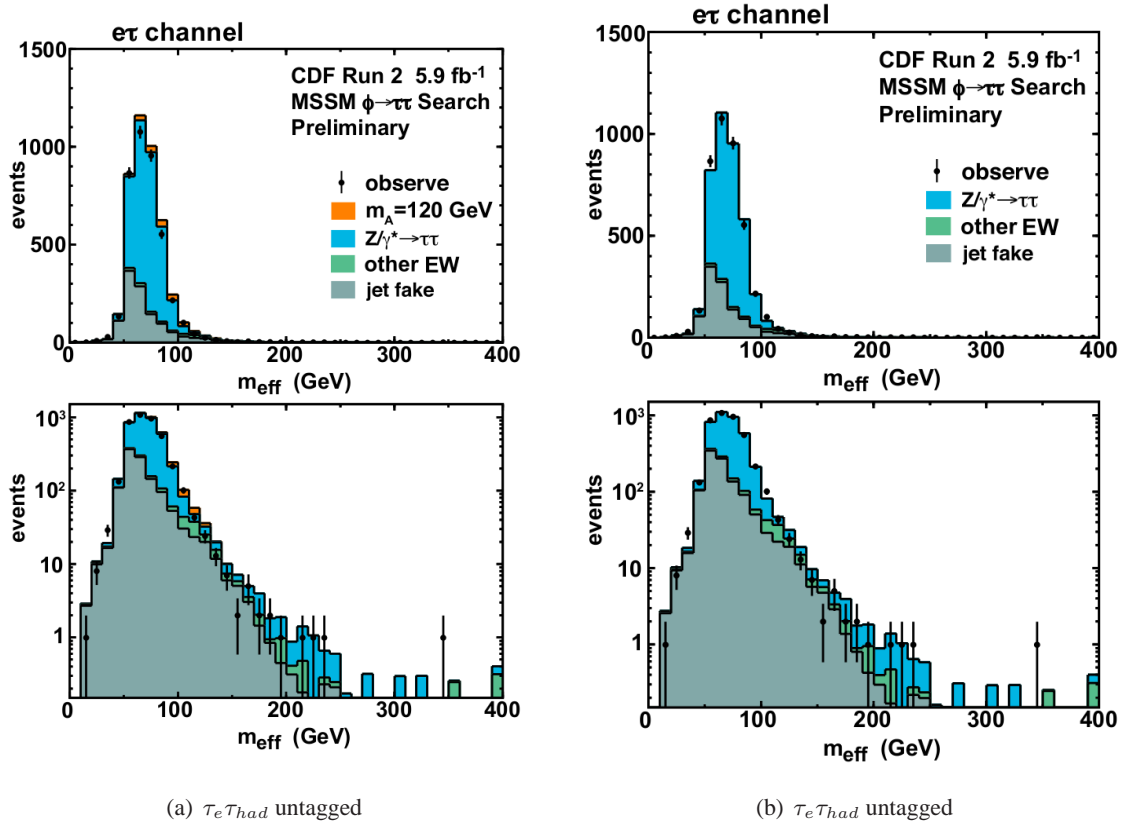


Figure 8.13: Observed distribution of m_{vis} along with and without a signal corresponding to $m_A = 120$ GeV. The signal distribution is normalized to the excluded signal at 95% CL. The backgrounds are normalized to the expectations after performing the fits.

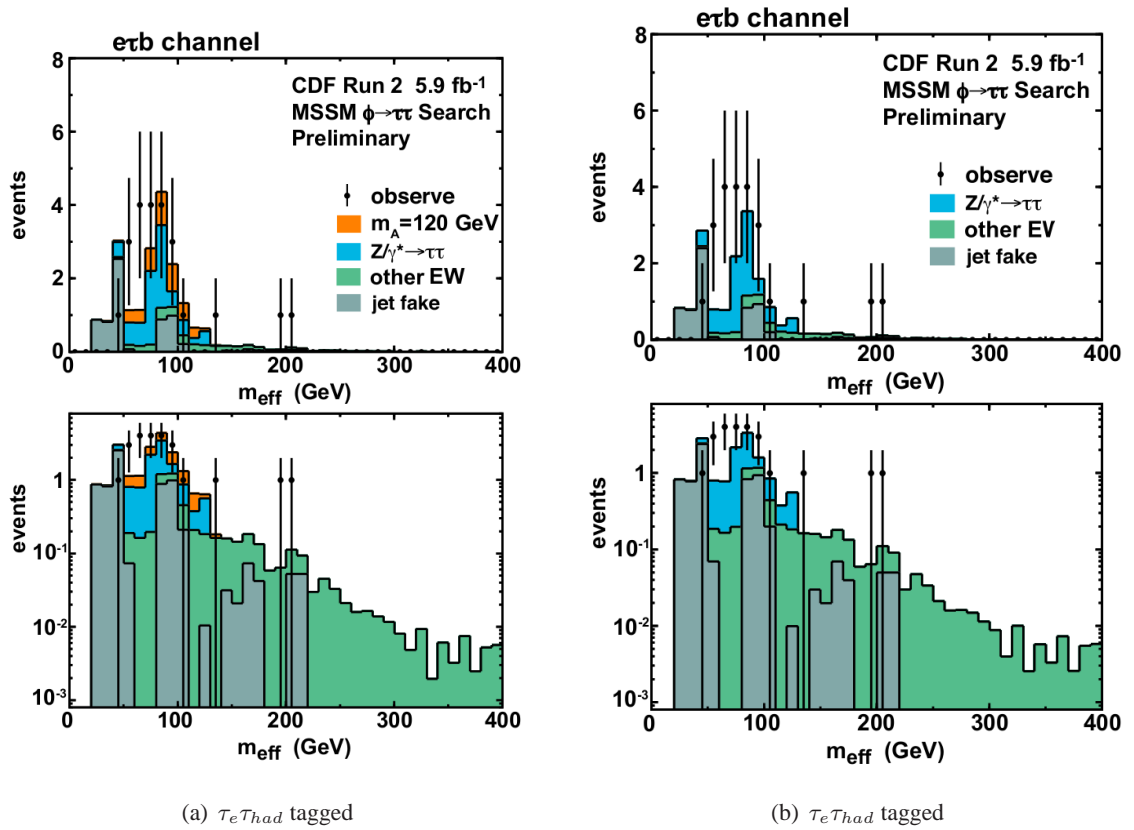


Figure 8.14: Observed distribution of m_{vis} along with and without a signal corresponding to $m_A = 120$ GeV. The signal distribution is normalized to the excluded signal at 95% CL. The backgrounds are normalized to the expectations after performing the fits.

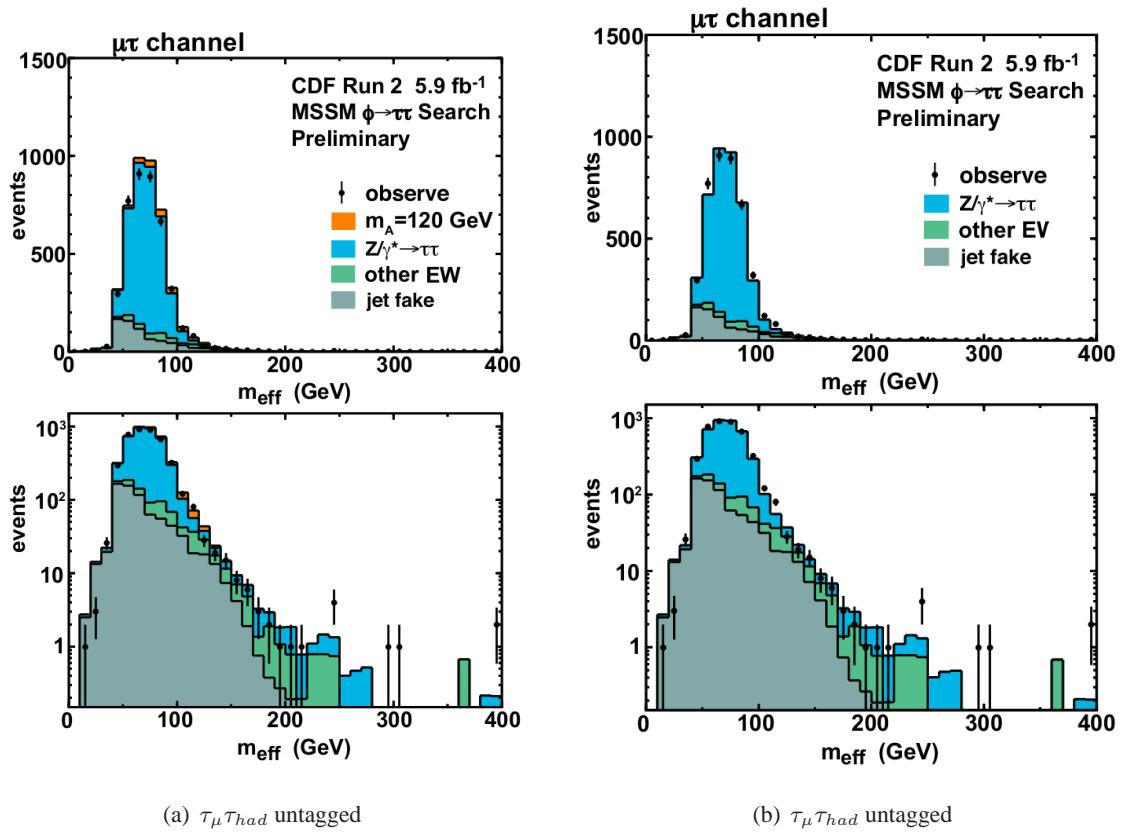


Figure 8.15: Observed distribution of m_{vis} along with and without a signal corresponding to $m_A = 120$ GeV. The signal distribution is normalized to the excluded signal at 95% CL. The backgrounds are normalized to the expectations after performing the fits.

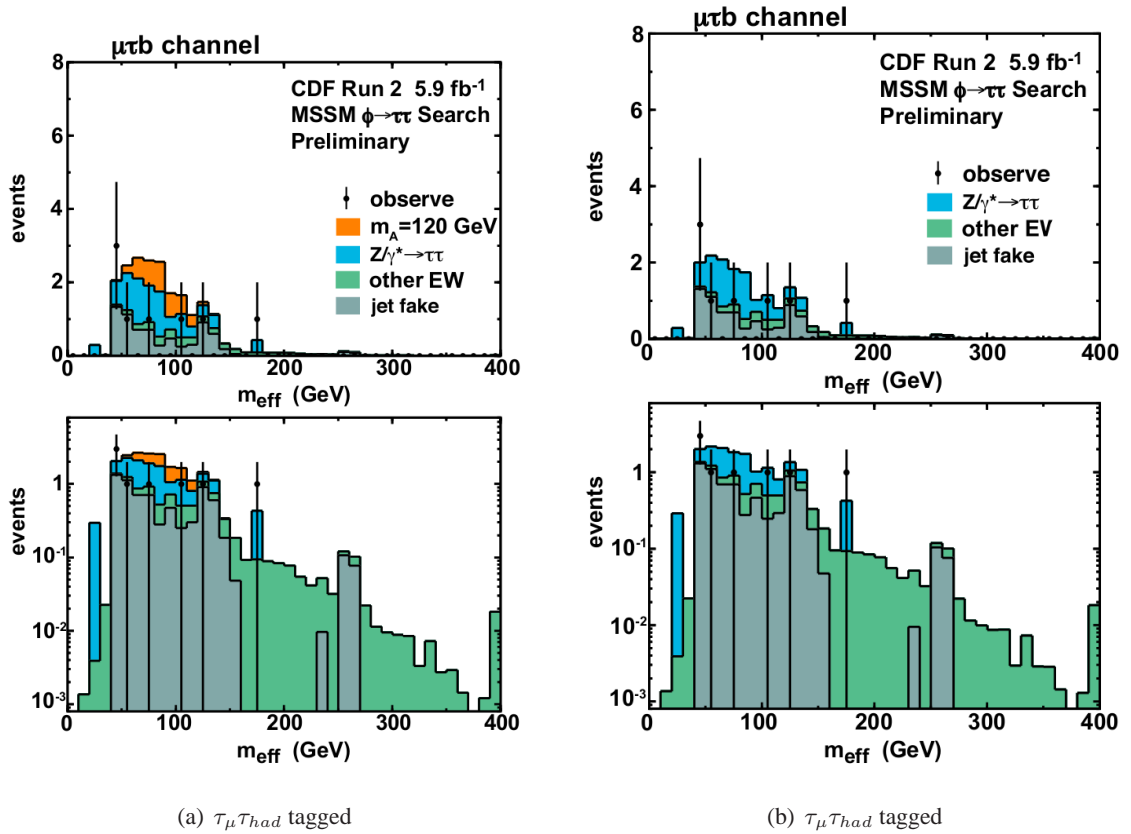


Figure 8.16: Observed distribution of m_{vis} along with and without a signal corresponding to $m_A = 120$ GeV. The signal distribution is normalized to the excluded signal at 95% CL. The backgrounds are normalized to the expectations after performing the fits.

8.7 Interpretation of the Limits

We use our observed limits at 95% CL on $\sigma(p\bar{p} \rightarrow \phi) \times \mathcal{B}(\phi \rightarrow \tau\tau)$ to exclude regions in the $\tan\beta$ vs m_A plane, where $\tan\beta$ is the ratio of the vacuum expectation values for the Higgs fields that couples to the up- and down-type fermions; m_A is the mass of the CP -odd neutral Higgs boson.

The MSSM parameter space is quite large, for the interpretation we use here the m_h^{\max} benchmark scenario. The m_h^{\max} scenario has parameters chosen such that the maximum possible Higgs mass as a function of $\tan\beta$ is obtained. The common SUSY parameters for this benchmark are Higgs mixing parameter $\mu = -0.2$ TeV, $SU(2)$ gaugino mass parameter $M_2=0.2$ TeV, $M_{SUSY}=1$ TeV, $X_t^{\overline{MS}} = \sqrt{6}M_{SUSY}$, $m_{\tilde{g}} = 0.8M_{SUSY}$. In all calculations we used top quark mass $m_t=178.0$ GeV/c² (using $m_t=174.0$ GeV/c² has negligible effect on the results).

As discussed in Section 2.2, the MSSM neutral Higgs sector has three bosons, the pseudoscalar A , and the scalar h and H . One of the scalars (either h or H) is nearly degenerate in mass and production cross-section with the A . For a given value of $\tan\beta$ in a given scenario, there is a ‘‘crossover mass’’ below which the h shadows the A and above which it is the H . In the m_h^{\max} scenario the crossover point is at $m=130$ GeV.

8.7.1 Production Cross-section Calculations

There are two production modes that are relevant for our search. Gluon fusion, $gg \rightarrow \phi$, and $b\bar{b}$ annihilation, $b\bar{b} \rightarrow \phi$, where ϕ is A, H, h .

The full MSSM production cross-sections for $b\bar{b} \rightarrow \phi$ has not been calculated. However, this process has been calculated to NLO and NNLO for the standard model Higgs (52). From the calculated cross sections for $b\bar{b} \rightarrow \phi$ in the standard model, we could naively apply a factor of $\tan^2\beta$. However, this would not take into account radiative effects. To do this properly we use the FeynHiggs program by S. Heinemeyer (7). This program takes MSSM parameters as input and outputs the couplings and branching ratios for the SM and MSSM Higgses. We take the ratio $\Gamma_{\phi \rightarrow b\bar{b}}^{\text{MSSM}}/\Gamma_{\phi \rightarrow b\bar{b}}^{\text{SM}}$ and multiply the SM production cross section of Kilgore et al. to get the $b\bar{b} \rightarrow \phi$ production cross section in the MSSM. Here $\Gamma_{\phi \rightarrow b\bar{b}}^{\text{MSSM}}, \Gamma_{\phi \rightarrow b\bar{b}}^{\text{SM}}$ are the partial widths of $\phi \rightarrow b\bar{b}$ in MSSM and SM calculated by FeynHiggs. The Δm_b correction to $\tan\beta$ changes the coupling of the Higgs to b , and therefore to τ as well. We cannot ignore the effect of Δm_b on the branching ratio, since as the coupling of the Higgs to b goes down (up), the corresponding branching fraction to $\tau\tau$ goes up (down). Therefore, we use the values of Higgs to $\tau\tau$ branching ratio output by the FeynHiggs program.

For the cross-sections for gluon fusion we use the HIGLU program by M. Spira (8). It calculates the NLO cross-sections for $gg \rightarrow A, H, h$ (using CTEQ6 PDFs). The various MSSM parameters such as $\tan\beta, \mu, M_{SUSY}$, and the tri-linear couplings are taken as input parameters.

HIGLU can calculate the cross-sections for any $\tan\beta$ but does not take into account radiative corrections modifying the Higgs couplings to b -quarks which can have a significant effect. Fortunately, these corrections behave exactly like in the case of $b\bar{b} \rightarrow \text{Higgs}$ (55). Therefore, we calculate the SM cross-section using HIGLU and apply the MSSM enhancement factors from FeynHiggs as described above for the $b\bar{b} \rightarrow \text{Higgs}$ case.

8.7.2 Excluded region in $\tan\beta$ vs m_A

Figure 8.17 shows the excluded parameter region in the $\tan\beta$ vs m_A plane. The notable inverted peak appearance is the result of the excess of events in the low mass region. It is notable that the excluded region is a subset of the CMS excluded region (56).

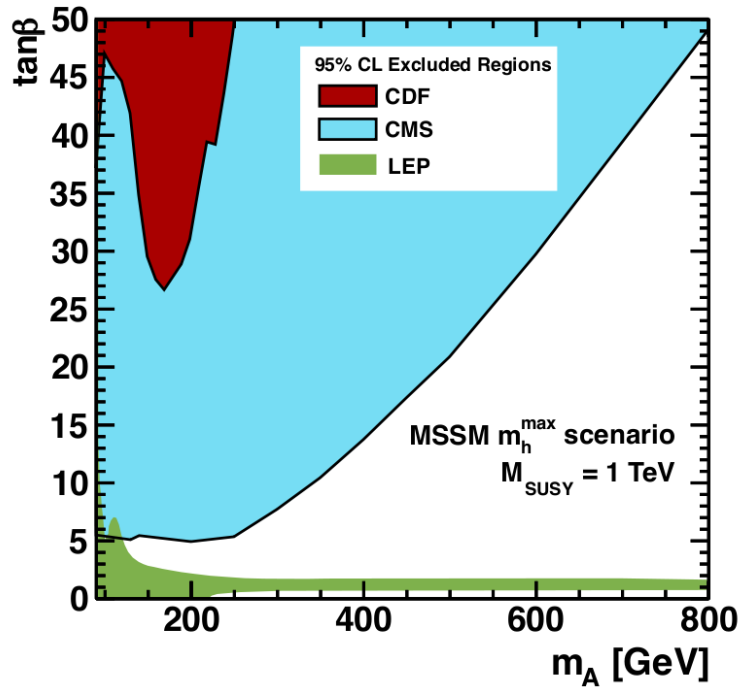


Figure 8.17: Excluded $\tan\beta$ as a function of m_A for the m_h^{\max} scenario with $\mu < 0$

8.8 Conclusions

A search for neutral MSSM Higgs bosons in the di- τ decay channel with 5.9 fb^{-1} of data in tagged and untagged channels. m_{vis} along with a template morphing technique was used to discriminate signal from background. While we observe a slight excess at low mass and a slight deficit at high mass we see no overall evidence for signal over background, and therefore set limits on the production cross section and branching ratio to taus.

This represents a result on the CDF Run II dataset, while some further improvements are possible, such as the usage of more sophisticated b-tagging methods and extension to the full CDF dataset the resulting exclusion would still be expected to fall within the larger exclusions produced by the LHC dataset which this result is consistent with.

List of Figures

2.1	The standard model particles	4
2.2	Lowest order diagram contributing to $gg \rightarrow \phi$ and $b\bar{b} \rightarrow A$	12
2.3	Rate of associated production with b-quarks of MSSM Higgs for a particular set of MSSM parameters.	13
3.1	The Tevatron accelerator complex	14
3.2	The CDF II detector	16
3.3	The CDF II detector	17
3.4	The CDF II Trigger system	23
3.5	The CDF II Level 1 and Level 2 Trigger system	26
4.1	ΔZ and ΔPt between the data muons and simulated taus at the generator level .	29
4.2	$\Delta\phi$ and $\Delta\eta$ between the data muons and simulated taus at the generator level .	30
5.1	XFT track finding efficiency for tracks that cross the $Z = 0$ plane. We parameterized this efficiency as a function of the radius at which the tracks cross that plane, $RZ0$	35
5.2	XFT track finding efficiency for tracks that cross the $Z = 0$ plane. We parameterized this efficiency as a function of the radius at which the tracks cross that plane, $RZ0$. Shown are the post-shutdown efficiency and the XFT4+SLAM efficiency.	36
5.3	XFT track finding efficiency for tracks that do not cross the $Z = 0$ plane. We parameterized this efficiency as a function of the length of the track path in the $r - z$ plane.	37
5.4	XFT track finding efficiency for tracks that don't cross the $Z = 0$ plane. We parameterized this efficiency as a function of the length of the track path in the $r - z$ plane.	38
5.5	We compared the efficiency in Jet20 data and QCD 18 MC simulation (upper left). This was used to derive a scale factor as a function of the number of towers (upper right) in the τ cluster resulting in the corrected level 2 cluster trigger efficiency (lower).	39
5.6	We compared the efficiency in Jet20 data and QCD 18 MC simulation (upper left) after the implementation of the pass 13 clustering algorithm. This was used to derive a scale factor as a function of the number of towers (upper right) in the τ cluster resulting in the corrected level 2 cluster trigger efficiency (lower). . .	40
5.7	L3 efficiency parameterized in terms of the number of primary vertexes for the old trigger.	40

5.8	L3 efficiency parameterized in terms of the number of primary vertexes for the new trigger.	41
5.9	L3 “migration” efficiency for the “old trigger”, parameterized in terms of $\Delta\theta_{min}$	42
5.10	L3 “migration” efficiency for the “new trigger”, parameterized in terms of $\Delta\alpha_{min}$	43
6.1	Invariant mass of the selected electron pairs (1 fb ⁻¹ sample).	48
6.2	Data/MC scale factor for track isolation of electrons (left), and muons (right). The scales are plotted as a function muon p_T (electron E_T).	50
6.3	Invariant mass of selected muon pairs (1 fb ⁻¹ sample).	50
6.4	Comparison of the efficiency of the $\sum p_{T,trk}^{iso} < 2 \text{ GeV}$, $\sum E_{T,\pi^0}^{iso} < 1 \text{ GeV}$ cuts in data and MC using $Z \rightarrow ee, \mu\mu$ events (1.8 fb ⁻¹ sample).	54
6.5	Comparison of the efficiency of the $\sum p_{T,trk}^{iso} < 2 \text{ GeV}$, $\sum E_{T,\pi^0}^{iso} < 1 \text{ GeV}$ cuts in data and MC using $Z \rightarrow ee, \mu\mu$ events (1.8 fb ⁻¹ sample).	55
6.6	Track multiplicity and $m(trks + \pi^0$'s) for tau candidates. Contributions from $W \rightarrow \tau\nu$ and various backgrounds are included as shown in the Legend.	56
6.7	Distributions of tau p_T in data and MC after correcting data for the observed shifts (left), and the resulting KS test (right).	57
6.8	Distributions of \cancel{E}_T in $\mu\tau$ channel with tau correction (left) and without tau correction (right)	59
7.1	Illustration of the definition of parameters used in the ζ cut.	61
7.2	Effect of the ζ cut.	61
7.3	Effect of the $ E_T^e + p_T^\mu $ cut on like-sign data events and Higgs signal ($m_A =$ 90, 200 GeV).The normalization of the Higgs signal is arbitrary.	62
7.4	Track isolation for electrons and muons in same-sign events passing all other selection criteria.	64
7.5	Signal selection efficiencies for the three detection modes as a function of Higgs mass (m_A).	69
8.1	Distributions for $\tau_e\tau_{had}$ candidate events.	72
8.2	Distributions for $\tau_e\tau_{had}$ candidate events.	73
8.3	Distributions for $\tau_\mu\tau_{had}$ candidate events.	74
8.4	Distributions for $\tau_\mu\tau_{had}$ candidate events.	75
8.5	Distributions for $\tau_e\tau_\mu$ candidate events.	76
8.6	Distributions for $\tau_e\tau_\mu$ candidate events.	77
8.7	Distributions in the three channels used for signal extraction. All background normalizations are absolute.	78
8.8	Distributions for b-tagged channels, first line is $\tau_e\tau_{had}$, second line is $\tau_\mu\tau_{had}$ and third line is $\tau_e\tau_\mu$	79

8.9	Visible mass distributions for Z and Higgs bosons (normalized to the same area).	84
8.10	Observed and expected 95% CL upper limits on $\sigma(p\bar{p} \rightarrow \phi + X) \times BR(\phi \rightarrow \tau\tau)$ as a function of Higgs mass. The shaded areas show the $\pm 1, 2\sigma$ bands on the expected limits.	88
8.11	Observed distribution of m_{vis} along with and without a signal corresponding to $m_A = 120$ GeV. The signal distribution is normalized to the excluded signal at 95% CL. The backgrounds are normalized to the expectations after performing the fits.	88
8.12	Observed distribution of m_{vis} along with and without a signal corresponding to $m_A = 120$ GeV. The signal distribution is normalized to the excluded signal at 95% CL. The backgrounds are normalized to the expectations after performing the fits.	89
8.13	Observed distribution of m_{vis} along with and without a signal corresponding to $m_A = 120$ GeV. The signal distribution is normalized to the excluded signal at 95% CL. The backgrounds are normalized to the expectations after performing the fits.	90
8.14	Observed distribution of m_{vis} along with and without a signal corresponding to $m_A = 120$ GeV. The signal distribution is normalized to the excluded signal at 95% CL. The backgrounds are normalized to the expectations after performing the fits.	91
8.15	Observed distribution of m_{vis} along with and without a signal corresponding to $m_A = 120$ GeV. The signal distribution is normalized to the excluded signal at 95% CL. The backgrounds are normalized to the expectations after performing the fits.	92
8.16	Observed distribution of m_{vis} along with and without a signal corresponding to $m_A = 120$ GeV. The signal distribution is normalized to the excluded signal at 95% CL. The backgrounds are normalized to the expectations after performing the fits.	93
8.17	Excluded $\tan \beta$ as a function of m_A for the m_h^{max} scenario with $\mu < 0$	95

List of Tables

2.1	Quantum number assignment of lepton families in the GWS model	6
2.2	Quantum number assignment of quark families	9
3.1	Calorimeter Summary - Central Calorimeters	19
3.2	Calorimeter Summary - Plug and Endwall Calorimeters	20
5.1	“lepton plus track” trigger paths used in this analysis	31
5.2	L2 cluster cuts.	32
5.3	Level 3 track cuts.	33
5.4	Isolation annulus definition, and cuts for shoulder tracks	33
5.5	Fitted parameters for the L2 trigger efficiency as a function of $RZ0$	34
5.6	Fitted parameters for the L2 trigger efficiency as a function of Lrz	35
5.7	Fitted parameters for the L2 trigger efficiency as a function of Lrz	38
5.8	Results of the fits to $\Delta\theta_{min}$ and $\Delta\alpha_{min}$	42
6.1	Tau decay mode combinatorics and their importance for $\phi \rightarrow \tau\tau$ searches.	45
6.2	Measured ID and isolation efficiencies for electrons	47
6.3	Measured ID and isolation efficiencies for medium and high p_T muons	50
7.1	Summary of backgrounds and modeling methods	67
8.1	Predicted backgrounds and observed events in the $\tau_e\tau_\mu$ untagged and tagged channel after applying all selection cuts. The quoted errors are statistical only.	70
8.2	Predicted backgrounds and observed events in the $\tau_e\tau_{had}$ and $\tau_\mu\tau_{had}$ untagged channels after applying all selection cuts. The quoted errors are statistical only.	70
8.3	Predicted backgrounds and observed events in the $\tau_e\tau_{had}$ and $\tau_\mu\tau_{had}$ tagged channels after applying all selection cuts. The quoted errors are statistical only.	71
8.4	Systematic uncertainties by source.	83
8.5	Expected and observed 95% CL limits on the Higgs signal cross section. For the expected limits, the columns illustrate the range of the expectation around the median.	87

Bibliography

- [1] Cons Gattuso, Andrew Braun, Denton Morris, Robin Spayde, Bruce Worthel, Brent Evanger, Pat Karns, [Operations Concepts Rookie Book](#). 14
- [2] The ALEPH, DELPHI, L3, OPAL, and the LEP W Working Group, "Combined Preliminary Results on the Mass and Width of the W Boson Measured by the LEP Experiments" LEPEWWG/MASS/2006-01 3
- [3] The ALEPH, DELPHI, L3, OPAL, SLD Collaborations, the LEP Electroweak Working Group, the SLD Electroweak and Heavy Flavour Groups, "Precision Electroweak Measurements on the Z Resonance" Phys. Rept. Volume 427, pg 257, 2006 3
- [4] John Terning. *Modern Supersymmetry: Dynamics and Duality*. Oxford University Press, 2006.
- [5] T. Morii, C.S. Lim, and S.N. Mukherjee. *The Physics of the Standard Model and Beyond*. World Scientific, 2004. 3
- [6] S.P. Martin, "A Supersymmetry Primer," *Perspectives on Supersymmetry*, Ed. Kane, G., pp.1–98 (World Scientific, Singapore, 1998), hep-ph/9709356 12
- [7] S. Heinemeyer, W. Hollik and G. Weiglein, Comput. Phys. Commun. 124, 76 (2000) [hep-ph/9812320]. S. Heinemeyer, W. Hollik and G. Weiglein, Eur. Phys. J. C 9, 343 (1999) [hep-ph/9812472]. G. Degrassi, S. Heinemeyer, W. Hollik, P. Slavich and G. Weiglein, Eur. Phys. J. C 28, 133 (2003) [hep-ph/0212020]. M. Frank, T. Hahn, S. Heinemeyer, W. Hollik, H. Rzehak and G. Weiglein, JHEP 0702, 047 (2007) [hep-ph/0611326]. 94
- [8] M. Spira, "HIGLU: A Program for the Calculation of the Total Higgs Production Cross Section at Hadron Colliders via Gluon Fusion including QCD Corrections" arXiv:hep-ph/9510347. 94
- [9] Report of the Tevatron Run 2 Higgs Working Group, hep-ph/0010338. 13
- [10] T. Affolder *et al.*. CDF Central Outer Tracker. *Nucl. Instrum. Meth.*, A526:249, 2004 18
- [11] C.S. Hill. L00: Operational Experience and Performance of the CDFII Silicon Detector. *Nucl. Instrum. Meth.*, A530: 1-6, 2004. 18
- [12] A. Sill. SVX-II: CDF Run II Silicon Tracking Projects. *Nucl. Instrum. Meth.*, A447:1-8, 2000. 18
- [13] A. Affolder *et al.*. ISL: Intermediate Silicon Layers Detector for the CDF Experiment. *Nucl. Instrum. Meth.*, A453:84-88, 2000. 18

- [14] CDF Collaboration. [A Brief Description of Run II Detector](#) 18, 19, 20, 21
- [15] L. Balka *et al.*, The CDF Central Electromagnetic Calorimeter. *Nucl. Instrum. Meth.*, A267:272, 1988. 20
- [16] S. Bertolucci *et al.*, The CDF Central and Endwall Hadron Calorimeter. *Nucl. Instrum. Meth.*, A267:301, 1988 20, 21
- [17] M. Albrow *et al.*, The CDF plug upgrade electromagnetic calorimeter: test beam results. *Nucl. Instrum. Meth.*, A487:381-395, 2002. 20, 21
- [18] R. Blair *et al.* [CDF-II Collaboration], The CDF-II detector: Technical design report, FERMILAB-DESIGN-1996-01. 20, 21
- [19] D. Acosta *et al.* [CDF-II Collaboration] The CDF Cherenkov luminosity monitor. *Nucl. Instrum. Meth.* A461:540-544, 2001. 21
- [20] D. Acosta *et al.* [CDF-II Collaboration] The Performance of the CDF Luminosity Monitor. *Nucl. Instrum. Meth.* A494:57-62, 2002 22
- [21] S. Klimenko, J. Konigsberg, Tony M. Liss. Averaging of the inelastic cross sections measured by the CDF and the E811 experiments. FERMILAB-FN-0741, Dec 2003. 22
- [22] Hauser, J. *et al.* "Plug shower maximum detector: Design proposal - Preprint" - Hauser, J. (94/10,rec.Jan.95) 43 p. Rochester U. - UR-1389 (94/10,rec.Jan.95) 240-282 21
- [23] A. Anastassov. Non-isolated π^0/γ reconstruction. CDF/6688, 2003. 21
- [24] C.Paus *et al.* "Design and Performance Tests of the CDF Time-of-Flight System," *Nucl. Instrum. Meth.* A 461:579-581, 2001. 19
- [25] A. Anastassov *et al.*, "Search for Neutral MSSM Higgs Boson(s) in the tau tau Decay Channel", CDF7027 (2004) 32
- [26] A. Anastassov *et al.*, "Search for Neutral MSSM Higgs Boson(s) in the tau tau Decay Channel", CDF7622 (2005). 32, 51, 82
- [27] A. Anastassov *et al.*, "Search for Neutral MSSM Higgs Boson(s) in the tau tau Decay Channel", CDF8639 (2006). 32, 57
- [28] A. Anastassov *et al.*, "Search for Neutral MSSM Higgs Boson(s) in the tau tau Decay Channel", CDF8972 (2007). 32
- [29] S. Baroiant *et al.* "Update on the Lepton+Track Trigger in Run II - Definition and Physics Goals", CDF6325 (2003).
- [30] A. Canepa *et al.* "Level-2 Claorimeter Trigger System - L2CAL", CDF8940 (2007). 25

- [31] H. Frisch *et al.* "Conceptual Design of the L1 Calorimeter trigger for the Run II Upgrade", CDF2909 (1996).
- [32] N. Eddy *et al.* "The XTRP System: An Overview". 24
- [33] D. Amidei *et al.* "New Shower Maximum Trigger for Electrons and Photons at CDF", CDF2740(1994). 25
- [34] B. Ashmanskas *et al.* "The CDF Silicon Vertex Trigger" arXiv:physics/0306169 [physics.ins-det] 25
- [35] C.Cox *et al.* "L2 XFT Stereo Upgrade Overview", CDF8975(2007). 25
- [36] Event builder and level 3 trigger at the CDF experiment - CDF Collaboration (Anikeev, K. et al.) Comput.Phys.Commun. 140 (2001) 110-116 FERMILAB-CONF-03-172-E 27
- [37] The Trigger and Datasets Working Group. Run ii trigger table and datasets plan. CDF/PHYS/TRIGGER/CDFR/4718, 2001. 27
- [38] Sourabh Dube *et al.*, CDF8445 (2006). 31
- [39] Michael Gold *et al.*, CDF8479 (2006). 31
- [40] S. Dube, S. Somalwar "Medium E_T electron identification efficiency and scale factors using DY", CDF8321 (2006). 45, 46
- [41] E. Lytken, A. Canepa, D. Bortoletto, "Intermediate p_T muon identification efficiencies with the 1 fb^{-1} dataset", CDF8336 (2006). 45, 46, 49
- [42] U. Grundler, *et al.*, "High- P_T muons recommended cuts and efficiencies for summer 2006" CDF8262 (2006). 45, 49
- [43] T.Spreitzer *et al.* "Electron Identification in Offline Release 6.1.2", CDF7950(2005). 47
- [44] Anton Anastassov *et al.* "Tau Reconstruction Efficiency and QCD Fake Rate for Run 2", CDF6308 (2003).
- [45] S. Baroiant *et al.* "Energy Measurement for Hadronic Taus", CDF6654 (2003) 51
- [46] Anton Anastassov, "Non-isolated π^0/γ Reconstruction", CDF6688 (2003). 51
- [47] J. Conway *et al.*, "Tau Identification", CDF3545 (1997).
- [48] S. Baroiant *et al.* " $Z^0 \rightarrow \tau\tau$ Cross-Section Measurement", CDF6552 (2004). 53
- [49] See John Conway's presentation from the February 2004 CDF Statistics Meeting, available on request.

- [50] M. Carena, S. Heinemeyer, C.E.M. Wagner, and G. Weiglein "Suggestions for Benchmark Scenarios for MSSM Higgs Boson Searches at Hadron Colliders", hep-ph/0202167 (2002).
- [51] M. Carena, S. Heinemeyer, C.E.M. Wagner, and G. Weiglein "Suggestions for Improved Benchmark Scenarios for Higgs-Boson Searches at LEP2", hep-ph/9912223 (1999).
- [52] F. Maltoni, Z. Sullivan, S. Willenbrock, "Higgs-Boson Production via Bottom-Quark Fusion", hep-ph/0301033 (2003). [94](#)
- [53] R.V. Harlander, W.B. Kilgore, "Higgs boson production via bottom quark fusion in next-to-next-to-leading order", hep-ph/0304035 (2003).
- [54] A. Anastassov, C. Cuenca, J. Conway, *et. al.* Search for Neutral MSSM Higgs Bosons in the Tau Tau Decay Channel. CDF/8972, 2007 [65](#)
- [55] M. Carena *et. al.*, Eur. Phys.J. C45, 797-814 (2006). [95](#)
- [56] The CMS Collaboration, "Higgs to tau tau (MSSM) (HCP)", *CMS twiki*, CMS-PAS-HIG-12-050, July 1st, 2013 Web. August 27th, 2013